MECHANICAL AND HIGH-FREQUENCY ELECTRICAL STUDY OF PRINTED, FLEXIBLE ANTENNA UNDER DEFORMATION

A Thesis
Presented to
The Academic Faculty

by

Yi Zhou

In Partial Fulfillment
of the Requirements for the Degree
Master of Science in the
George W. Woodruff School of Mechanical Engineering

Georgia Institute of Technology
December 2019

MECHANICAL AND HIGH-FREQUENCY ELECTRICAL STUDY OF PRINTED, FLEXIBLE ANTENNA UNDER DEFORMATION

Approved by:

Dr. Suresh K. Sitaraman, Advisor
School of Mechanical Engineering
Georgia Institute of Technology

Dr. Madhavan Swaminathan
School of Electrical Engineering
Georgia Institute of Technology

Dr. Raghuram V. Pucha
School of Mechanical Engineering
Georgia Institute of Technology

Date Approved: December 6, 2019

ACKNOWLEDGEMENTS

I would like to express my sincere gratitude to my advisor, Dr. Sitaraman for his continued guidance and support in my research as well as life in graduate school over the past two and half years. I would also like to thank Dr. Madhavan Swaminathan and Dr. Raghuram V. Pucha for their valuable time to be on my committee and their feedback to my research.

I would like to acknowledge the current and former members of Computer-Aided Simulation of Packaging Reliability (CASPaR) Lab: Isaac Bower, Rui Chen, Justin Chow, Trilochan Rambhatla, David Samet, Ben Steward, Christine Taylor, and Chong Ye. The meaningful discussions we shared on research work and life have indeed made my experience in graduate school more than enjoyable.

In addition, I would like to thank other professionals and students who are involved in my research including Dr. Jim Huang from Hewlett Packard Enterprise as well as Sridhar Sivapurapu and Nahid Aslani Amoli from Dr. Swaminathan's group.

Many thanks are due to my parents who always stood behind every critical decision I made. I would not have accomplished this milestone without their love, support, and trust.

I would like to acknowledge that this material is based, in part, on research sponsored by Air Force Research Laboratory under agreement number FA8650-15-2-5401, as conducted through the flexible hybrid electronics manufacturing innovation institute, NextFlex.

TABLE OF CONTENTS

ACKNOWLEDGEMENTS **iii**

LIST OF TABLES **vi**

LIST OF FIGURES **vii**

LIST OF SYMBOLS AND ABBREVIATIONS **xiv**

SUMMARY **xvi**

CHAPTER 1. INTRODUCTION **1**

CHAPTER 2. BACKGROUND AND LINTERATURE REVIEW **5**
2.1 History of Conformal Antenna and Flexible Printed Antenna **5**
2.2 Mechanical Testing of Flexible Printed Electronics **6**
2.3 Antenna Performance Under Strain **9**

CHAPTER 3. OBJECTIVES AND SCOPE **12**

CHAPTER 4. ANTENNA DESIGN AND FABRICATION RESULTS **14**
4.1 Fabrication Process **14**
4.2 Antenna Design in HFSS **16**
4.2.1 Layer Thickness 17
4.2.2 Material Electrical Properties 19
4.2.3 HFSS Simulation Setup and Results 21
4.3 Fabrication Results and Comparison to Simulation **23**

CHAPTER 5. MANDREL BENDING TEST AND RESULTS **27**
5.1 Mandrel Bending Test Over Different Sizes of Mandrel **27**
5.1.1 Experimental Setup and Procedure 27
5.1.2 Experimental Test Results 29
5.2 Cyclic Mandrel Bending Test over Mandrel Size of 0.625 in. Radius **36**
5.2.1 Experimental Procedure and Results of Sample P1 36
5.2.2 Experimental Procedure and Results of Sample P2 37

CHAPTER 6. MECHANICAL FINITE-ELEMENT ANALYSIS OF MANDREL BENDING TEST **41**
6.1 Geometry Modeling **41**
6.2 Material Modeling **44**
6.2.1 Characterization of Printed Silver Ink's Property 44
6.2.2 Other Materials' Properties 47
6.3 Loading and Boundary Conditions **47**

6.4 Initial Meshing Details 50
6.5 Mesh Convergence and Simulation Results 51

CHAPTER 7. BIAXIAL BENDING TEST AND RESULTS 56
7.1 Experimental Fixture Design and Setup 56
7.2 Experimental High-Frequency Measurement Results 60
7.3 SEM Images Results 62

CHAPTER 8. MECHANICAL FINITE-ELEMENT ANALYSIS OF THE BIAXIAL BENDING TEST 65
8.1 Loading and Boundary Conditions 66
8.2 Mesh Convergence and Simulation Results 67

CHAPTER 9. Conductivity Change Impact on Patch Antenna's High-Frequency Electrical Behavior 78
9.1 Updated HFSS Model 78
9.2 Conductivity Impact on the S_{11} Response 80

CHAPTER 10. Conclusion, Contributions, and Future Work 82
10.1 Conclusion 82
10.2 Contributions 84
10.3 Future Work 84

REFERENCES 86

LIST OF TABLES

Table 1 - Material dielectric properties for HFSS model. 20

Table 2 - Nanoindentation results. 46

Table 3 - Mechanical material properties for Workbench model. 47

Table 4 - Mesh convergence results of the mandrel bending model. 54

Table 5 - Theoretical strain values of the printed ink sturcture under the biaxial bending condition. 68

Table 6 - Mesh convergence results of the saddle-like shape bending model. 77

LIST OF FIGURES

Figure 1 - The middle image shows an example of FHE. Some current and future applications for FHE are: (a) flexible display and touch screen, (b) e-skin for robotics, (c) medical application, (d) wearable device, (e) detection system, and (f) communication system [1]. 1

Figure 2 - Schematics of different printing methods: (a) inkjet printing, (b) screen printing, (c) aerosol jet printing, (d) flexography printing, and (e) gravure printing [8]. 2

Figure 3 - Today's wireless communication spectrum [51]. 6

Figure 4 - FHE would experience different types of deformation when in application of (a) the vehicle sensor, (b) the foldable display, and (c) the wearable electronics [54]. 7

Figure 5 - Multiple mechanical tests are developed to study the performance and reliability of FHE including: (a) stretching test, (b) adaptive curvature bending test, and (c) twisting test [57]. 8

Figure 6 - Example of the antenna mandrel bending test setup [30]. 8

Figure 7 - Cracks are observed in screen printed silver flake film on PI when under deformation [56]. 10

Figure 8 - Cracks are observed in inkjet-printed silver nanoparticle ink film on PEN when under strain [59]. 11

Figure 9 - A typical patch antenna design and the critical parameters associated with it. 14

Figure 10 - The Epson™ C88+ inkjet printer loaded with a silver nanoparticle ink (JS-B25P) from Novacentrix™ is used for the fabrication of the proposed antenna design. 15

Figure 11 - Side view of the designed multi-layered antenna. 16

Figure 12 - Top view of the multi-layered antenna. 17

Figure 13 - The 1 cm × 1 cm printed square for cross section inspection: a) the top view of the printed square on transparent PET substrate with orange copper foil underneath; b) the printed square is then cross sectioned along the AA'. 18

Figure 14 - The layer thickness measurement results from the cross section optical inspection. 18

Figure 15 - The 3D profilometer scanned result of printed ink layer thickness. 19

Figure 16 - PET's dielectric properties vary in the high-frequency region [60]. 20

Figure 17 - HFSS simulation results of different patch size. 22

Figure 18 - Final design of the patch antenna. 23

Figure 19 - The three fabricated antenna samples P1, P2 and P3. 24

Figure 20 - The configuration of the fabricated antenna measured in free space by the Agilent™ N9923A RF Vector Network Analyzer. 25

Figure 21 - Electrical high-frequency measurement results of the three fabricated antennas and their comparison to the simulation result. 26

Figure 22 - Top view of the optical inspection of the right edge of the patch. 26

Figure 23 - The antenna is seated on a sheet of polycarbonate for the flat measurements in the uniaxial bending test. 27

Figure 24 - Polycarbonate mandrel of different radii. 28

Figure 25 - The antenna is wrapped around the polycarbonate mandrel for the bent measurements in the uniaxial bending test. 29

Figure 26 - Cycle 1 S_{11} measurement results of the P1 sample tested in the bending test over different sizes of mandrel. 30

Figure 27 - Cycle 2 S_{11} measurement results of the P1 sample tested in the bending test over different sizes of mandrel. 31

Figure 28 - Cycle 3 S_{11} measurement results of the P1 sample tested in the bending test over different sizes of mandrel. 32

Figure 29 - Cycle 4 S_{11} measurement results of the P1 sample tested in the bending test over different sizes of mandrel. 33

Figure 30 - Cycle 5 S_{11} measurement results of the P1 sample tested in the bending test over different sizes of mandrel. 34

Figure 31 - All the S_{11} flat measurement results of the P1 sample tested in the bending test over different sizes of mandrel. 35

Figure 32 - S_{11} flat measurements of the P1 sample tested in the cyclic bending test over the mandrel of 0.625 in. radius. 37

Figure 33 - S_{11} flat measurements of the P2 sample tested in the cyclic bending test over the mandrel of 0.625 in. radius. 38

Figure 34 - SEM image of the antenna sample P2 subjected to 2000 cycles of mandrel bending, taken at the patch where there is no copper ground plane. 39

Figure 35 - SEM image of the antenna sample P2 subjected to 2000 cycles of mandrel bending, taken at the patch where there is underneath copper ground plane. 40

Figure 36 - SEM image of the antenna sample P2 subjected to 2000 cycles of mandrel bending, taken at the feedline location. 40

Figure 37 - Isometric view of the multi-layered antenna model. 42

Figure 38 - Top and bottom views of the multi-layered antenna model. 42

Figure 39 - Side view of the multi-layered antenna. 43

Figure 40 - Isometric view of the mandrel model. 43

Figure 41 - Nanoindentation data of the 12 indentations on the sample. 45

Figure 42 - Nanoindentation results without the two outliers. 45

Figure 43 - Initial position and loading conditions of the mandrel bending FEA model. 48

Figure 44 - Isometric views of the final position of the model. 49

Figure 45 - Initial mesh details of the mandrel bending FEA model. 50

Figure 46 - Side views of the mesh details of the model. 51

Figure 47 - Simulation result of the first principal strain distribution of the ink layer in the mandrel bending model with the initial mesh (mesh case 1). 52

Figure 48 - Simulation result of the first principal strain distribution of the ink layer in the mandrel bending model with the mesh case 2. 53

Figure 49 - Simulation result of the first principal strain distribution of the ink layer in the mandrel bending model with the mesh case 3. 54

Figure 50 - 3D CAD model of the designed saddle-like shape biaxial bending fixtures. 56

Figure 51 - The two parts of saddle-like fixture are 3D printed separately as seen in a), and they can be clamped together during the test as seen in b). 57

Figure 52 - The antenna is seated between two PLA printed blocks for the flat measurement. 58

Figure 53 - The antenna is seated in between the PLA printed fixture with the ink layer facing down when taking the bent measurement. 58

Figure 54 - The saddle-like bending fixtures are attached to universal testing machine for the cyclic bending test. 59

Figure 55 - The first cycle S_{11} response measurements of antenna sample P3 in the biaxial saddle-like bending test. 60

Figure 56 - S_{11} response flat measurements of antenna sample P3 in the cyclic biaxial saddle-like bending test. 61

Figure 57 - SEM image of the antenna sample P3 after subjected to 2000 cycles of biaxial saddle-like shape bending test. The inspection location is near the right edge of the ground plane. 63

Figure 58 - SEM image of the antenna sample P3 after subjected to 2000 cycles of biaxial saddle-like shape bending test. The inspection location is near the left edge of the ground plane. 64

Figure 59 - Isometric view of the antenna-fixture system for biaxial bending model. 65

Figure 60 - Front view of the initial position of the biaxial bending model, with the indication of boundary and loading conditions. 66

Figure 61 - Front view of the final position of the biaxial bending model. 66

Figure 62 - Isometric view of the antenna sample at the final position. 67

Figure 63 - Isometric view of the a) top fixture, and b) bottom fixture with indication of initial mesh details. 69

Figure 64 - Top view of the multi-layered patch antenna with the initial mesh details. 70

Figure 65 - Simulation result of the principal strain vector contour with the initial mesh. 71

Figure 66 - Simulation result of the first principal strain distribution of the ink layer in the saddle-like shape bending model with the initial mesh (case 1). 72

Figure 67 - Simulation result of the second principal strain distribution of the ink layer in the saddle-like shape bending model with the initial mesh (case 1). 73

Figure 68 - Simulation result of the first principal strain distribution of the ink layer in the saddle-like shape bending model with the mesh case 2. 75

Figure 69 - Simulation result of the second principal strain distribution of the ink layer in the saddle-like shape bending model with the mesh case 2. 76

Figure 70 - Updated HFSS model built based on the geometry of sample P1. 79

Figure 71 - Comparison of the HFSS simulation and measurement results of P1 at flat configuration. 79

Figure 72 - Conductivity value has impact on the S_{11} response. a) HFSS simulation results of models with different conductivity values. b) The initial and final flat measurements of P1 in mandrel bending test. 81

LIST OF SYMBOLS AND ABBREVIATIONS

CAD	Computer-Aided Design
A	Cross-Sectional Area of Conductor
A_0	Initial Cross-Sectional Area of Conductor
CLSM	Confocal Laser Scanning Microscopy
d	Distance from The Neutral Axis
ε	Strain Value
ε_r	Dielectric Constant
ε_{xx}	Normal Strain Value in X Direction
ε_{yy}	Normal Strain Value in Y Direction
FEA	Finite-Element Analysis
FHE	Flexible Hybrid Electronics
HFSS	High-Frequency Structure Simulator
IoT	Internet of Things
L	Length of Conductor
L_0	Initial Length of Conductor
P1	Fabricated Patch Antenna Sample 1
P2	Fabricated Patch Antenna Sample 2
P3	Fabricated Patch Antenna Sample 3
PEN	Polyethylene Naphthalate
PET	Polyethylene Terephthalate
PI	Polyimide
PLA	Polylactic Acid

R	Resistance of Conductor
R_0	Initial Resistance of Conductor
RF	Radio Frequency
ρ	Resistivity of Conductor
ρ	Bending Radius at Neutral Axis
ρ_0	Initial Resistivity of Conductor
ρ_x	Bending Radias In X Direction at Neutral Axis
ρ_y	Bending Radius In Y Direction at Neutral Axis
S_{11}	S-Parameter of Return Loss
SEM	Scanning Electronic Microscopy
SMA	SubMiniature Version A
SOLT	Short-Open-Load-Thru
t	Thickness of Conductor
TPU	Thermoplastic Polyurethane
VNA	Vector Network Analyzer
w	Width of Conductor
WLAN	Wireless Local Area Network

SUMMARY

Flexible hybrid electronics (FHE) has a wide range of applications including medical devices, wearable devices, communication devices, automotive and aerospace sensors, and various consumer Internet of Things (IoT). This thesis has a focus on inkjet-printed antenna. Inkjet printing is a maskless, material-saving and fully additive technique which allows a variety of conductive inks to be deposited on a wide range of flexible substrates. During usage, the FHE components are often stretched, bent, folded, and/or twisted to conform to underlying structure. Therefore, the electrical and mechanical characteristics of flexible printed electronic components should be studied under such deformation during operation.

In this work, tests have been developed for characterizing the mechanical and high-frequency electrical behavior of inkjet-printed patch antennas under uniaxial and biaxial bending. The antenna samples have been fabricated by inkjet printing silver nanoparticle ink on flexible polyethylene terephthalate (PET) substrates. Polycarbonate cylindrical mandrels of different radii have been used as test fixtures for the uniaxial bending test. Special sculptured surfaces have been 3D printed in polylactic acid (PLA) to perform the biaxial bending test. During bending tests, the S_{11} (return loss) response has been measured by a vector network analyzer (VNA) in both bent and flat configurations. Mechanical simulations have been performed to study the strain distribution in the printed elements which will lead to changes in electrical behavior. High-frequency electrical simulations have also been performed to correlate with the bending experimental data. It is seen that, the conductivity of the printed structure changes differently in different zones, due to the

various values of strain it undergoes. Although the cracks are observed in the printed structures, the maximum shift in the measured resonant frequency is less than 80 MHz in both tests.

CHAPTER 1. INTRODUCTION

Flexible hybrid electronics (FHE) as indicated by its name, has the great advantage of its ability to conform to complex geometry. Benefiting from this feature, FHE has a wide range of applications including medical devices, wearable technology, communication devices, automotive and aerospace sensors, and various consumer Internet of Things (IoT) [1]. Figure 1 indicates some of the current and future applications of FHE.

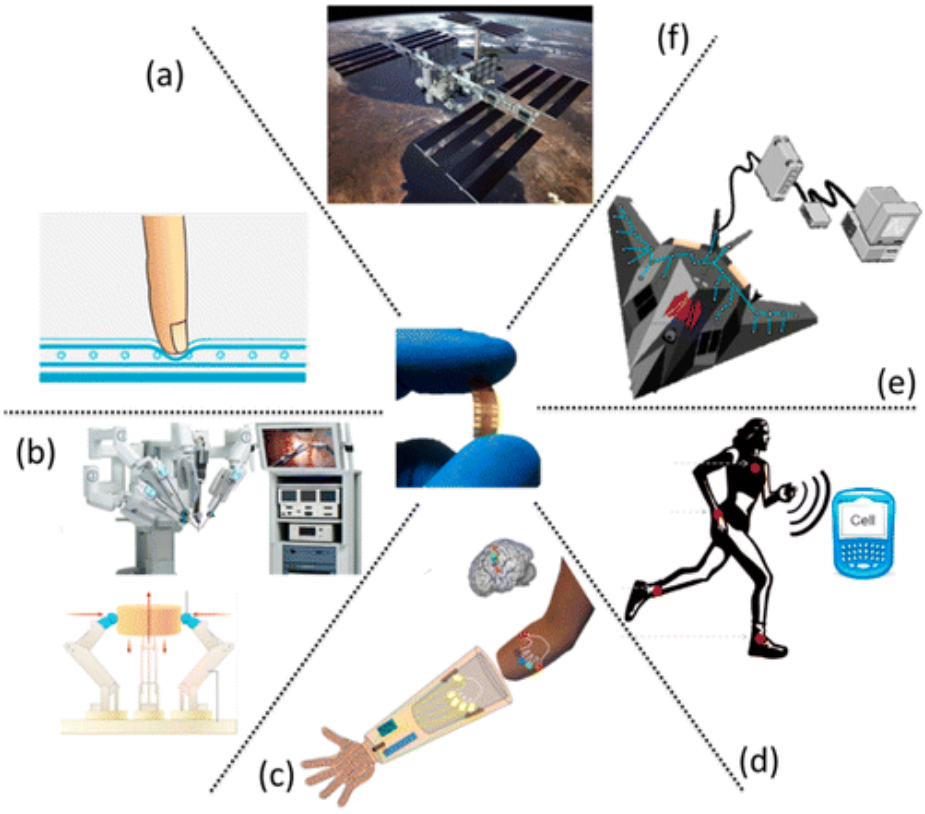

Figure 1 - The middle image shows an example of FHE. Some current and future applications for FHE are: (a) flexible display and touch screen, (b) e-skin for robotics, (c) medical application, (d) wearable device, (e) detection system, and (f) communication system [1].

Recently, printing technologies have been explored as the cost-effective fabrication methods for FHE. In general, the printing methods are additive-only, do not require clean

room environment, and can be fabricated on-demand. Some popular methods are inkjet printing, screen printing, aerosol jet printing, flexographic printing, and gravure printing, and the mechanisms of them are shown in Figure 2 [8]. Each printing method has its unique advantages and limitations. Inkjet printing is material-saving and cost-effective, but has relatively slow printing speed, low throughput, and low resolution. Screen printing is simple to perform and has high speed, but its print quality and resolution are highly impacted by the selection of the substrate, ink, and screen. Aerosol jet printing can produce finer features but has lower scalability toward large area processing. Gravure and flexographic printing have better control of feature size and are good for roll-to-roll large production but require large capital investment.

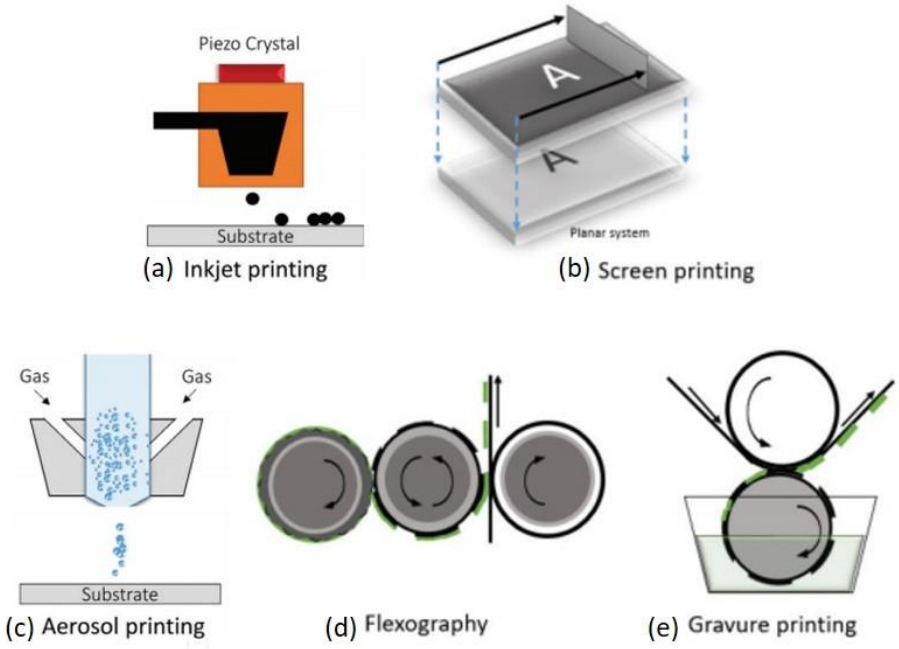

Figure 2 - Schematics of different printing methods: (a) inkjet printing, (b) screen printing, (c) aerosol jet printing, (d) flexography printing, and (e) gravure printing [8].

In printed electronics, polymer thin films are commonly used as the substrate, because they are highly flexible, can be inexpensive and permit roll-to-roll processing [9]. Some candidate polymer substrates for printing technologies include polyimide (PI), polyethylene terephthalate (PET), polyethylene naphthalate (PEN), and thermoplastic polyurethane (TPU). The different polymer films have distinct property sets, and it is crucial to pick the right film for specific application. Some key properties to be considered are mechanical strength, resistance to chemicals and solvents, optical clarity, thermal resistance, and commercial availability. Both PET and PEN have high stiffness, good chemical resistance, are optically clear, and have good commercial availability, but they have low process temperature tolerance. PI has greater process temperature tolerance and is also commercially available, but it is yellow in color and has lower mechanical strength [12]. TPU as a substrate is highly stretchable and is more comfortable to wear in a textile-integrated application, but it has lower temperature flexibility and is relatively expensive [13, 14].

Much research has been done on printable metal conductor including copper, silver, and gold on flexible substrates [15- 26]. Direct deposition of molten metals is beyond the thermal window of printing on flexible substrates; therefore, most of the research work on printable conductor ink has focused on the mix of organic solvent with metallic particle solute. The metallic ink solution upon deposition can be sintered into continuous conductive films. The sintering or curing condition would impact the conductivity of the metallic films [9].

There are several electronic components, such as strain sensors, inductors, capacitors, and antennas, that can be fabricated using commercially available inkjet printers

[27- 30]. This work focuses on a high-frequency antenna design fabricated by inkjet printer with silver nanoparticle ink on PET substrates. High-frequency antenna is an inherent element of any application that requires energy and/or signal transmission and communication [31, 32].

During the usage in different applications, the flexible antenna will undergo different types of deformation, such as stretching, bending, folding, and/or twisting to conform to underlying structure. In comparison to the rigid antenna, when the engineer design and characterize a flexible antenna, the impacts from potential physical deformations need to be taken into consideration. Uniaxial bending test is the most common test for the flexible antenna characterization. Most of the existing publications on uniaxial bending test of the flexible antenna only report the data in a limited number of bending radii [33- 39]. In these publications, the changes in antenna performance have been reported, but the correlation between the physical geometry change and the high-frequency electrical performance change has not been explored. Because of this, in this thesis, the fabricated antenna is subjected to bending using mandrels of seven bending radii from 0.625 to 4 in., and thus, the antenna is subjected to uniaxial bending. In addition, since in some applications the antenna will undergo non-planar deformation, this thesis also places the fabricated antenna in a biaxial bending condition. This thesis explores the correlation between the mechanical deformation and the high-frequency electrical performance change of the antenna.

CHAPTER 2. BACKGROUND AND LINTERATURE REVIEW

This chapter provides an overview on the background of flexible printed antenna in comparison to conformal antenna, some available mechanical tests for FHE, and the characterization method of antenna electrical performance.

2.1 History of Conformal Antenna and Flexible Printed Antenna

Antenna is an electrical component that can receive and/or transmit energy, and it is the most critical component in wireless communication systems [31]. According to the IEEE Standard Definition of Terms for Antennas (IEEE Std. 145-1993) [40], conformal antenna is an antenna that conforms to a surface whose shape is determined by considerations other than electromagnetic. The conformal antennas have been used in commercial applications such as the body of aircrafts, high-speed trains, and/or other vehicles since as early as 1990s. There have also been applications of conventional conformal antennas in medical devices [41- 42]. These conventional conformal antennas use direct fabrication of antenna elements on curved structures. Such a direct fabrication technique not only has fabrication difficulty, but also would result in heavy weight and low reliability of the fabricated antennas [43- 46].

Printing technologies such as inkjet printing, screen printing, aerosol jet printing, flexographic printing, and gravure printing are widely explored and used in the fabrication of flexible electronics elements including antennas. Compared to the conventional conformal antenna fabrication methods, printing technologies can produce antenna on a flexible substrate with benefits in lower cost, lighter weight, and easier fabrication process.

Flexible printed antenna can conform to complex underlying surface as the conventional conformal antenna does. In addition, the flexible printed antenna exceeds the capability of the conformal antenna, as it can undergo different types of deformation during usage, and multiple deformation cycles with a proper design [32].

Flexible antennas have been successfully realized by inkjet printing [30, 33, 43, 47], screen printing [48, 49], and aerosol jet printing [50]; the conductive material being printed varies from silver, copper to graphene, and the flexible substrate includes paper, PET, and polyimide. This thesis manages to design and fabricate a high-frequency antenna by inkjet printing method with silver nanoparticle ink and PET substrate. The fabricated antenna samples in this thesis have a resonant frequency around 5 GHz, which is commonly used in applications such as WLAN devices and satellite links [51]. The spectrum of wireless communication frequencies is shown in Figure 3.

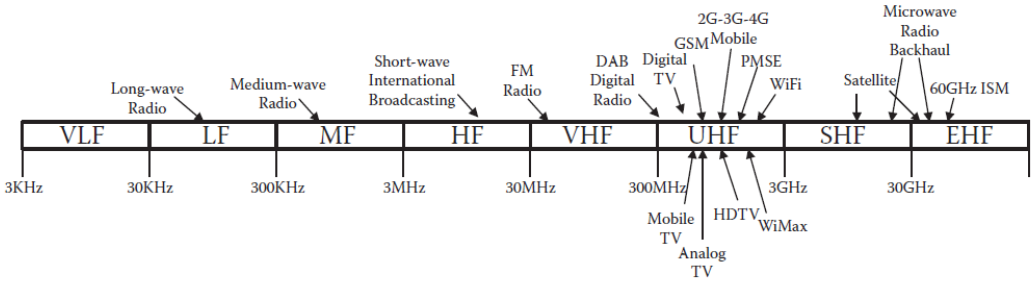

Figure 3 - Today's wireless communication spectrum [51].

2.2 Mechanical Testing of Flexible Printed Electronics

During usage, flexible printed electronics would undergo different types of deformation. Figure 4 shows several applications of flexible electronics and relevant types of deformation during usage [52- 54]. A sensor would be uniaxially or biaxially bent to

conform onto the vehicle's body, as shown in Figure 4(a). The folding deformation would be applied to the electronics in the foldable display as seen in Figure 4(b). For a wearable sensor that is embedded to clothes as shown in Figure 4(c), the sensor would be bent and/or stretched when somebody moves around while wearing it, and the sensor would potentially be twisted when being washed in the washer. Because of these, tests have been developed to study the performance and reliability of flexible printed electronics under all kinds of deformation. Figure 5 shows some typical schematics of the mechanical test setup, for stretching, bending, and twisting [55- 57].

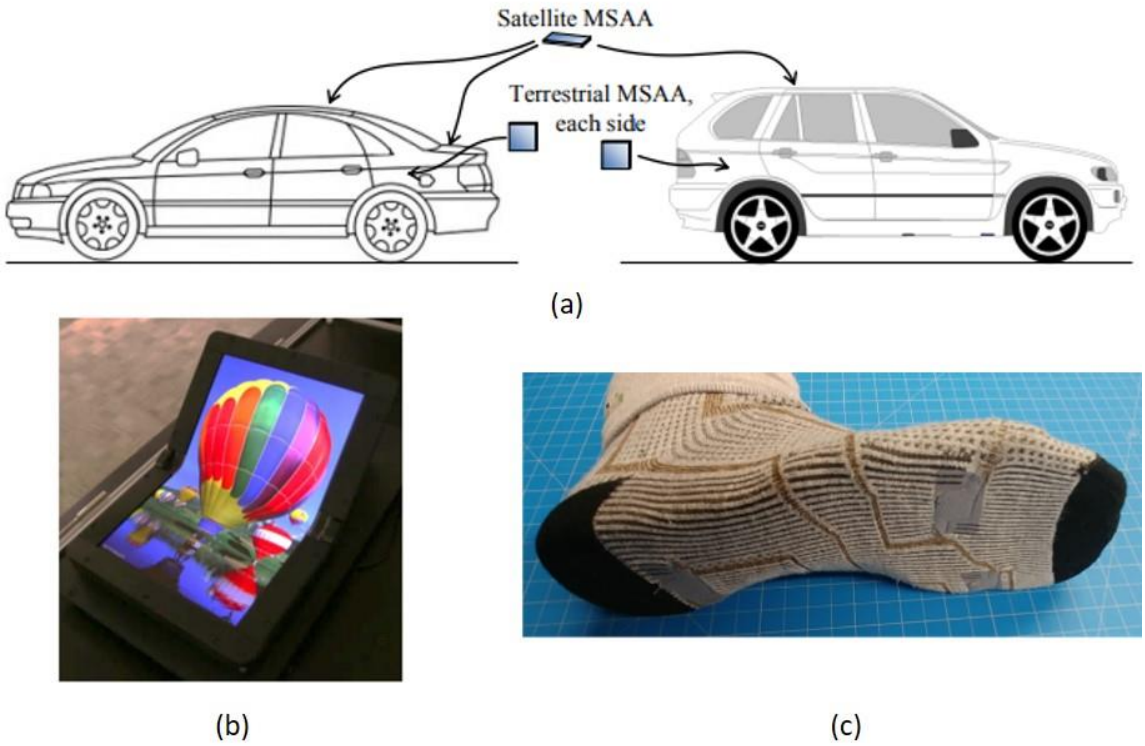

Figure 4 - FHE would experience different types of deformation when in application of (a) the vehicle sensor, (b) the foldable display, and (c) the wearable electronics [54].

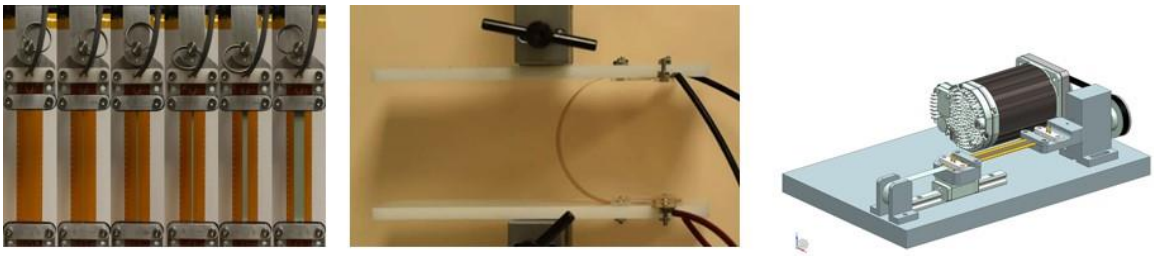

Figure 5 - Multiple mechanical tests are developed to study the performance and reliability of FHE including: (a) stretching test, (b) adaptive curvature bending test, and (c) twisting test [57].

When studying flexible printed antenna, much characterization of antenna under deformation is done in bending conditions. The most common bending test is the cylindrical mandrel bending test, which is a uniaxial constant radius bending test. In such a test, the antenna is wrapped around or attached to a cylindrical mandrel with the printed structure facing outward as show in Figure 6. In the figure, the antenna is bent in the width direction where the feedline does not experience any deformation. The antenna can also be bent along the feedline direction.

Figure 6 - Example of the antenna mandrel bending test setup [30].

Most of the previous publications on uniaxial bending test of the flexible antenna have reported the data in a limited number of bending radii [33- 39]. Furthermore, the study of the flexible antenna subjected to biaxial bending condition is very scant in the literature. In this thesis work, two sets of experimental characterization are done to the fabricated antennas. In the uniaxial mandrel bending test, the antenna samples are wrapped around seven mandrels of different sizes to examine the impact of the magnitude of strain on the antenna performance. The biaxial bending test developed by Isaac Bower [58], a former lab member, is also adapted in this thesis to test the performance of the antenna in biaxial bending circumstance.

2.3 Antenna Performance under Strain

The fundamental formula for electrical resistance of a thin metal film is

$$R = \rho \frac{L}{A} \tag{1}$$

where R is the resistance, ρ is the metal resistivity, L is the length of the sheet, and A is the cross-sectional area of the sheet. The resistance of the metal sheet would change under strain due to Poisson effect. With the assumption of no change in the volume and the resistivity of the conductive sheet, the relative resistance of the metal sheet under strain can be derived as

$$\frac{R}{R_0} = \frac{\rho}{\rho_0}\frac{LA_0}{L_0A} = \left(\frac{L}{L_0}\right)^2 \tag{2}$$

where the subscript "*0*" indicates the unstrained properties of the metal sheet. Theoretically, the change in resistance purely relies on the change of geometry.

However, the ideal case does not apply to the resistance change of the printed conductive thin film. The resistivity ρ is the inverse of conductivity σ, and the conductivity would decrease due to the mechanical damages in the printed structure. The printed conductive thin film is the cured solution of organic solvent with metallic particle solute. The silver flake type of ink is used in screen printing, and the silver nanoparticle type of ink is used in inkjet printing and aerosol jet printing. When the printed conductive structure on polymer substrate is under positive strain, the electrical resistance change and the mechanical damages are reported in the literature. The ability to handle strain differs from ink to ink. As shown in the scanning electronic microscopy (SEM) images of Figure 7, the screen-printed transmission line of silver flake on Kapton^{TM} polyimide has crack initiation upon the first cycle of adaptive curvature bending with the bending gap of 5 mm, and more noticeable cracks are observed at the 100th cycle of bending [56]. Figure 8 shows confocal laser scanning microscopy (CLSM) image of the inkjet-printed conductive film of silver nanoparticle ink on PEN substrate. At the 114th cycle of 2% strain, the cracks are visible on the ink with the measured resistance being 2.3 times of the initial resistance [59].

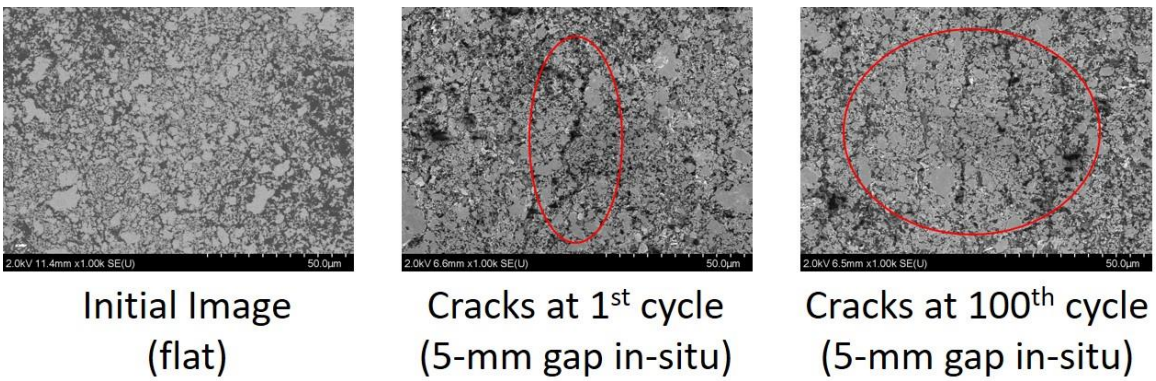

Figure 7 - Cracks are observed in screen printed silver flake film on PI when under deformation [56].

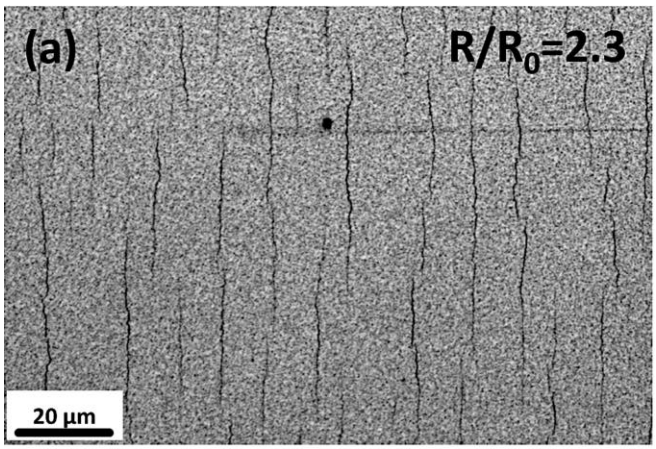

Figure 8 - Cracks are observed in inkjet-printed silver nanoparticle ink film on PEN when under strain [59].

A useful measurement describing the performance of an antenna is the reflection coefficient, also known as return loss, and it can capture the resonant frequency of the antenna. In practice of antenna design and characterization, the reflection coefficient is presented by the S-parameter (S_{11}). The antenna is resonating at the frequencies at which S_{11} is below -10 dB. Among the previous study of antenna under bending as discussed in section 2.2, S_{11} of the antenna is recorded, and some shifts of resonant frequency are noticed when at bent that compared to the flat case. In this thesis, the correlation between the high-frequency electrical performance change and the conductivity change due to uniaxial or biaxial physical deformation is explored.

CHAPTER 3. OBJECTIVES AND SCOPE

Flexible antennas can be successfully fabricated by printing methods. When in usage, the antenna will undergo bending deformation uniaxially and biaxially. Thus, it is critical to examine whether the antenna has changes in RF performance when under deformation. The objective of this thesis is to study the mechanical and high-frequency electrical performance of the inkjet-printed patch antenna under uniaxial and biaxial bending conditions, and to characterize the relationship between the mechanical deformation and the antenna's performance change. To accomplish the objective, this thesis uses the following approach:

1. Design and fabricate patch antennas by inkjet printing silver nanoparticle ink onto PET substrates with the target resonant frequency around 5 GHz.
2. Test the antenna and measure its high-frequency response under cyclic uniaxial bending condition. Utilize mandrels of different radii in the test.
3. Test the antenna and measure its high-frequency response under cyclic biaxial bending condition. Utilize specialized saddle-like shape bending fixtures.
4. Image ink structures using Scanning Electronic Microscopy (SEM) to investigate mechanical failures.
5. Perform finite-element simulations to examine strain distribution in printed ink structures in both uniaxial and biaxial bending tests.
6. Obtain mechanical properties of the ink through nanoindentation and from literature.

7. Study the impact of the deformation induced conductivity change of the ink on the high-frequency electrical performance.

CHAPTER 4. ANTENNA DESIGN AND FABRICATION RESULTS

A Patch antenna is formed by a metallic patch on a grounded substrate. A typical patch antenna design is shown in Figure 9 below. In this thesis, a rectangular patch fed by a microstrip line is designed. Inkjet printing method is used to fabricate the antenna samples. This chapter discusses the details of the antenna design, fabrication process and the fabrication results.

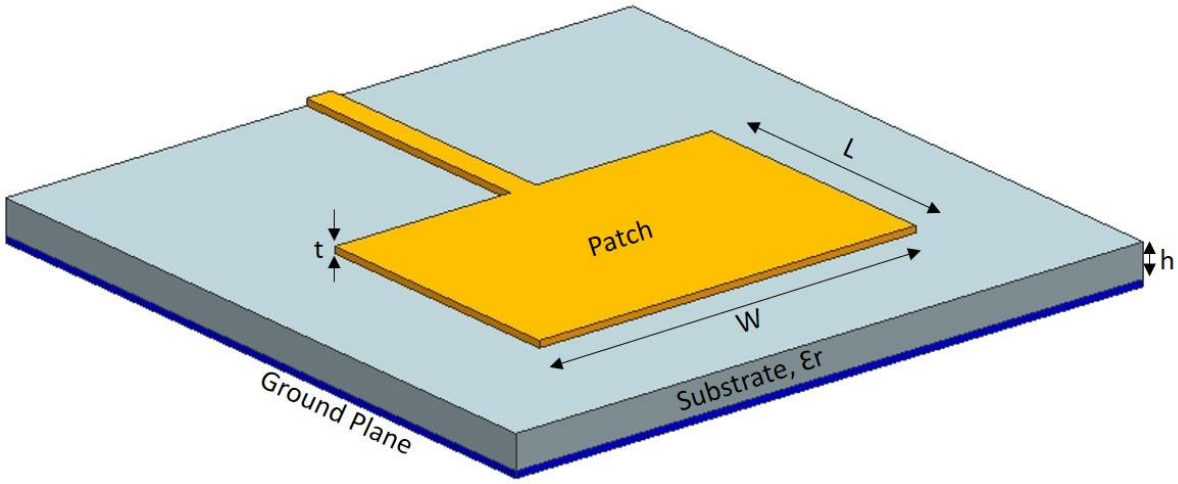

Figure 9 - A typical patch antenna design and the critical parameters associated with it.

4.1 Fabrication Process

This thesis work intends to fabricate a patch antenna utilizing the inkjet printing method. As shown in Figure 10, an Epson^{TM} C88+ inkjet printer loaded with a silver nanoparticle ink (JS-B25P) from Novacentrix^{TM} is used. To achieve the full ink coverage of the printed pattern, four passes are printed. When printing the patch antenna, the direction of printing is alternated between directions along the feedline and perpendicular

to the feedline. In between each pass, the printed structure is air-cured in ambient temperature for 30 minutes.

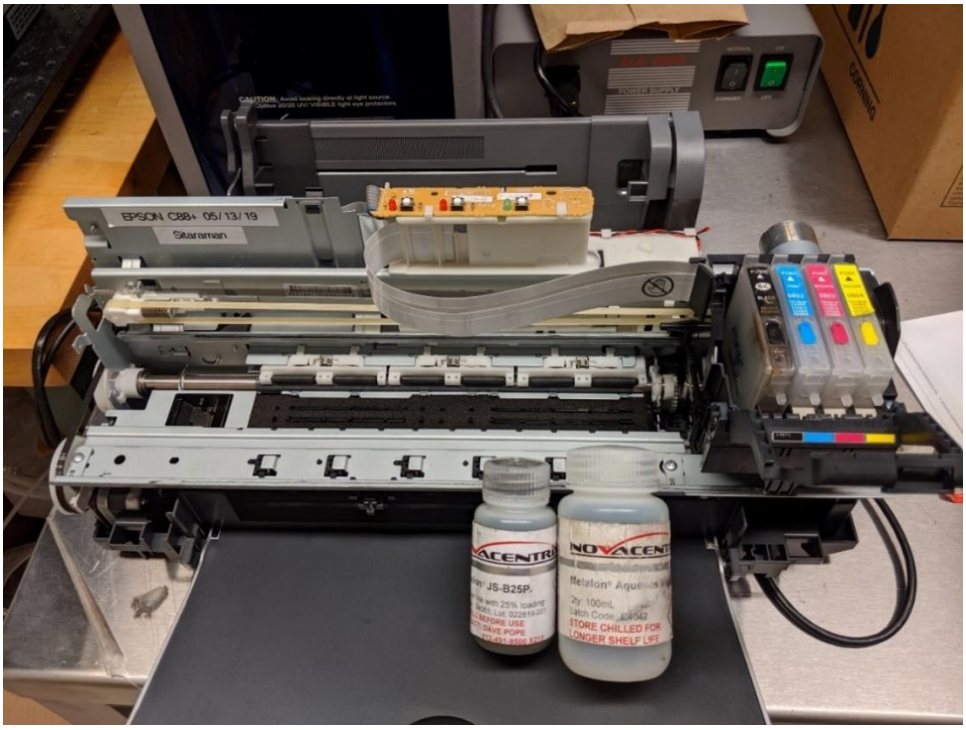

Figure 10 - The Epson™ C88+ inkjet printer loaded with a silver nanoparticle ink (JS-B25P) from Novacentrix™ is used for the fabrication of the proposed antenna design.

The conductive ink is inkjet printed on the silicone-coated front side of a polyethylene terephthalate (PET) substrate manufactured by Mitsubishi™. For the antenna sample, the other side of the substrate has a copper-foil ground plane and the copper foil is attached to the backside of the PET substrate with a 3M™ 966 adhesive tape. An indication of the multi-layered antenna is shown in Figure 11.

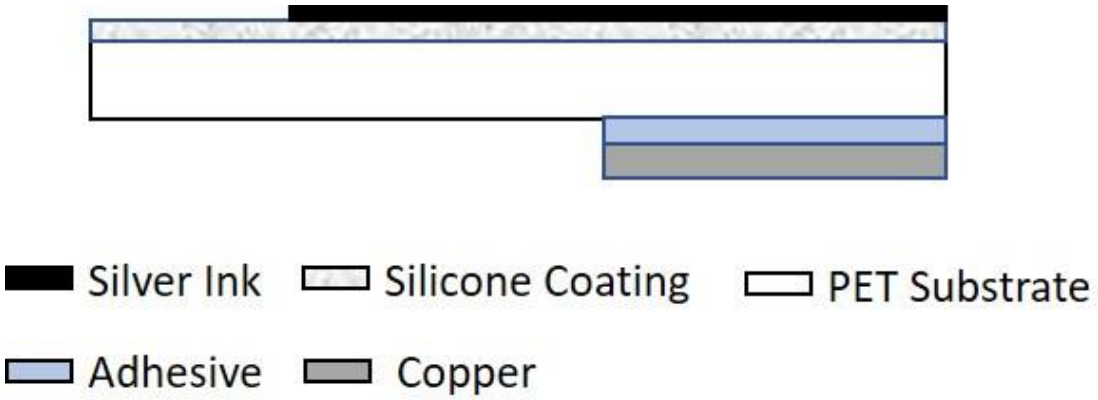

Figure 11 - Side view of the designed multi-layered antenna.

4.2 Antenna Design in HFSS

ANSYS™ HFSS (high-frequency structure simulator) is used to design the patch antenna. Figure 12 shows the top view of the antenna design, with the dimension variables that are needed in the HFSS model. The substrate width is chosen to be 50.4 mm, and the substrate length is chosen to be 76 mm; these are adapted from a previous design of a screen-printed patch antenna on Kapton™. In the antenna design, the patch is centered at the substrate. As learned from the previous design experience of the patch antenna on polymer substrate, a truncated ground plane is needed for a better match of the resonant frequency. In this design the overlap distance between the patch and the ground plane is selected to be 4 mm. The feedline width is chosen to be 0.6 mm as it is the smallest feature size of the four-pass printing. The target resonant frequency of the antenna is 5 GHz, and therefore, multiple sweeps are run to determine the patch size.

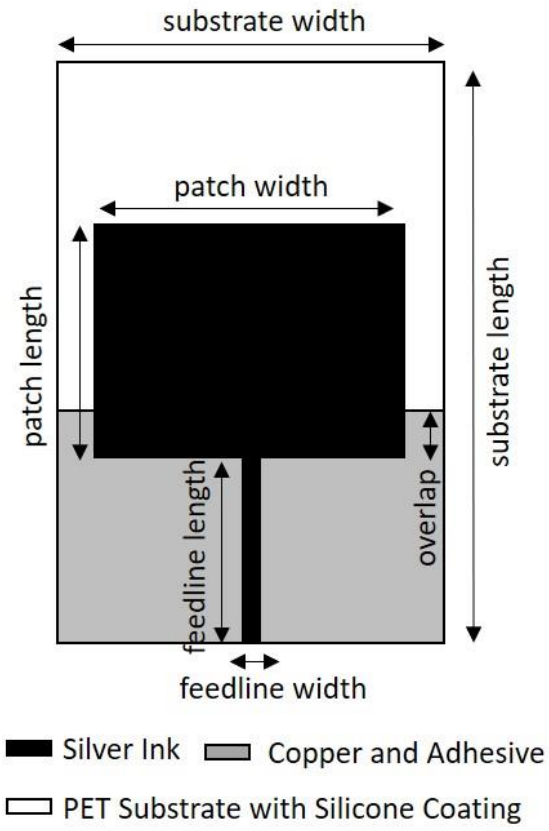

Figure 12 - Top view of the multi-layered antenna.

4.2.1 Layer Thickness

To build a valid HFSS model, the stacking details of the antenna is needed. To obtain the details of each layer, a 1 cm × 1 cm square of the ink is printed and attached to the copper foil as discussed in Section 4.1. The sample is cross sectioned and inspected by the microscope. Figure 13(a) shows the printed ink square with copper foil underneath, and Figure 13(b) shows the sample after being cross sectioned.

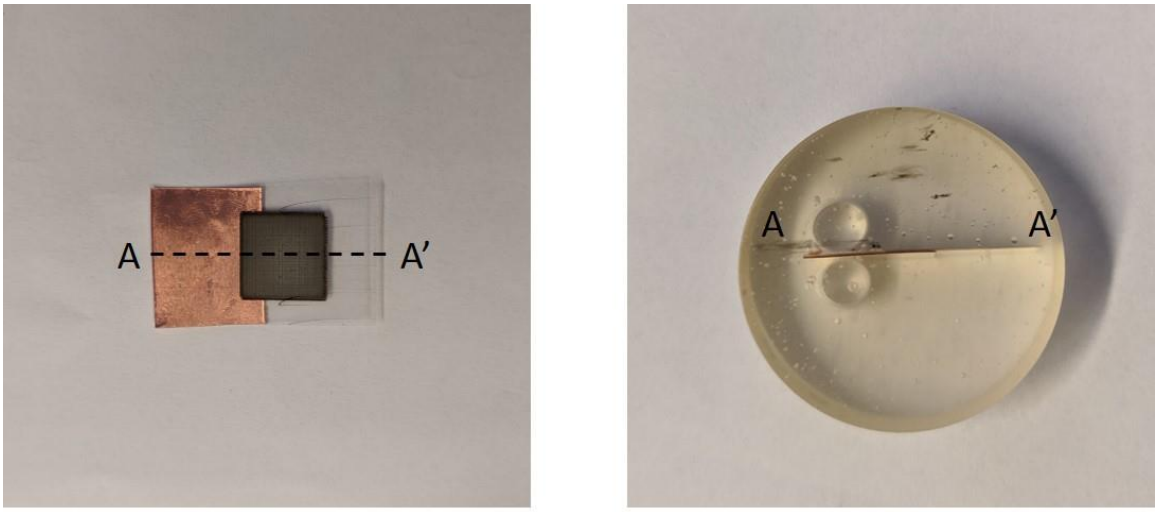

Figure 13 - The 1 cm × 1 cm printed square for cross section inspection: a) the top view of the printed square on transparent PET substrate with orange copper foil underneath; b) the printed square is then cross sectioned along the AA'.

The inspection results of the cross section are provided in Figure 14. As shown, the bottom copper layer has a thickness of 107.54 µm, the adhesive layer on top has a thickness of 59.66 µm, and the PET substrate with the silicone coating has a thickness of 134.79 µm. The silver ink is too thin to be measured correctly by microscopic image as seen.

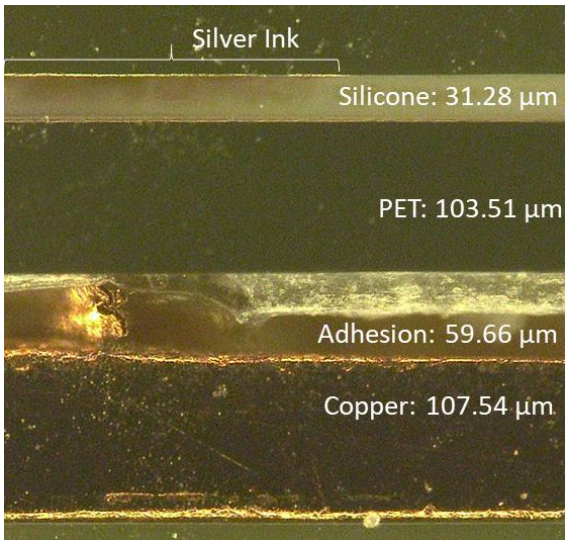

Figure 14 - The layer thickness measurement results from the cross section optical inspection.

Then the optical profilometer is used to measure the thickness of the silver ink. Figure 15 shows the 3D scanning results. In Figure 15, the darker area on the left is the PET substrate, and the brighter region on the right is the printed silver ink. As seen, the PET substrate has a relatively rough surface due to the porous silicone coating on top. Therefore, before measuring the step height, a reference surface on the PET substrate area is leveled. The ink layer thickness is measured to be 6.28 µm.

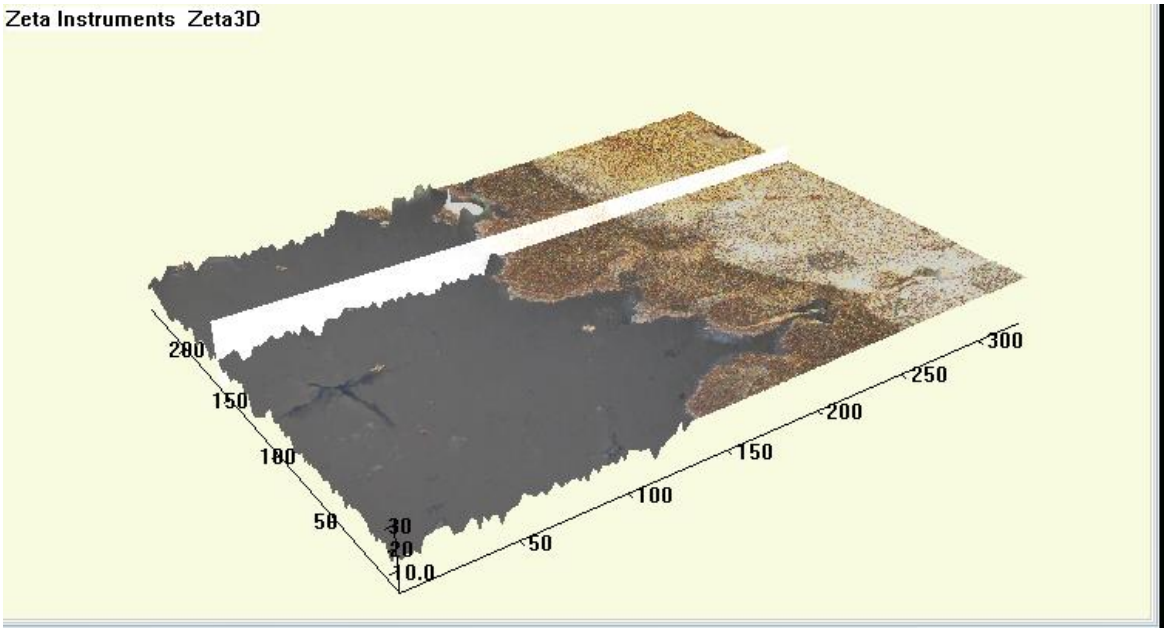

Figure 15 - The 3D profilometer scanned result of printed ink layer thickness.

4.2.2 Material Electrical Properties

The dielectric properties of the PET substrate and the adhesive are taken from the literature and are presented in Table 1. PET is reported to have different values of dielectric constant and loss tangent in the high-frequency region, as seen in Figure 16 [60]. At the target resonant frequency of 5 GHz, dielectric constant is 2.2 and loss tangent is 0.03. For the adhesive, dielectric constant is 2.92, and loss tangent is 0.025.

Table 1 - Material dielectric properties for HFSS model.

Material	Dielectric Constant	Loss Tangent
PET [60]	2.2	0.03
Adhesive [61]	2.92	0.025

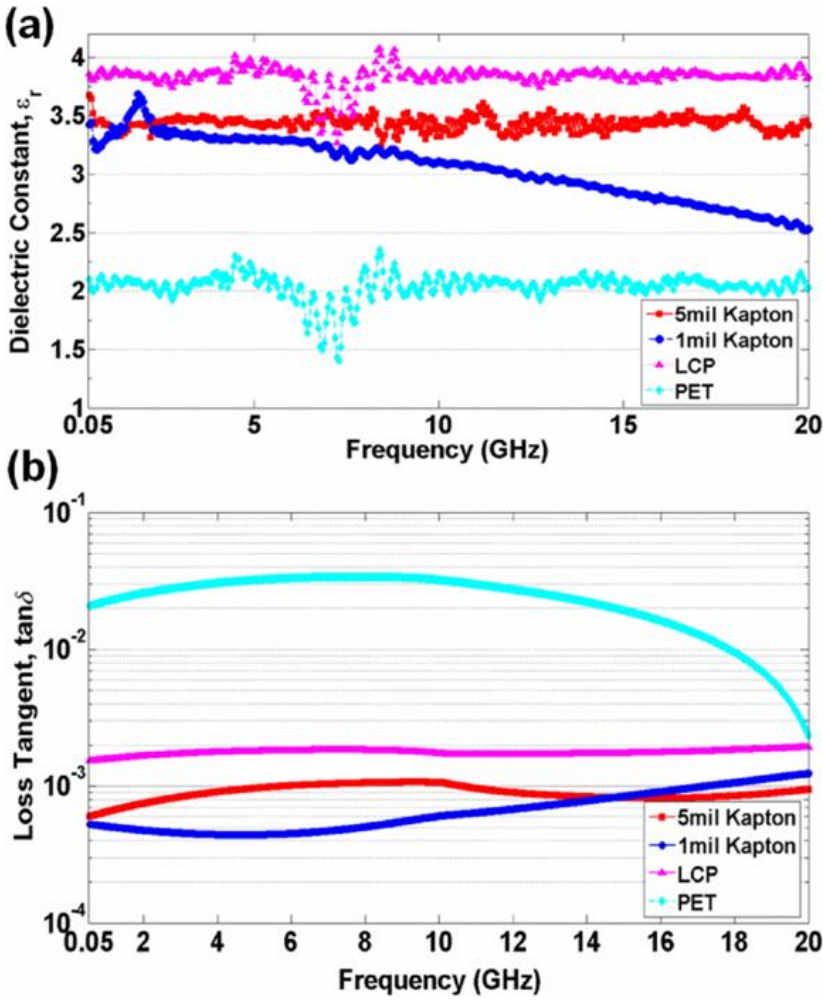

Figure 16 - PET's dielectric properties vary in the high-frequency region [60].

The copper ground plane is assumed to be the perfect conductor. But the conductivity of the silver ink is measured and calculated from a printed transmission line sample. The transmission line has a width of 0.6 mm, and a length of 21.9 mm. The four-point measurement shows that it has a resistance of 2.3 Ω. The conductivity of the printed structure can be calculated by Equations 3 and 4

$$\rho = \frac{R\,w\,t}{L} \tag{3}$$

$$\sigma = \frac{1}{\rho} \tag{4}$$

where ρ is the resistivity, R is the resistance, w is the width of the transmission line, t is the thickness of the transmission line, L is the length of the transmission line, and σ is the conductivity. The calculated conductivity input to the HFSS model is 2.52×10^6 S/m.

4.2.3 HFSS Simulation Setup and Results

Parameter sweeps for the two variables, the patch length and the patch width, are completed in ANSYS™ HFSS. Both the variables are given the range of 20 mm – 40 mm, with an increment of 10 mm; in total, nine simulations are run. Figure 17 shows the sweep results. From the results, the patch is chosen to have a length of 30 mm and a width of 40 mm. Figure 18 shows the CAD of the antenna design with the final geometry details.

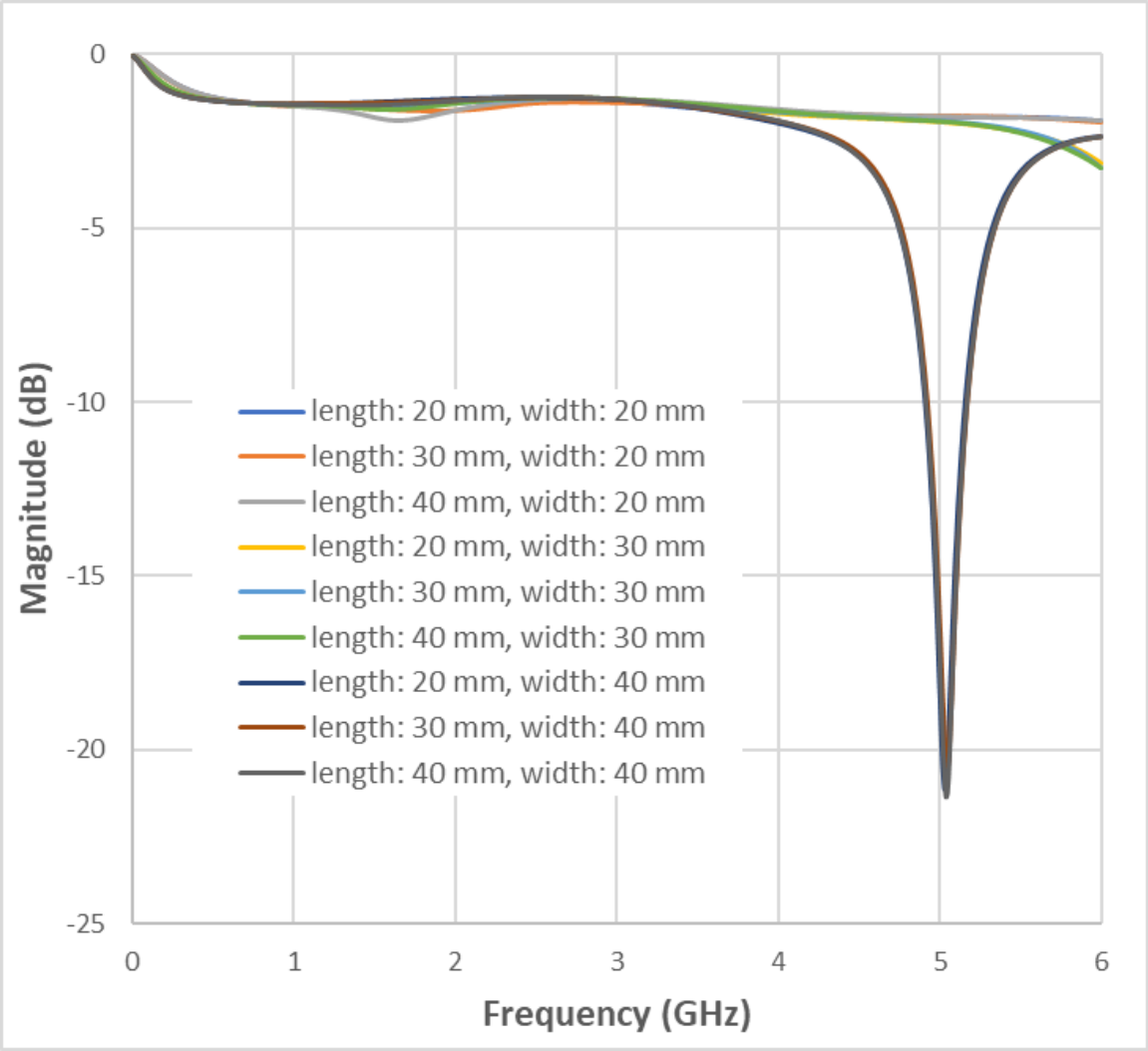

Figure 17 - HFSS simulation results of different patch size.

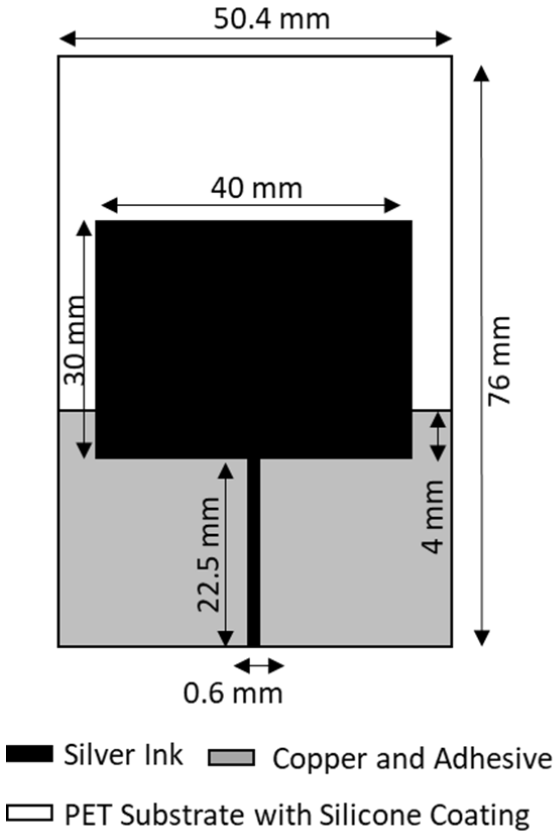

Figure 18 - Final design of the patch antenna.

4.3 Fabrication Results and Comparison to Simulation

Three antenna samples, P1, P2 and P3 are fabricated following the process discussed in Section 4.1. The three fabricated antenna is show in Figure 19. The top side of the PET substrate has the patch antenna with a feedline, while the bottom side of the substrate has the ground plane. The copper ground plane is seen through the transparent PET substrate. From the optical measurement, the patches are roughly 30 mm × 40 mm, and the feedlines have a width of 0.6 mm as designed. Edge launch ELF40-001 SMA connectors are connected by screws to excite the printed antenna.

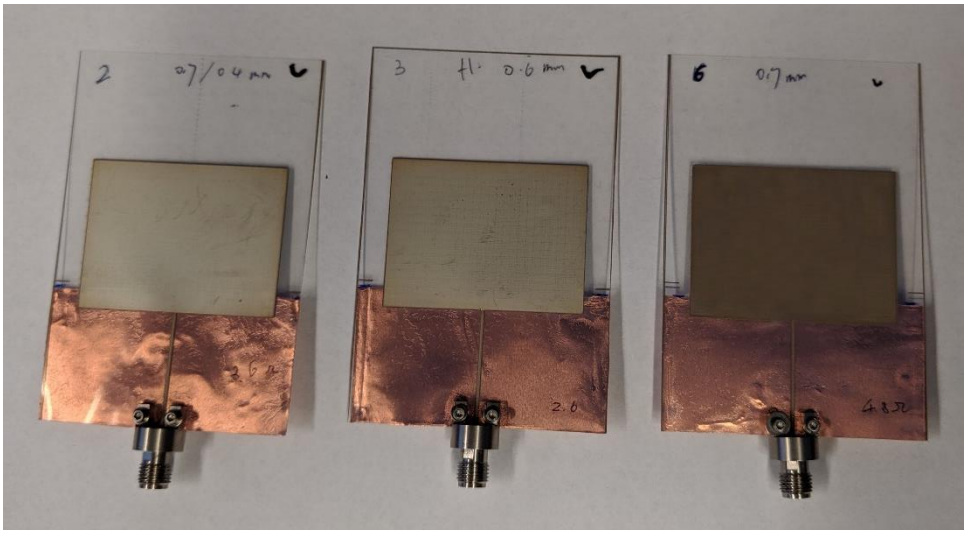

Figure 19 - The three fabricated antenna samples P1, P2 and P3.

In this work, for all of the high-frequency measurements, an Agilent™ N9923A RF Vector Network Analyzer (VNA) is used and calibrated with an HP™ 85052D Calibration Kit, using the SOLT (Short-Open-Load-Thru) standards [61]. The free space measurement setup is shown in Figure 20. The initial electrical high-frequency measurement results of the antenna are presented in Figure 21. As seen, the resonant frequency for sample P1 is 4.82 GHz, for P2 is 5.06 GHz, and for P3 is 4.93 GHz. The discrepancies come from the size of the patch. As seen in Figure 22, a maximum serration of 69 µm occurs along the edge of the printed ink structure. It should be pointed out that the printer used in this work is inexpensive, and thus, tighter control of dimensions is not possible. The purpose of this work is to demonstrate the simulation and measurement methodology, as opposed to creating a high-quality printed sample.

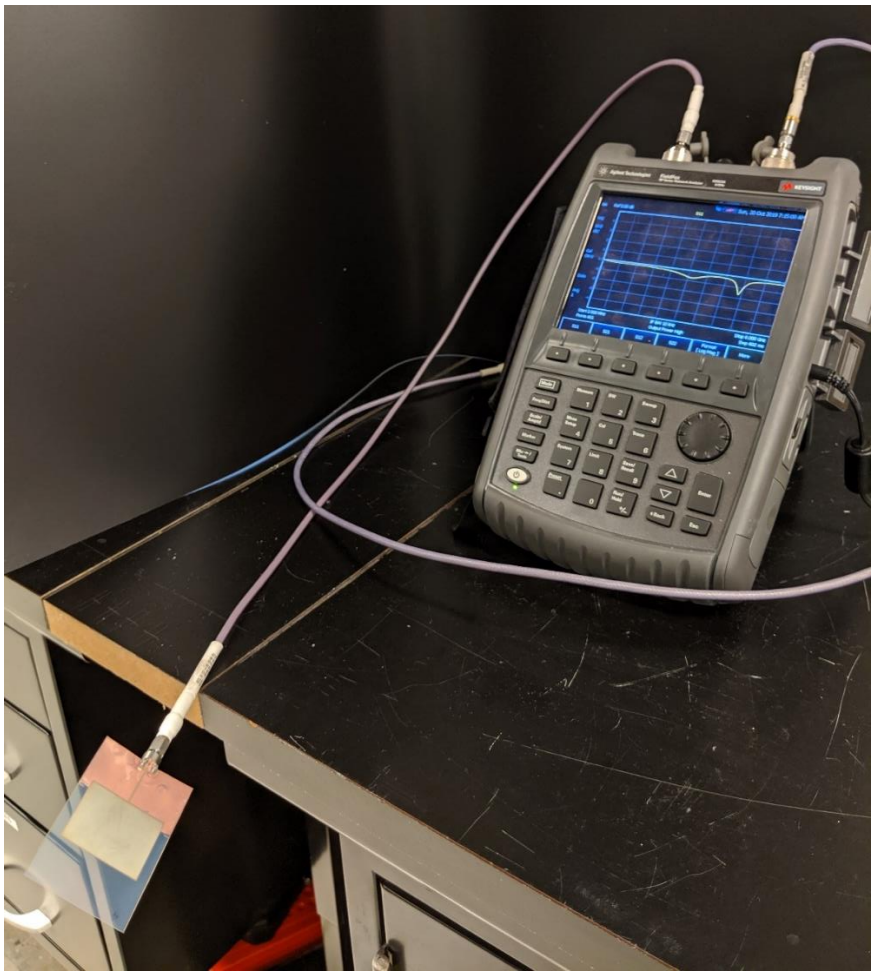

Figure 20 - The configuration of the fabricated antenna measured in free space by the Agilent™ N9923A RF Vector Network Analyzer.

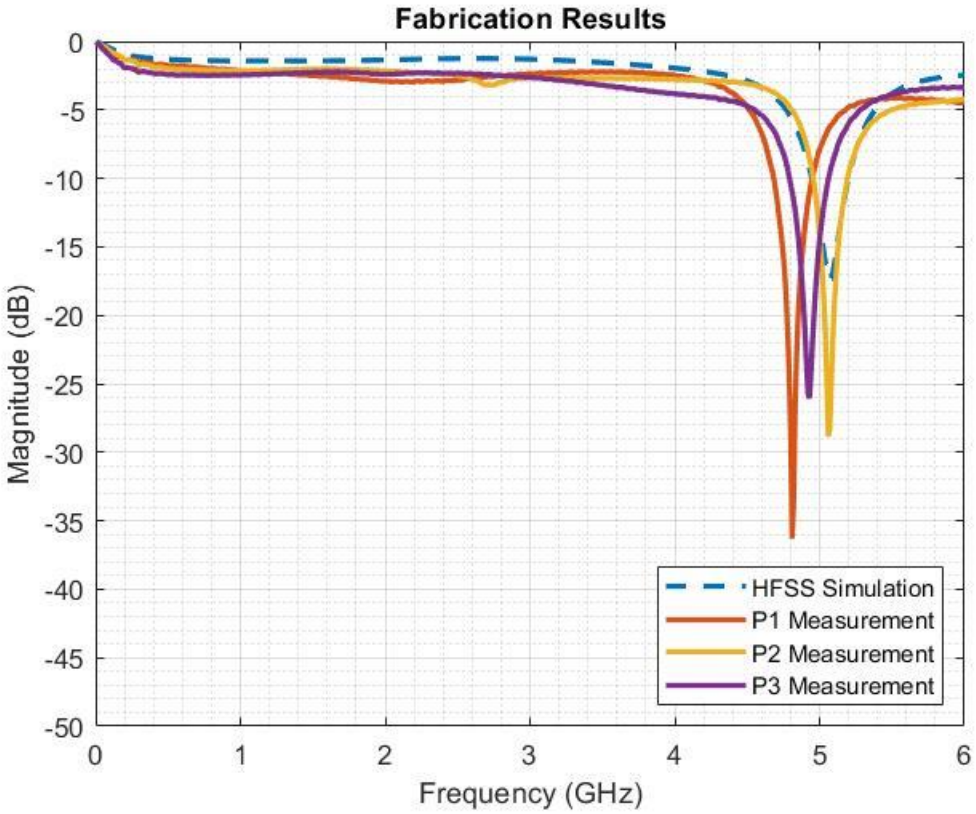

Figure 21 - Electrical high-frequency measurement results of the three fabricated antennas and their comparison to the simulation result.

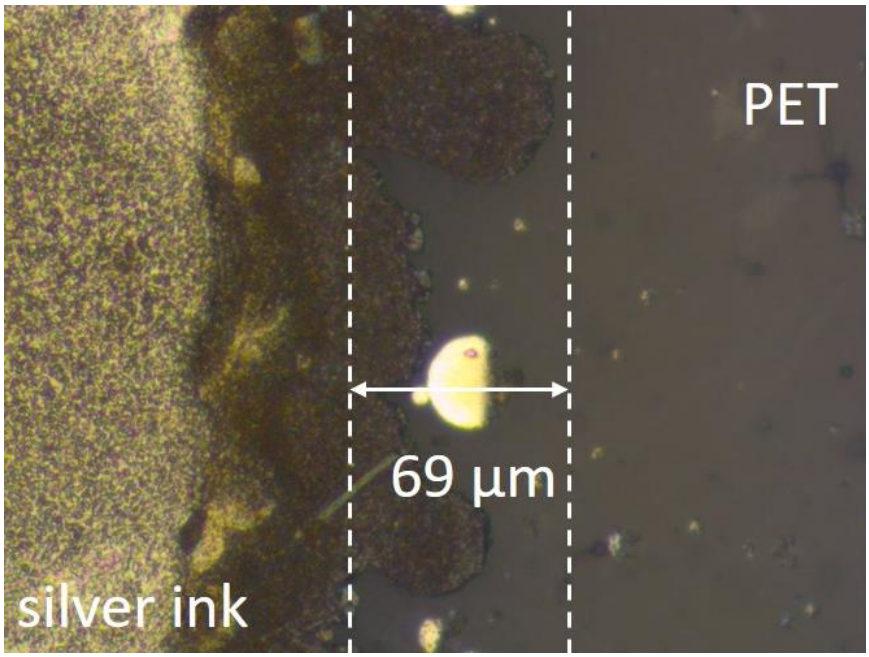

Figure 22 - Top view of the optical inspection of the right edge of the patch.

CHAPTER 5. MANDREL BENDING TEST AND RESULTS

5.1 Mandrel Bending Test over Different Sizes of Mandrel

5.1.1 Experimental Setup and Procedure

Antenna sample P1 is tested in the mandrel bending experiment over different sizes of mandrels. At the start of the bending experiments, the VNA is used to measure S_{11} of the antenna in the flat configuration. The sample is placed on a flat polycarbonate sheet with a thickness of 0.125 in. as shown in Figure 23. The polycarbonate sheet is used in the flat configuration to account for the potential effect on the electrical characteristics of the antenna in the proximity of another material, and then to compare the electrical characteristics of the same antenna under bent configuration over a cylindrical mandrel of the same material with the wall thickness of 0.125 in.

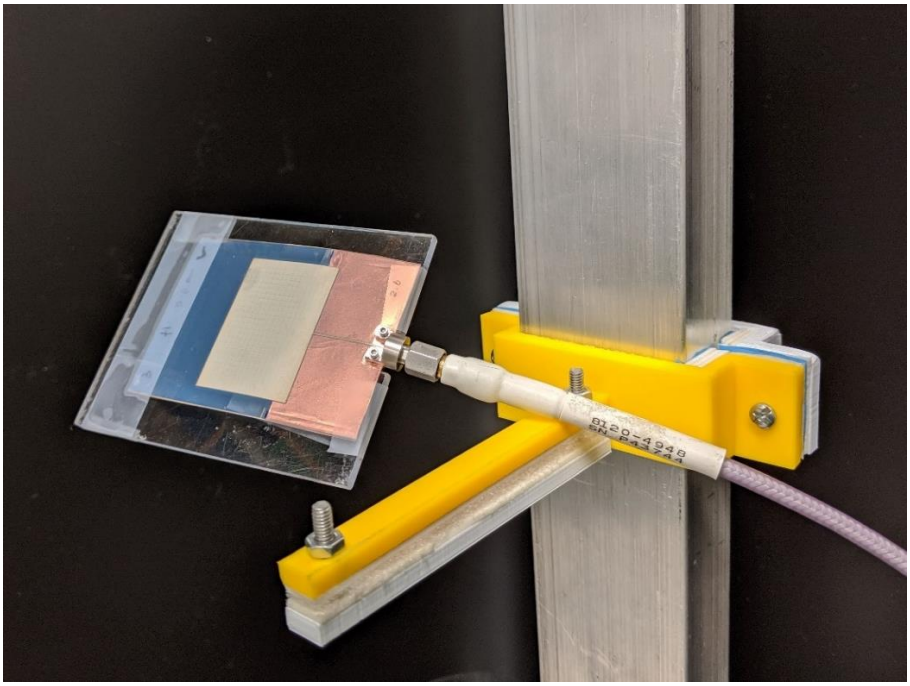

Figure 23 - The antenna is seated on a sheet of polycarbonate for the flat measurements in the uniaxial bending test.

After the flat-configuration measurements, the antenna is sequentially wrapped around various polycarbonate cylindrical mandrels with an outer radius of 4, 3, 2.5, 2, 1.5, 1, and 0.625 in. All polycarbonate cylindrical mandrels used in this experiment are presented in Figure 24. In all of the experiments, the antenna is wrapped such that the ink layer would face outward as demonstrated in Figure 25, and therefore, circumferential tensile strain is applied on the silver ink layer. The experiment is started from the largest radius to minimize potential damage to the printed structure, and the measurements are then sequentially conducted at smaller radii. After measuring S_{11} with the antenna being wrapped around a cylinder of a particular radius, S_{11} is measured again in the flat configuration before the antenna is wrapped around the next smaller cylinder.

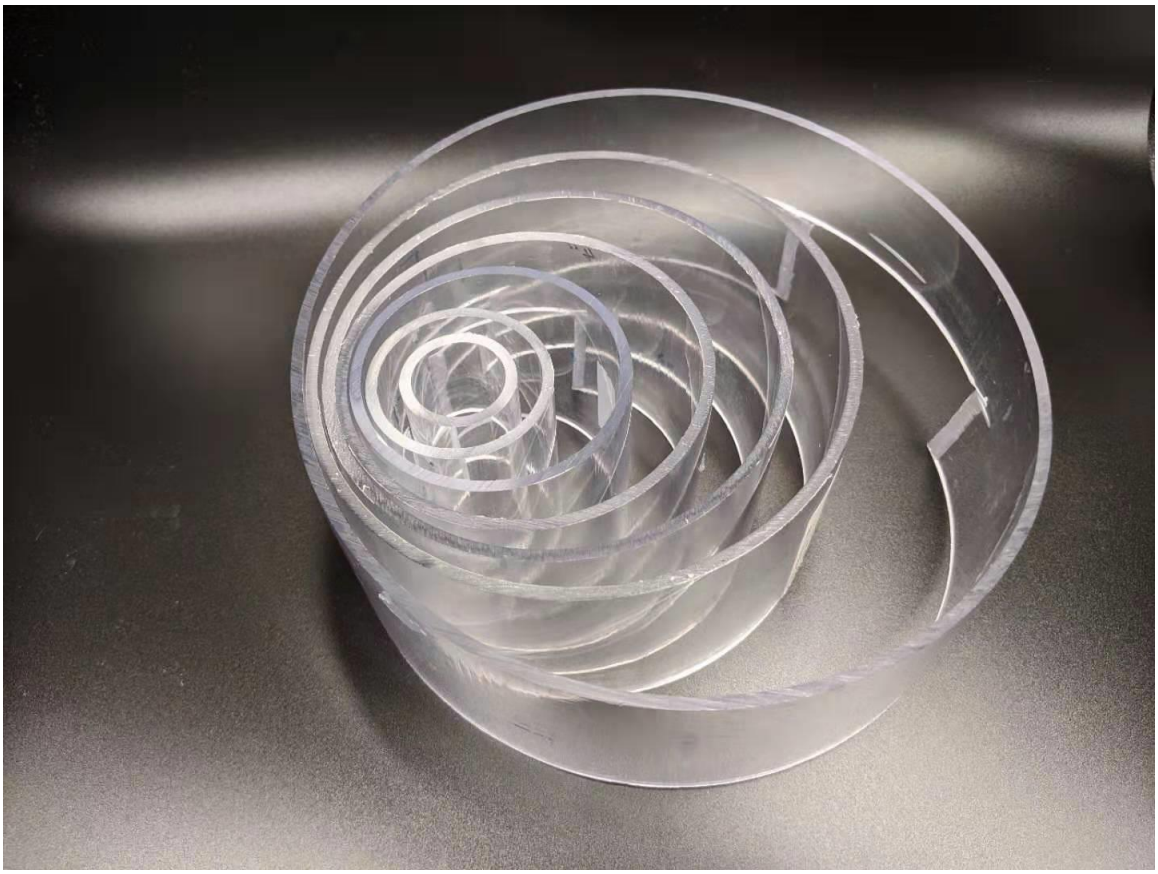

Figure 24 - Polycarbonate mandrel of different radii.

This sequence of bent and flat configuration measurements is repeated through all cylinders of decreasing radii. Once S_{11} is measured around the smallest cylinder with a radius of 0.625 in. and once it is observed that S_{11} has minimal change, the experiment is then repeated by wrapping the antenna around the cylinders of increasing radii. This completes one cycle of S_{11} measurements. This sequence of measurements is repeated five cycles.

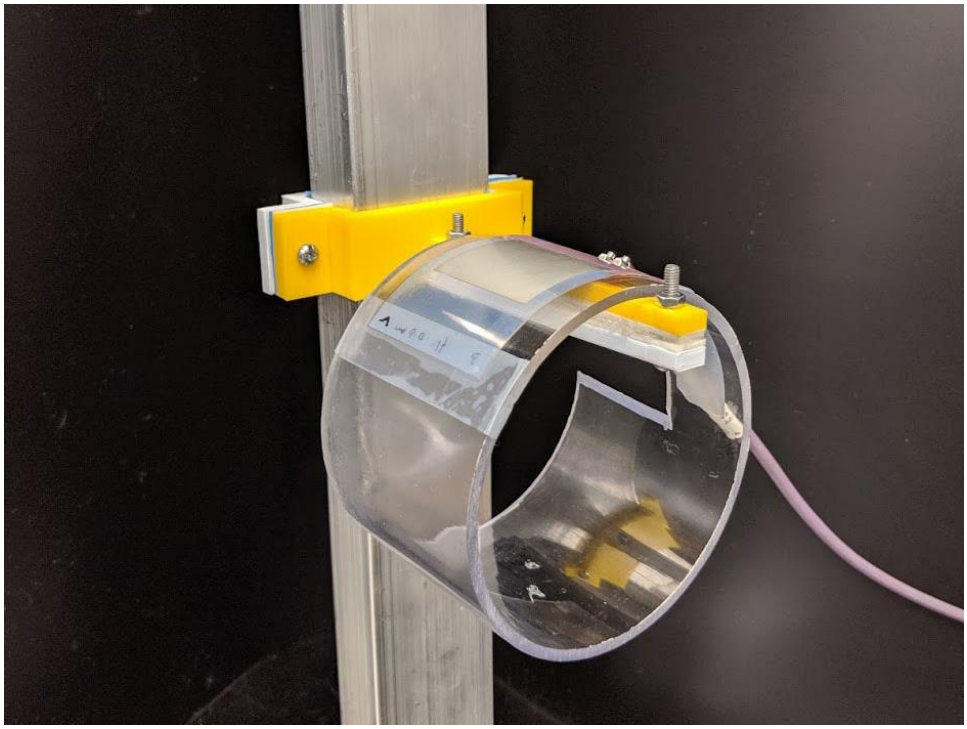

Figure 25 - The antenna is wrapped around the polycarbonate mandrel for the bent measurements in the uniaxial bending test.

5.1.2 Experimental Test Results

The results of five cycles of S_{11} measurements are presented in Figures 26 – 31. The results are zoomed in to 4 – 6 GHz region, since at below 4 GHz, all S_{11} measurements are above -10 dB, and this is applied to all the S_{11} plots in Chapter 5, Chapter 7 and Chapter 9.

To avoid overcrowding of curves, the flat measurements are shown at the beginning and the end of each cycle, and the measured data are shown in Figures 26 through 30. Figure 31 shows measured S_{11} for flat configurations at the beginning and end of all cycles. Initial flat measurements of each cycle are denoted as "f0," and the final flat measurements are denoted as "ff." The in-situ bending S_{11} measurements are denoted as "b" followed by bending radius dimension which is followed by a – sign or a + sign. The – sign indicates that the radius is decreasing from one measurement to the next, while the + sign indicates that the radius is increasing from one measurement to the next.

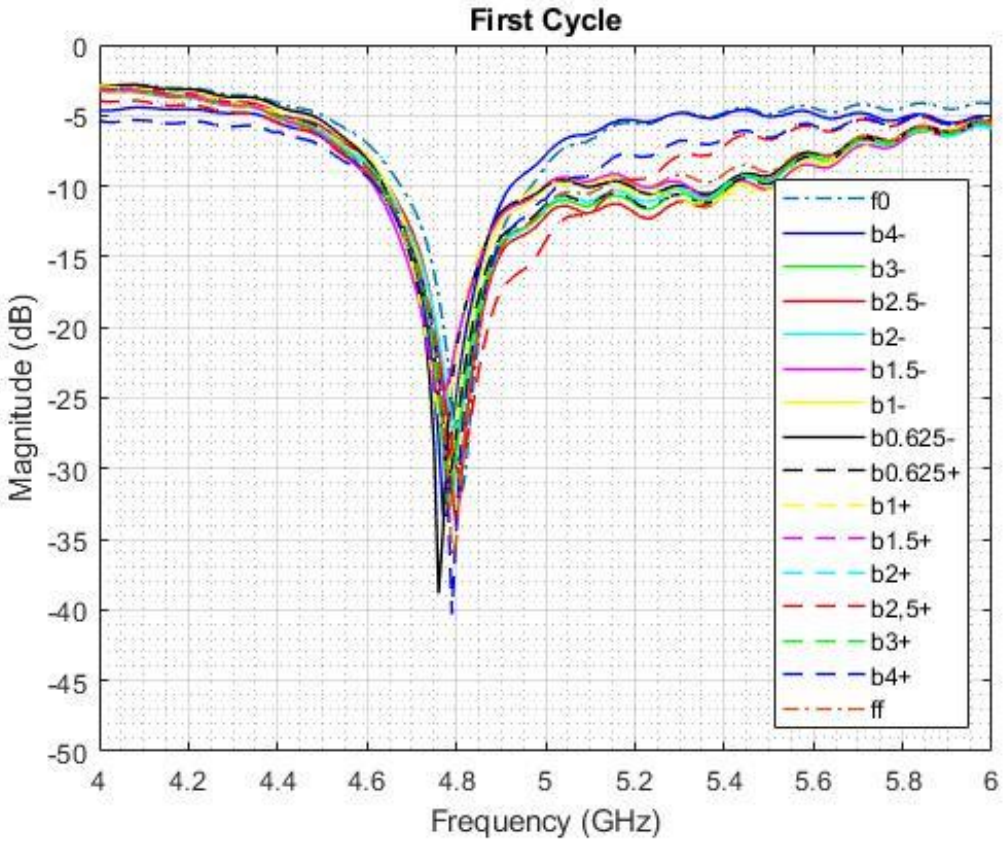

Figure 26 - Cycle 1 S_{11} measurement results of the P1 sample tested in the bending test over different sizes of mandrel.

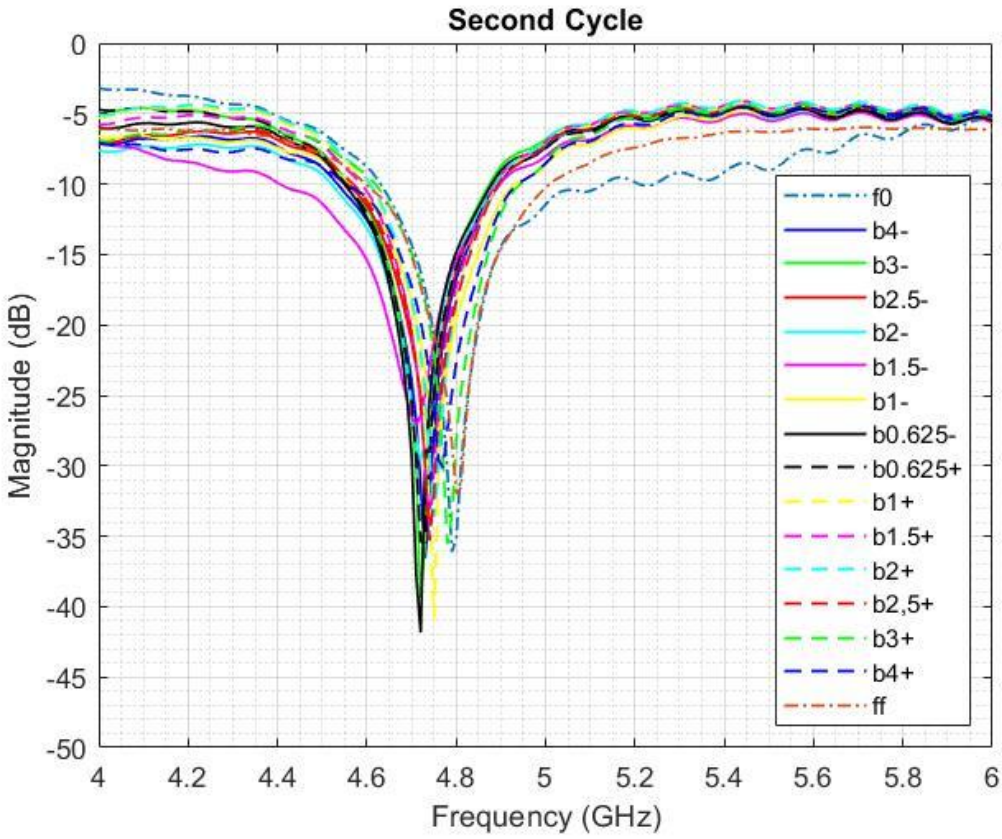

Figure 27 - Cycle 2 S_{11} measurement results of the P1 sample tested in the bending test over different sizes of mandrel.

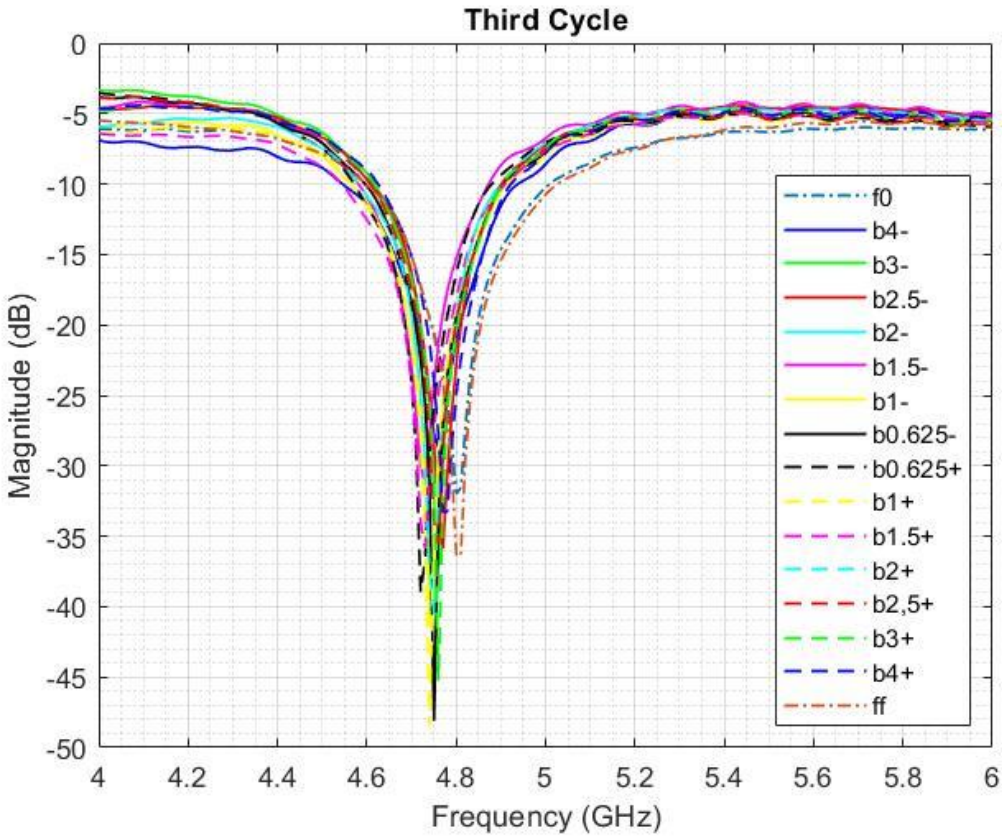

Figure 28 - Cycle 3 S_{11} measurement results of the P1 sample tested in the bending test over different sizes of mandrel.

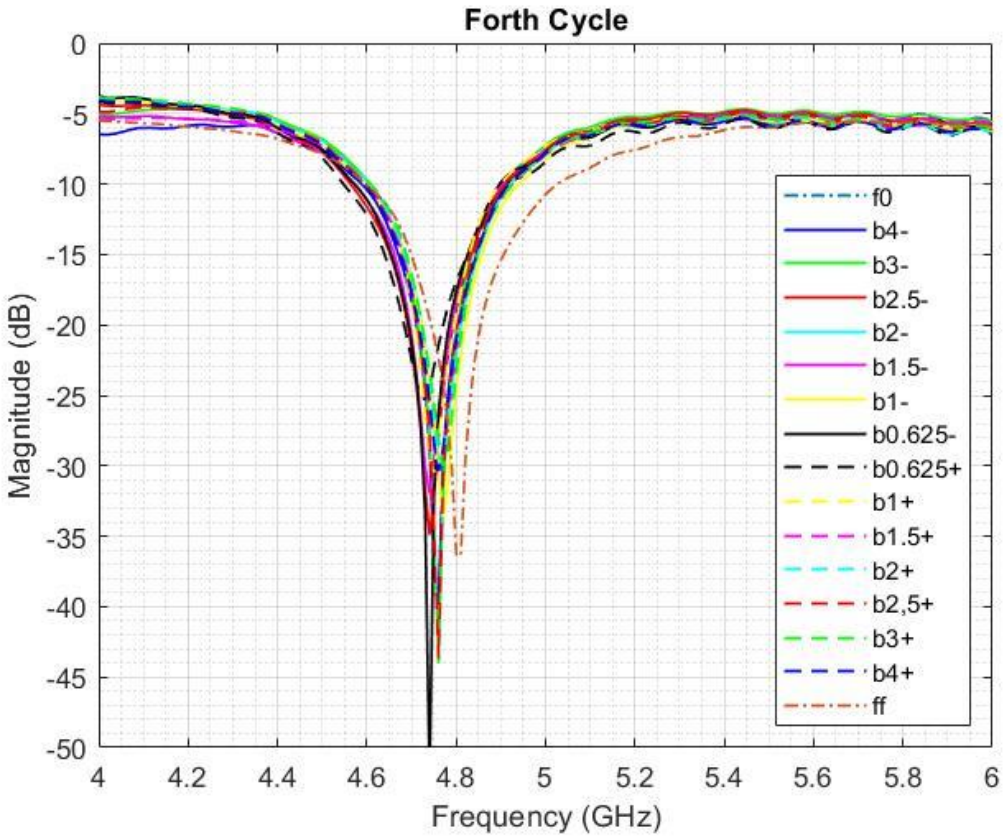

Figure 29 - Cycle 4 S_{11} measurement results of the P1 sample tested in the bending test over different sizes of mandrel.

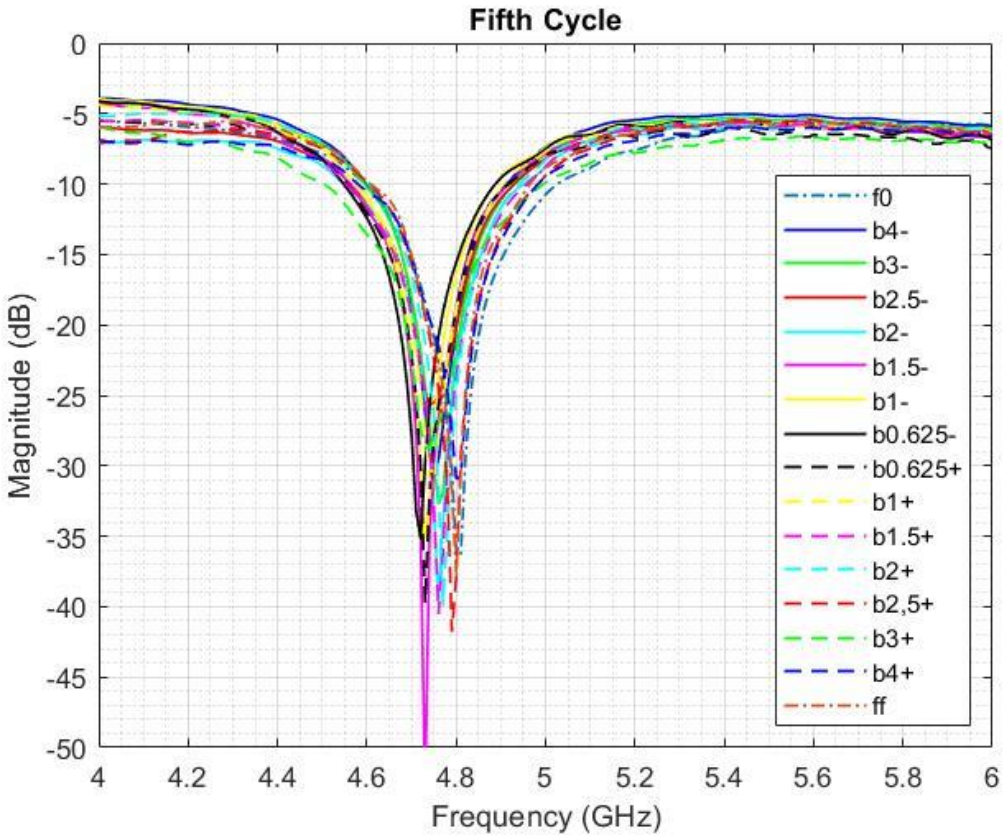

Figure 30 - Cycle 5 S_{11} measurement results of the P1 sample tested in the bending test over different sizes of mandrel.

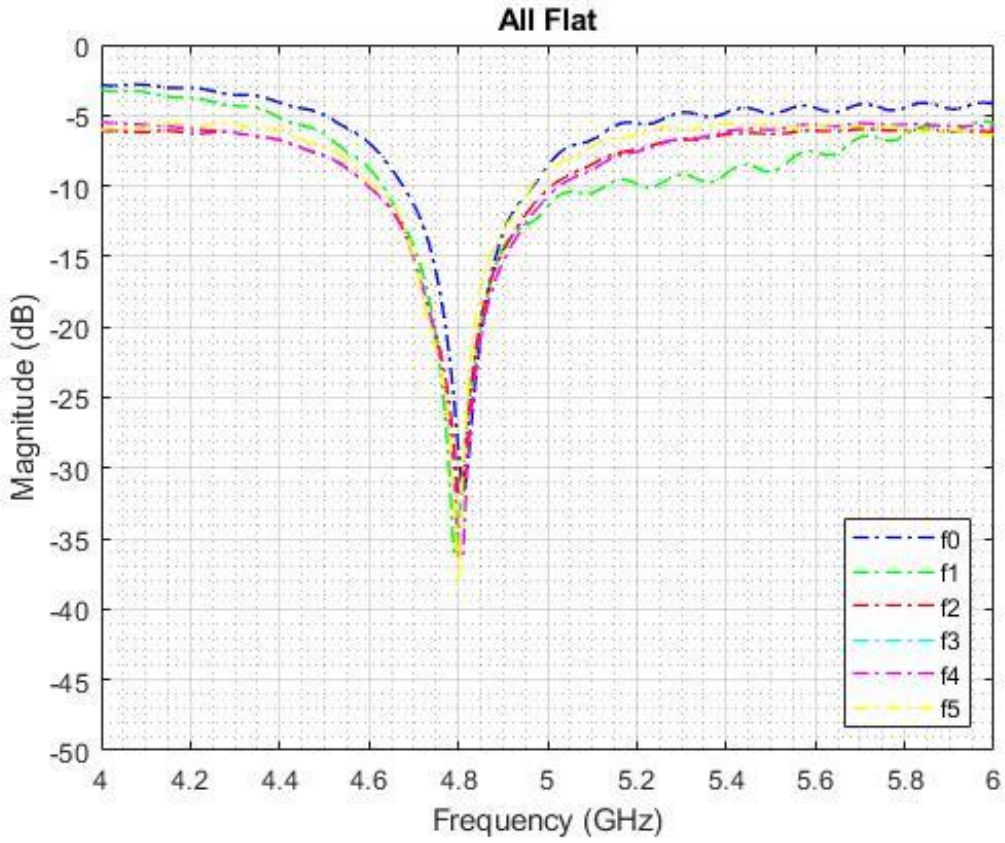

Figure 31 - All the S_{11} flat measurement results of the P1 sample tested in the bending test over different sizes of mandrel.

The initial S_{11} measurement shows a resonant frequency of 4.81 GHz. Throughout the experiments, the overall shape of S_{11} is similar, but the resonant frequency shows minor changes. In general, with smaller radius bending, the resonant frequency decreases in a given cycle, and as the cycling progresses, the resonant frequency continues to decrease for a given radius bending. The maximum shift of resonant frequency to a lower value is observed to be 80 MHz at Cycle 5 (last cycle) at a bending radius of 0.625 in.

It is also seen that all the flat S_{11} measurements have the resonant frequency within the range of 4.79 – 4.81 GHz. In other words, it can be considered that there is practically no change in the resonant frequency in the flat configuration, and very limited damages in the ink structures.

5.2 Cyclic Mandrel Bending Test over Mandrel Size of 0.625 in. Radius

5.2.1 Experimental Procedure and Results of Sample P1

As the number of bending is relatively small in the test in Section 5.1.2, and very limited change in flat measurements is seen, sample P1 is further tested by being wrapped around the mandrel of 0.625 in radius for 2000 times. In this test, only the flat S_{11} measurements are taken, every 100 times below the 500^{th} cycle, and every 500 times between the 500^{th} – 2000^{th} cycles. The flat measurement is taken with the polycarbonate sheet underneath.

The measured S_{11} results are presented in Figure 32. “f”s in the denotation indicate that the measurements are taken at flat, and the numbers coming after indicate the number of cycle. Although all the S_{11} measurements in the flat configuration have similar shapes, the range of resonant frequencies is 4.79 – 4.84 GHz, which is greater in comparison to the results from the previous set of experiment done to the sample P1. The magnitude of the resonant frequency changes from around -40 dB to around -20 dB after the 1000^{th} cycle.

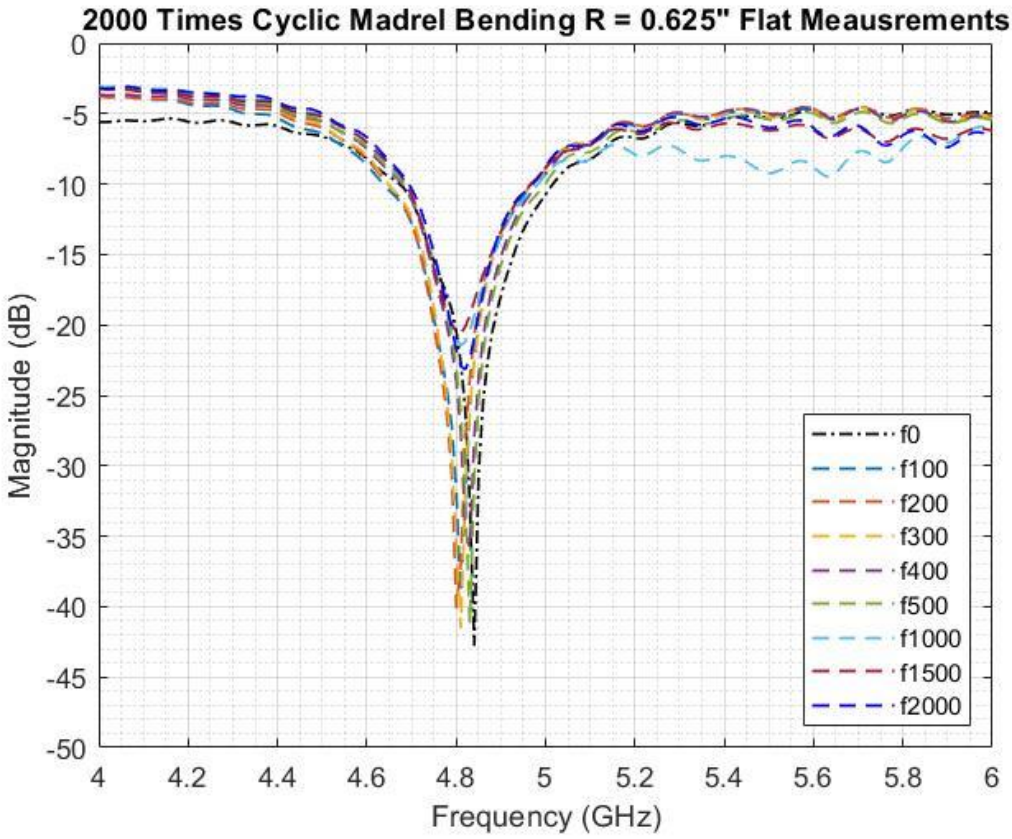

Figure 32 - S_{11} flat measurements of the P1 sample tested in the cyclic bending test over the mandrel of 0.625 in. radius.

5.2.2 Experimental Procedure and Results of Sample P2

The undamaged sample P2 is also tested in the mandrel bending cyclic test for 2000 times over the mandrel of 0.625 in radius with the same procedure. The results are presented in Figure 33. As seen, the shape of the S_{11} response does not change, and the resonant frequency falls into the range of 5.01 – 5.09 GHz, and the initial S_{11} response at flat configuration of sample P2 is 5.06 GHz. There is not great change in the magnitude of the resonant frequency.

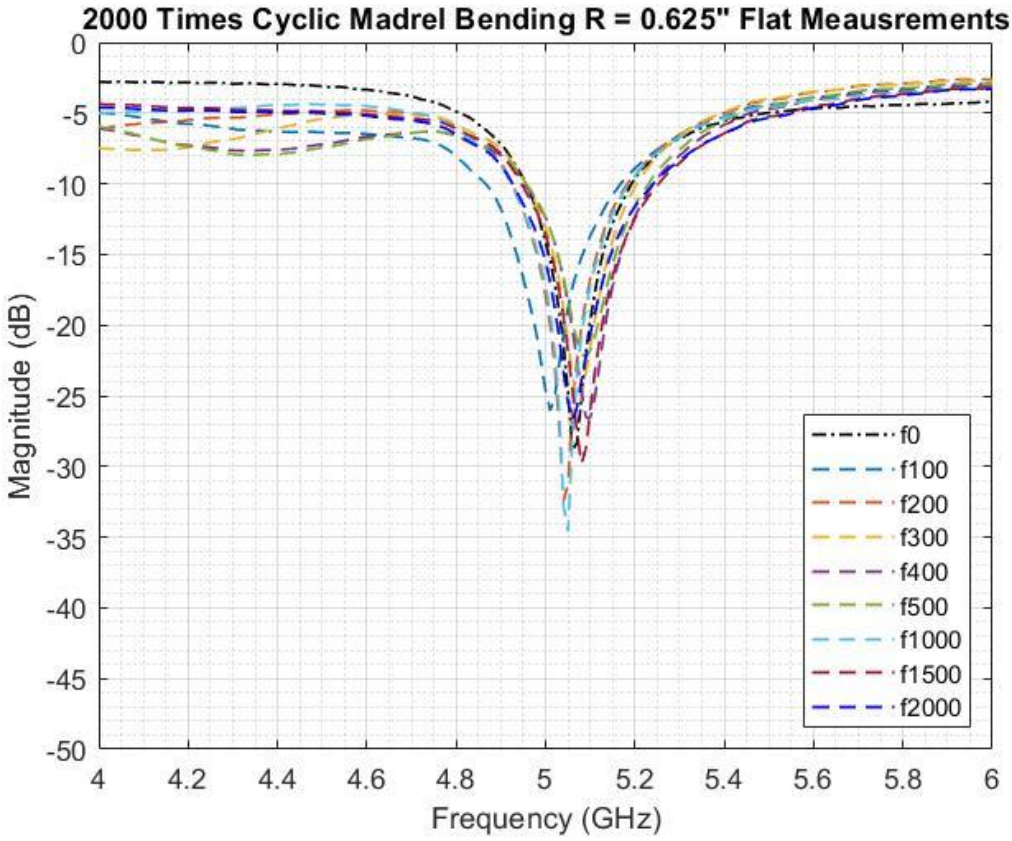

Figure 33 - S_{11} flat measurements of the P2 sample tested in the cyclic bending test over the mandrel of 0.625 in. radius.

SEM images are taken to the sample P2 after the bending test to examine the ink layer's structure changes. Cracks are observed throughout the printed structures, but different areas have different crack densities. Figure 34 focuses on the patch area without the underneath copper ground plane. Figure 35 focuses on the patch area with the underneath copper ground plane. Figure 36 focuses on the feedline area. As seen, cracks are observed in all three areas, and the directions of the cracks are perpendicular to the bending direction, which is along the feedline direction. The three areas can be sorted by crack density from high to low as: the patch with ground plane, the patch without ground plane, and the feedline area. Since the more cracks there are in the printed structure, the

lower conductivity it has, the three areas have the inverse ranking of the conductivity values from high to low.

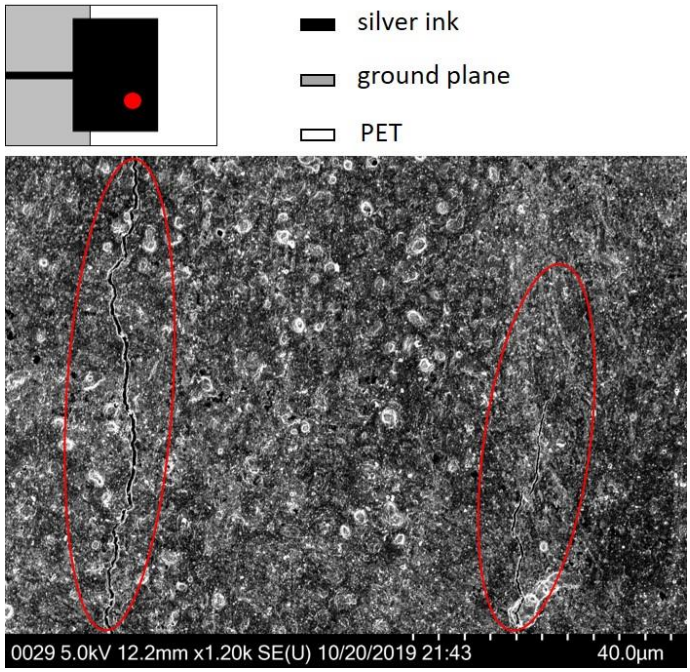

Figure 34 - SEM image of the antenna sample P2 subjected to 2000 cycles of mandrel bending, taken at the patch where there is no copper ground plane.

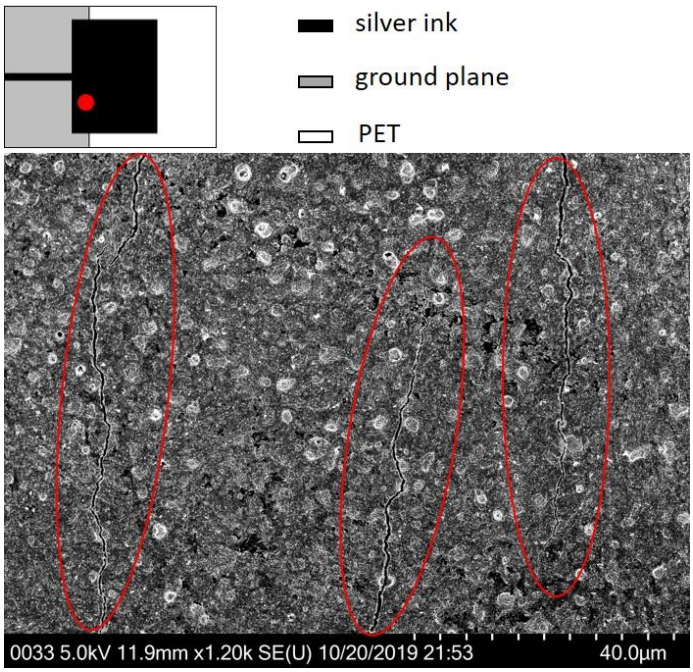

Figure 35 - SEM image of the antenna sample P2 subjected to 2000 cycles of mandrel bending, taken at the patch where there is underneath copper ground plane.

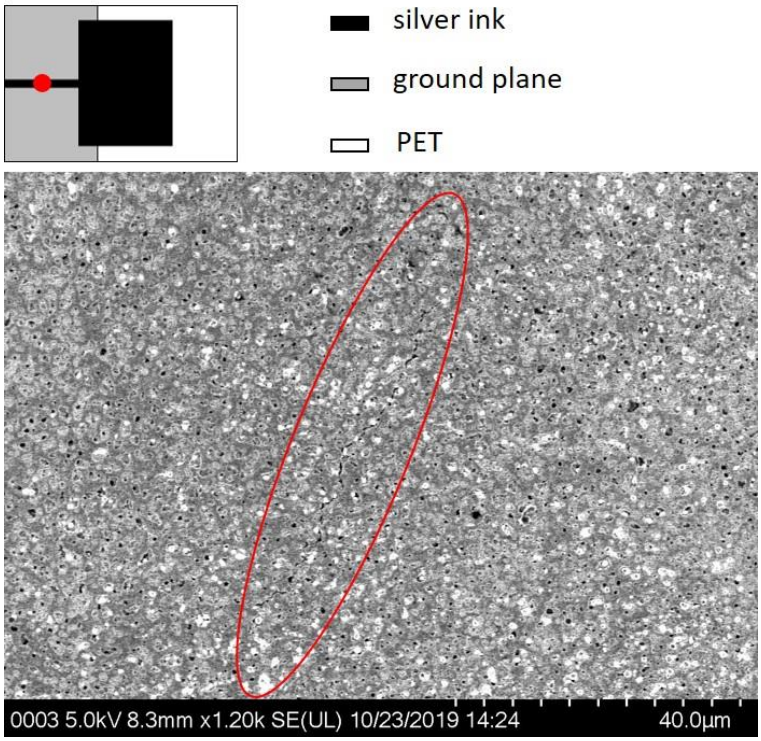

Figure 36 - SEM image of the antenna sample P2 subjected to 2000 cycles of mandrel bending, taken at the feedline location.

CHAPTER 6. MECHANICAL FINITE-ELEMENT ANALYSIS OF MANDREL BENDING TEST

A mechanical 3D finite-element model is built in ANSYS™ Workbench to determine the strain distribution of the antenna when in deformation in the mandrel bending test. To build a reliable FEA model, the geometry details, material properties, and loading conditions should be valid, and this chapter discusses these three aspects in details. The chapter also presents the FEA strain results.

6.1 Geometry Modeling

The 3D FEA model is set up to mimic the mandrel bending test with the highest deformation, where the highest strain appears. Therefore, the model includes two major parts, the antenna and the mandrel.

The antenna model is built based on the fabricated antenna samples discussed in Chapter 4. Figure 37 shows the isometric view of the multi-layered antenna 3D model. Figure 38 shows the top and bottom views, and Figure 39 shows the side view of the antenna model. As seen, the antenna model consists of four layers, which include from bottom, copper layer of 107.54 μm, adhesive layer of 59.66 μm, PET layer of 134.79 μm, and silver ink layer of 6.28 μm. The copper layer, adhesive layer and the PET layer have the same width of 50.4 mm; the copper layer and adhesive layer have a length of 26.5 mm, whereas the PET layer has a length of 76 mm. The silver ink layer is formed by a feedline of 0.6 mm × 22.5 cm, and a rectangular patch of 30 cm × 40 cm.

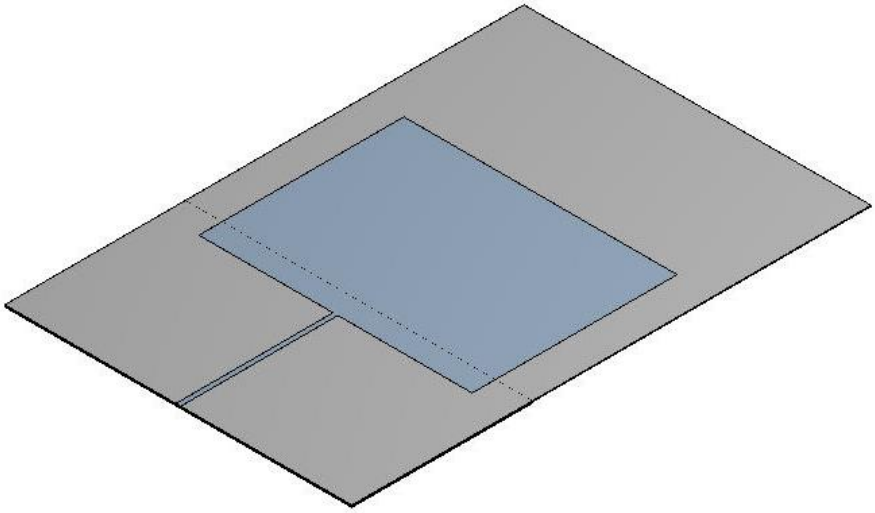

Figure 37 - Isometric view of the multi-layered antenna model.

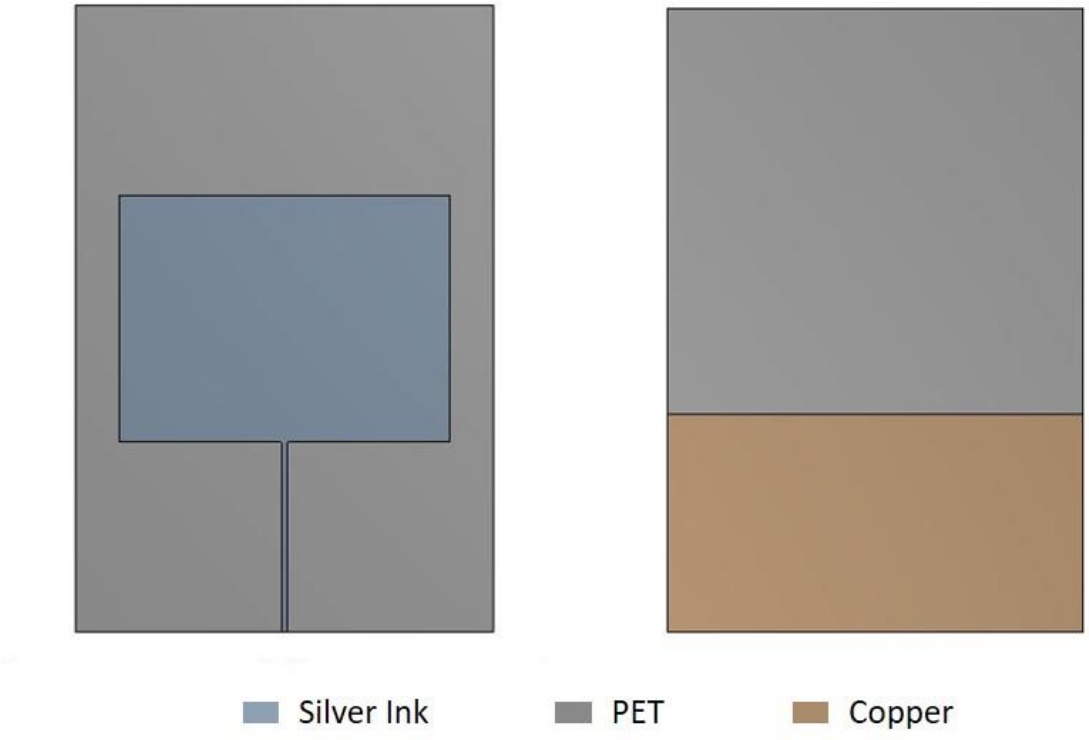

Figure 38 - Top and bottom views of the multi-layered antenna model.

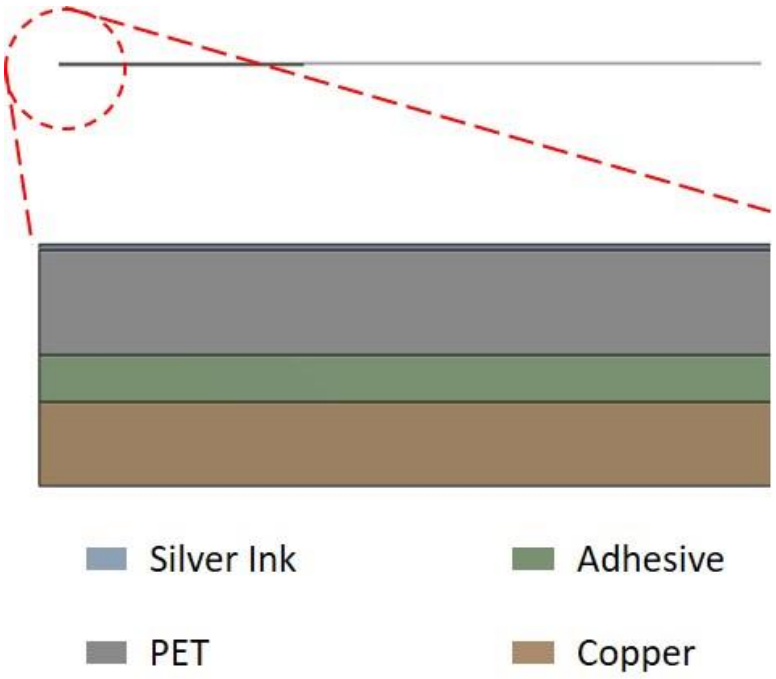

Figure 39 - Side view of the multi-layered antenna.

The mandrel has a radius of 0.625 in. which is the smallest mandrel size used in the experiment discussed in Chapter 5. The length of the mandrel is given to be 50 mm. The model of the mandrel is shown in Figure 40.

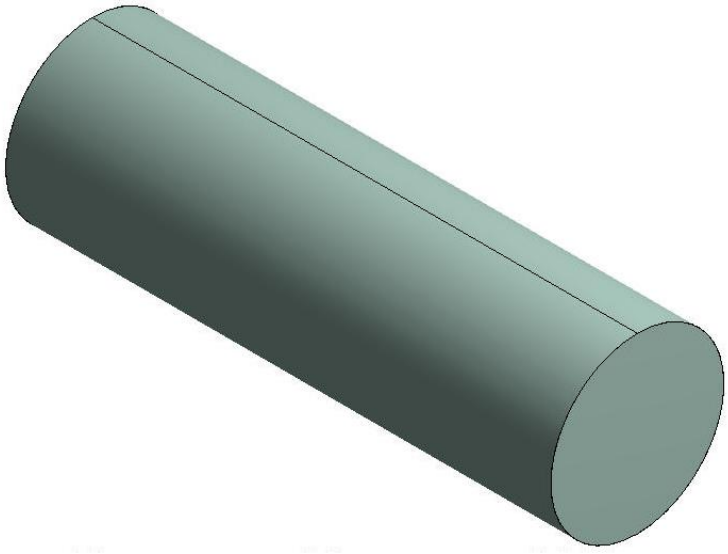

Figure 40 - Isometric view of the mandrel model.

6.2 Material Modeling

6.2.1 Characterization of Printed Silver Ink's Property

Most of the mechanical properties can be looked up in the literature except the printed silver ink. The Poisson's Ratio of the printed silver ink is assumed to be the same as the bulk silver of 0.37 [63]. The elastic modulus of the ink can be obtained by the nanoindentation technique.

In this work, a 1 cm × 1 cm square of the ink is printed with the same procedure discussed in Section 4.1 for the nanoindentation process. The nanoindentation is performed with the Hysitron^{TM} Triboindenter. A 3 × 4 rectangle indentation pattern is created within the target region. By giving a specific force load, the stylus would indent to a corresponding depth. The 12 indentations have different force loads, and the results are shown in Figure 41. Although the material properties are obtained from the unloading portion of the curves, it is critical to make sure that the loading portion of the curves follows the same trend; therefore, the indentation 4 and 8 are the two outliers. Figure 42 shows the indentation plots without the indentation 4 and 8. As seen in Figure 42, the maximum indentation depth is less than 200 nm which is less than 1/10th the thickness of the ink; therefore, all the collected data apply to the printed ink, not the underlying substrate. Table 2 shows the indentation results of the elastic modulus with the ten valid indents. It is seen that the indentation values vary from 2.94 to 10.16 GPa; this is reasonable, because when the stylus lands on the printed structure it can be on top of a silver nanoparticle or on the polymer matrix that is in between nanoparticles. Therefore, the average elastic modulus value is taken for the ten valid indents, and it is 5.03 GPa as seen in Table 2.

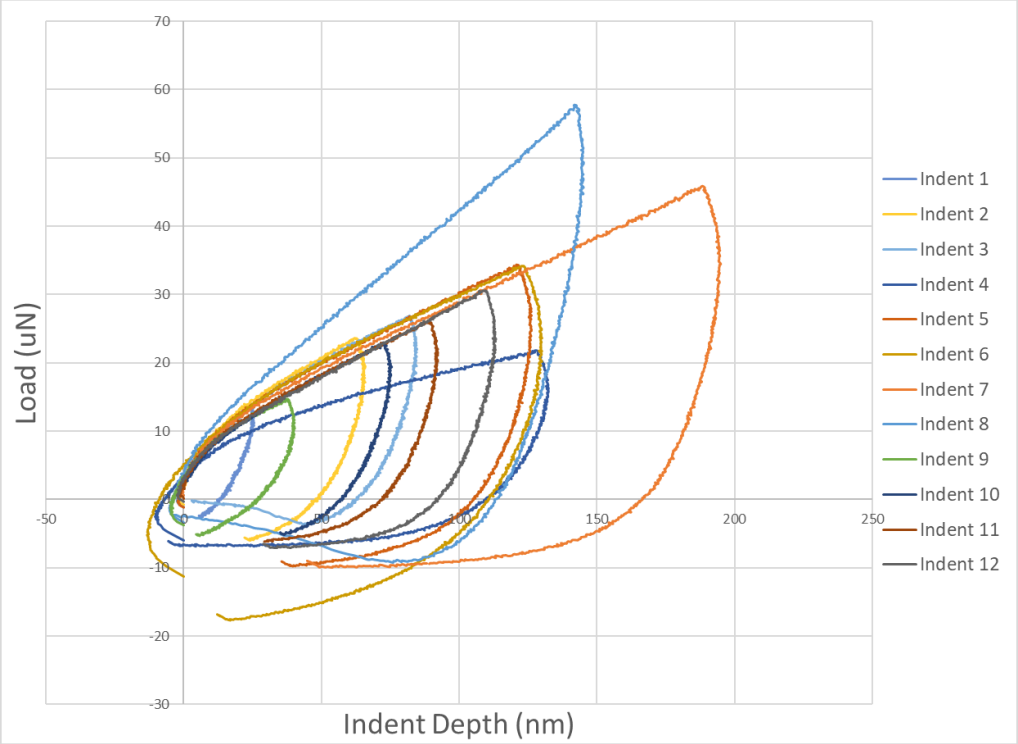

Figure 41 - Nanoindentation data of the 12 indentations on the sample.

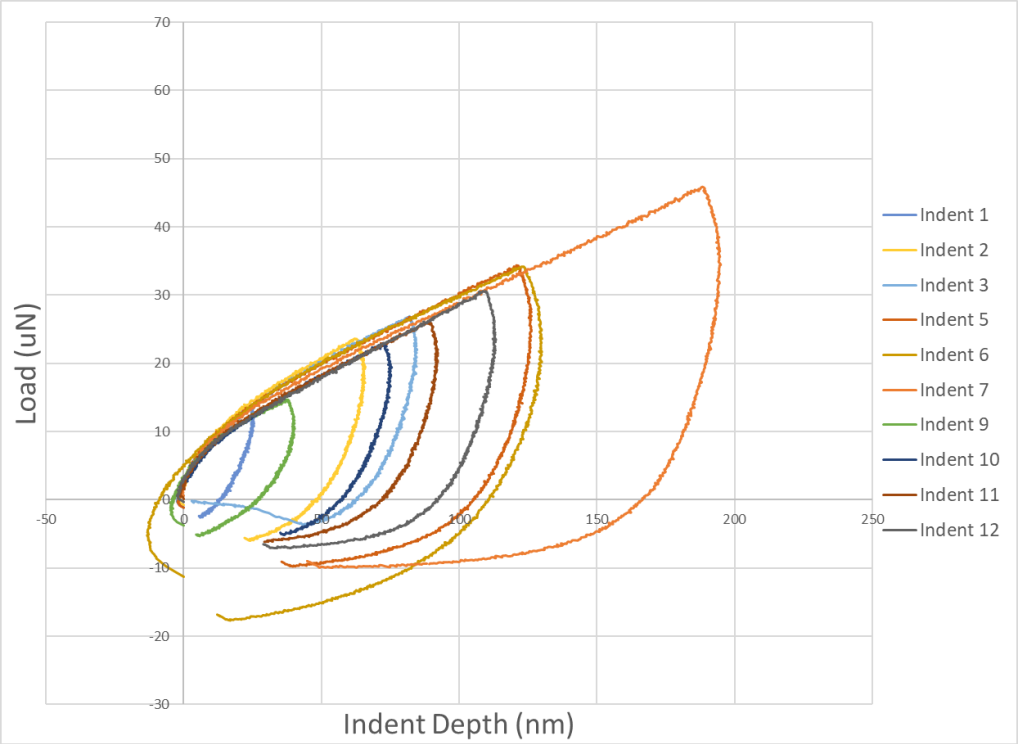

Figure 42 - Nanoindentation results without the two outliers.

Table 2 - Nanoindentation results

Indentation Name	Elastic Modulus (GPa)
1	10.16
2	5.35
3	4.10
5	4.26
6	4.94
7	2.94
9	6.51
10	4.30
11	3.90
12	3.89
Average	5.03

6.2.2 Other Materials' Properties

For all materials, isotropic elastic material models are used in the simulations. A summary of the material used in the simulation is presented in Table 3. As discussed earlier, the silver ink has a Young's Modulus of 5.03 GPa, and a Poisson's Ratio of 0.37. The material properties of the copper foil and the PET substrate can be obtained from the literature [64- 66]. The PET has a Young's Modulus of 2.40 GPa, and a Poisson's Ratio of 0.40. Copper foil has a Young's Modulus of 110 GPa, and a Poisson's Ratio of 0.34. The adhesive layer is assumed to have a modulus of 2.40 GPa. The cylindrical mandrel is assumed to have a very high modulus to indicate its rigid nature in the simulation.

Table 3 - Mechanical material properties for Workbench model.

Material	Young's Modulus (GPa)	Poisson's Ratio
Silver Ink	5.03	0.37 [63]
PET [64]	2.40	0.40
Copper [65][66]	110	0.34

6.3 Loading and Boundary Conditions

To mimic the motion of the antenna wrapping around the mandrel, the model is set up as seen in Figure 43. The four layers of the antenna are modeled as one part. At the initial position, the bottom edge of the substrate without the ground plane is simulated to be bonded to the mandrel as seen. To make sure that the sample could fully conform to the surface of the mandrel, a rotational displacement is applied to the mandrel with a 1°

increment per step through 266° when the entire sample is fully wrapped around the mandrel. A small force of 1N is applied to the end surface of the substrate to keep the sample flat during rolling. The bottom surfaces of the substrate and the ground plane are assigned frictionless contact with the surface of the mandrel. Figure 44(a) and (b) demonstrate two isometric views of the final position of the simulation as the mandrel is rotated to 266°.

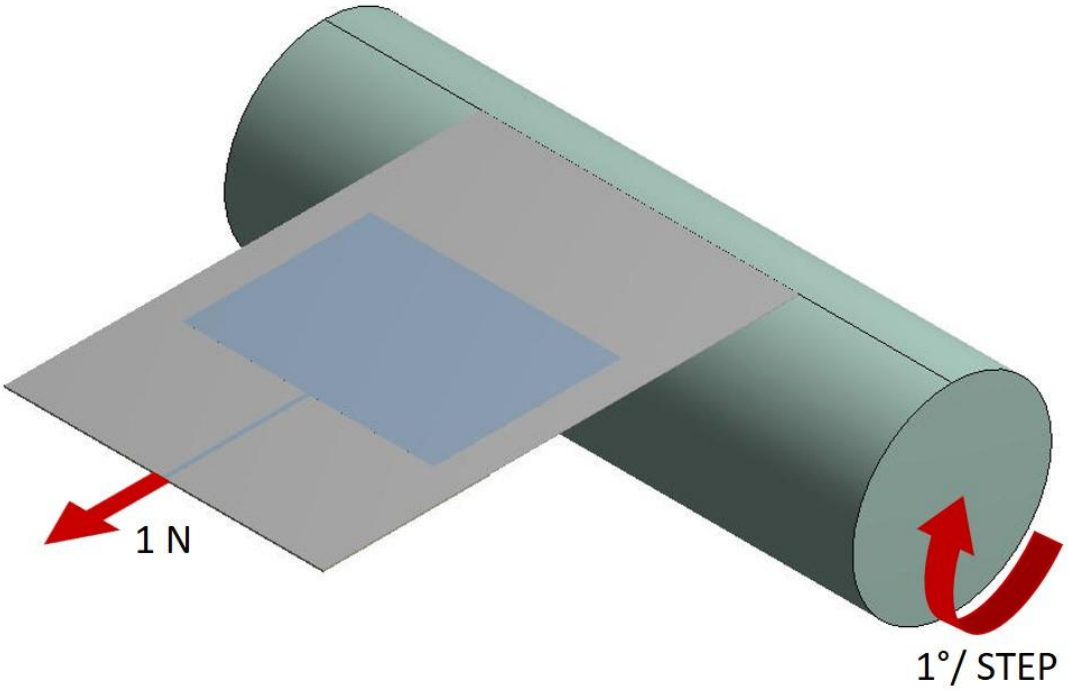

Figure 43 - Initial position and loading conditions of the mandrel bending FEA model.

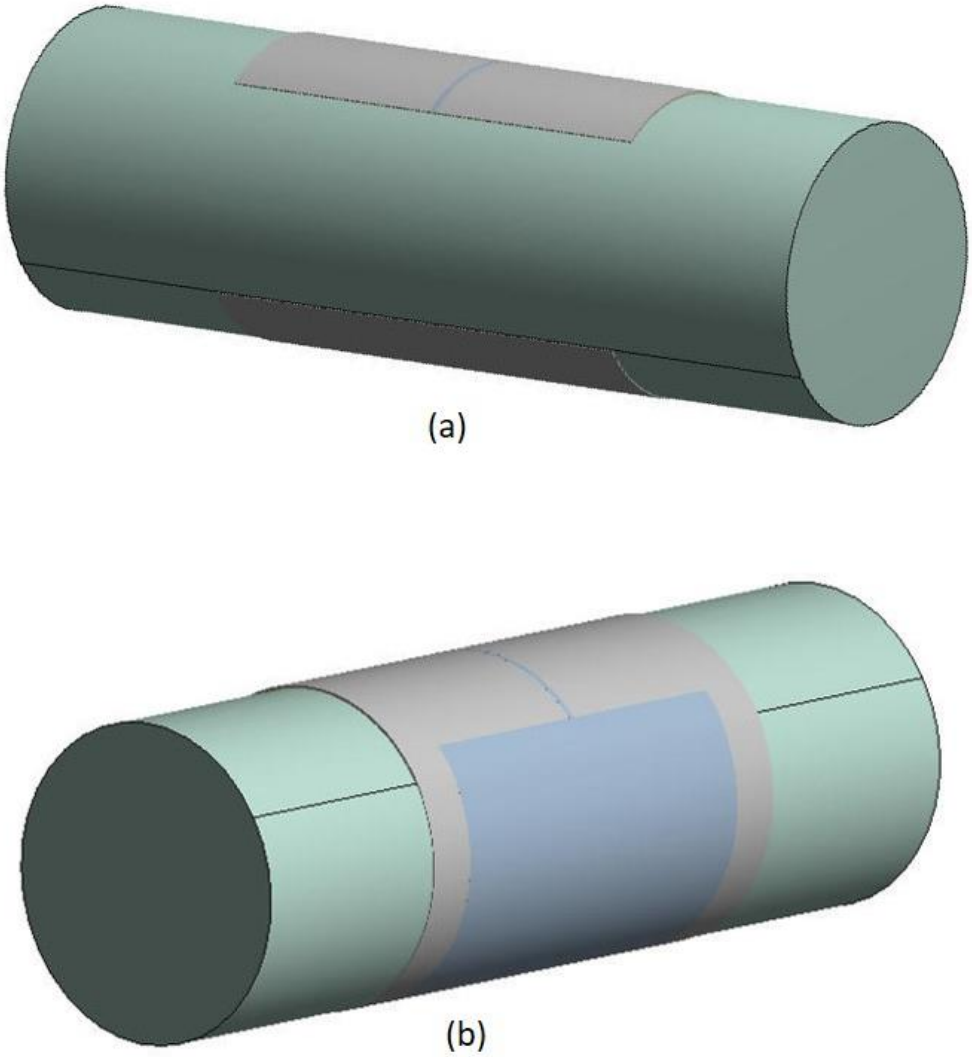

Figure 44 - Isometric views of the final position of the model.

6.4 Initial Meshing Details

An initial mesh details of the antenna-mandrel system FEA model is shown in Figure 45. In the model, the mandrel is assumed as a rigid body in the simulation and is meshed with the 8-node SURF 154 elements. The element size is 5 mm.

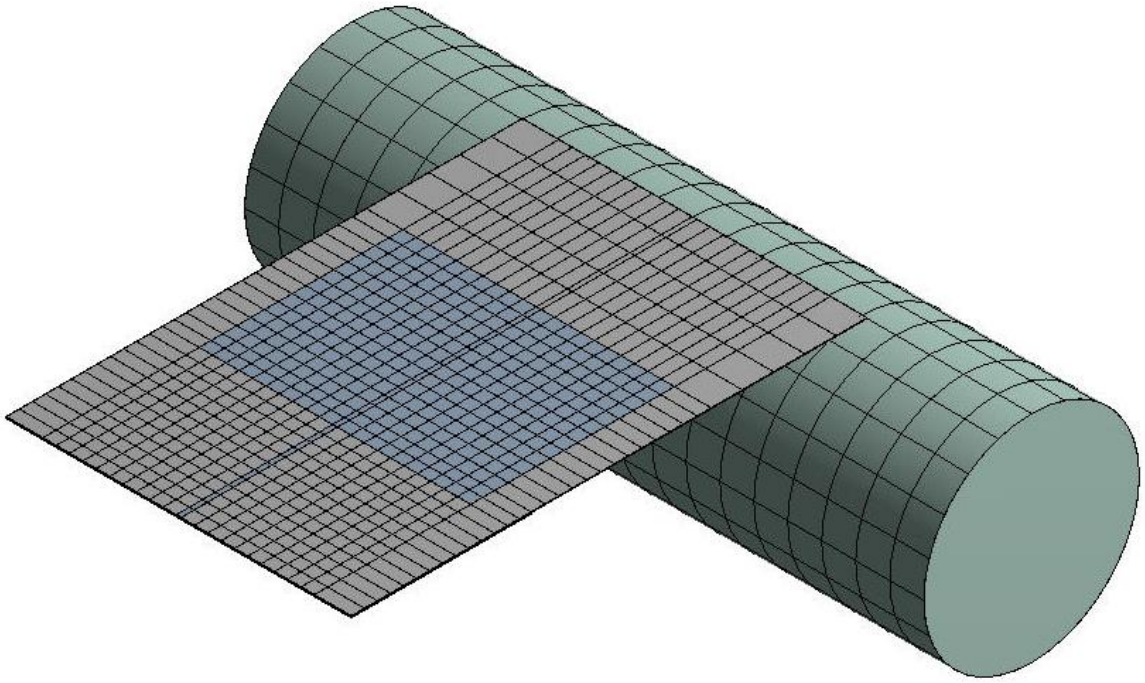

Figure 45 - Initial mesh details of the mandrel bending FEA model.

The multi-layered antenna is meshed with the 20-node SOLID 186 elements. The element size of 2 mm is assigned to the top surface of the silver ink layer. A sweep method is used for the ink layer with the two layers in thickness initially. A multi-zone method is used in the PET layer, adhesive layer and copper layer to help save elements in unfocused area as seen. A sweep method is also used in these three layers, with an element size of 0.1 mm in thickness. In the initial mesh case, the PET is meshed in 2 layers, adhesive in 1 layer, and the ground plane in 2 layers through thickness as shown in Figure 46.

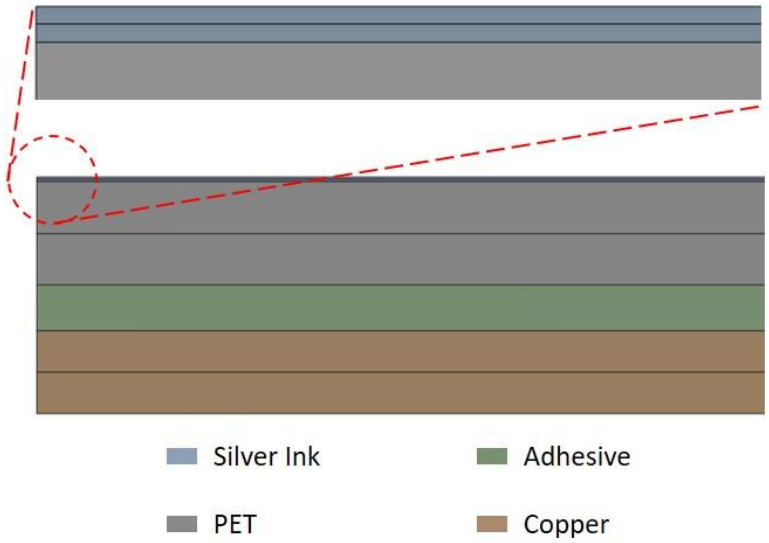

Figure 46 - Side views of the mesh details of the model.

6.5 Mesh Convergence and Simulation Results

Bending strain at any location can be approximately computed by

$$\varepsilon = \frac{d}{\rho} \tag{5}$$

where ε is the strain, d is the distance from the neutral axis of the multilayer structure and ρ is the bending radius at neutral axis. The strains should be greater where there is an underlying copper ground plane moving the neutral plane closer to the cylindrical outer surface. The calculated bending strain is 0.01568 for the ink layer with a copper ground plane underneath. For the sake of expediency, first principal strain contours of the silver ink layer, obtained from numerical simulation with the initial mesh details, are shown in Figure 47.

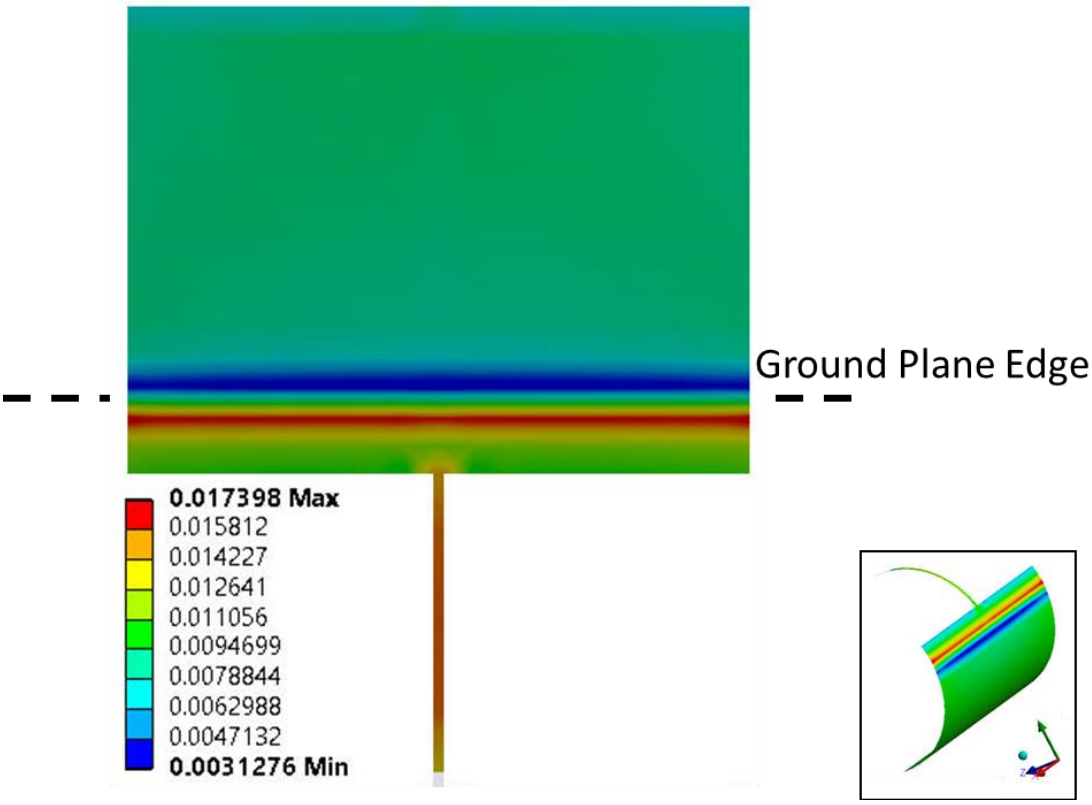

Figure 47 - Simulation result of the first principal strain distribution of the ink layer in the mandrel bending model with the initial mesh (mesh case 1).

It is seen that the average strain value of the feedline is 0.01581 which is closed to the hand calculated values of 0.01568. With the edge effect of the ground plane, the maximum strain value of 0.01740 occurs at the patch where the ground plane ends. The portion of the ink with no copper ground plane underneath has strain values of 0.00947.

The FEA results are sensitive to the mesh densities. Another two sets of meshing are run for the mesh convergence valuation. The case 2 has an additional layer of element in each material compared to the original mesh of case 1. The case 3 has a smaller size of mandrel elements, which is 2 mm rather than 5 mm in the case 1. The results of the mesh cases 2 and 3 are shown in Figure 48 and Figure 49. As seen, the strain distribution contours are similar to the contour of the case 1, but with higher values. The increases in the strain

results are all below 1%, due to the increase of mesh densities. A summary of the mesh convergence results is present in Table 4.

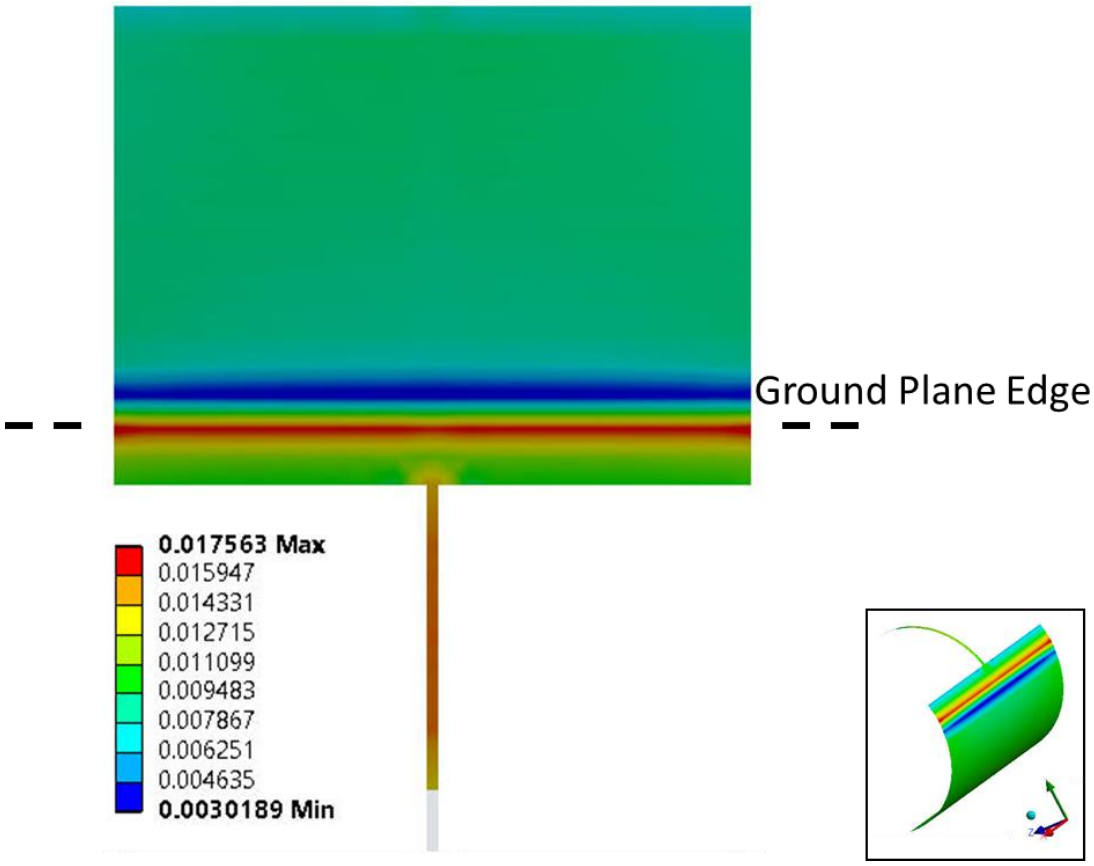

Figure 48 - Simulation result of the first principal strain distribution of the ink layer in the mandrel bending model with the mesh case 2.

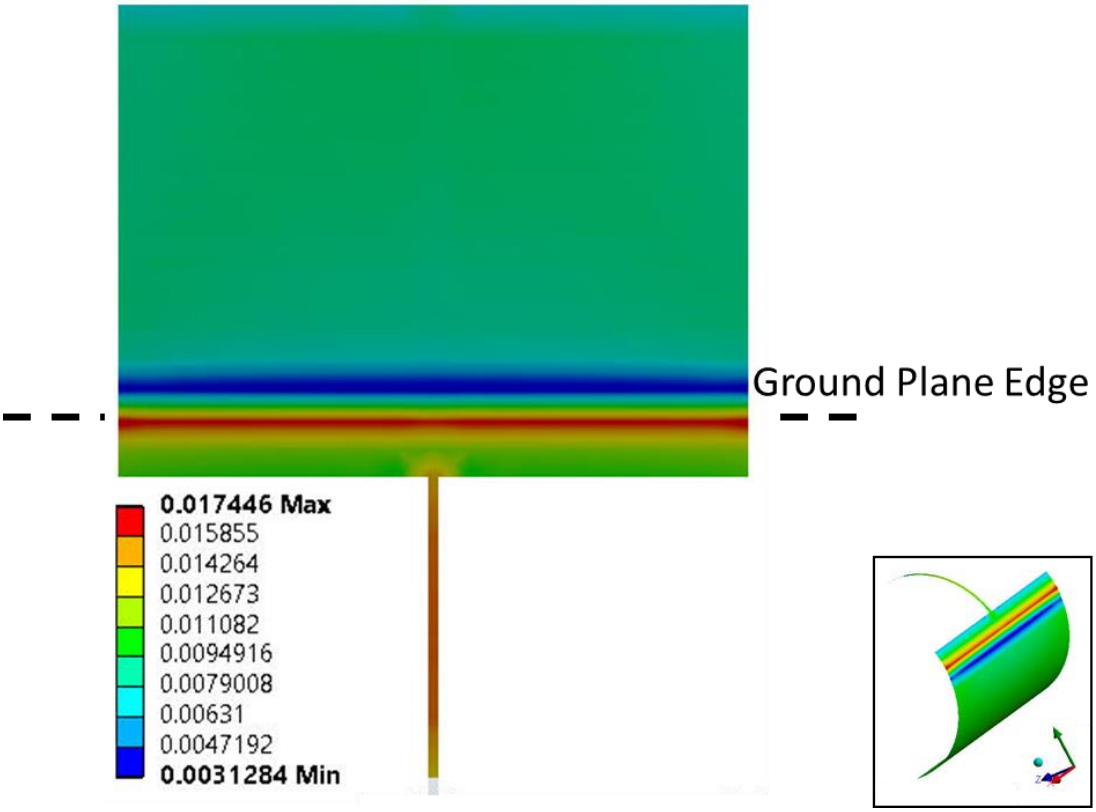

Figure 49 - Simulation result of the first principal strain distribution of the ink layer in the mandrel bending model with the mesh case 3.

Table 4 - Mesh convergence results of the mandrel bending model.

Case	1	2	3
Mandrel Surface Element Size	5 mm	5 mm	2 mm
Ink Layer Number of Elements in Thickness	2	3	2
PET Layer Number of Elements in Thickness	2	3	2
Adhesive Layer Number of Elements in Thickness	1	2	1
Copper Layer Number of Elements in Thickness	2	3	2
Max Strain at Patch with Ground Plane	0.01740	0.01756	0.01745
Average Strain at Feedline	0.01581	0.01595	0.01586
Average Strain at Patch without Ground Plane	0.00947	0.00948	0.00949

It is clear from the mechanical FEA results that, the ink structure experiences different strain values in different areas. This strain distribution results can be compared with the SEM images results in section 5.2. The patch area without the underneath ground plane has the highest strain value, and it has the densest crack shown in the SEM images. In the FEA results, the strain value of the feedline area experiences the second highest strain and the patch area with ground plane the third, but in the SEM images the feedline area has less cracks. This could possibly come to the fact that, with the edge SMA connector mounted at the end of the feedline, the bottom portion of the antenna is not fully conformed to the mandrel during the test. Therefore, during the experiment, the feedline area of the ink structure experiences less strain values than other areas of the ink structure.

CHAPTER 7. BIAXIAL BENDING TEST AND RESULTS

7.1 Experimental Fixture Design and Setup

Special experimental fixtures are designed and fabricated by 3D printing in polylactic acid (PLA) material to conduct the biaxial bending test. Figure 50 shows the 3D CAD model of the fixtures design. The fixtures are designed as a two-part system that the electronics can be sandwiched to the desired biaxial curved surface. Saddle-like mating surfaces of the fixtures are designed such that a 4 in. radius convex curve is swept along a 40 in. radius concave curve in the transverse direction. Holes are designed at the holders of the fixtures, so that in the cyclic bending test, the fixtures can be attached to the universal testing machine. Figure 51 shows the 3D-printed saddle-like shape bending fixtures.

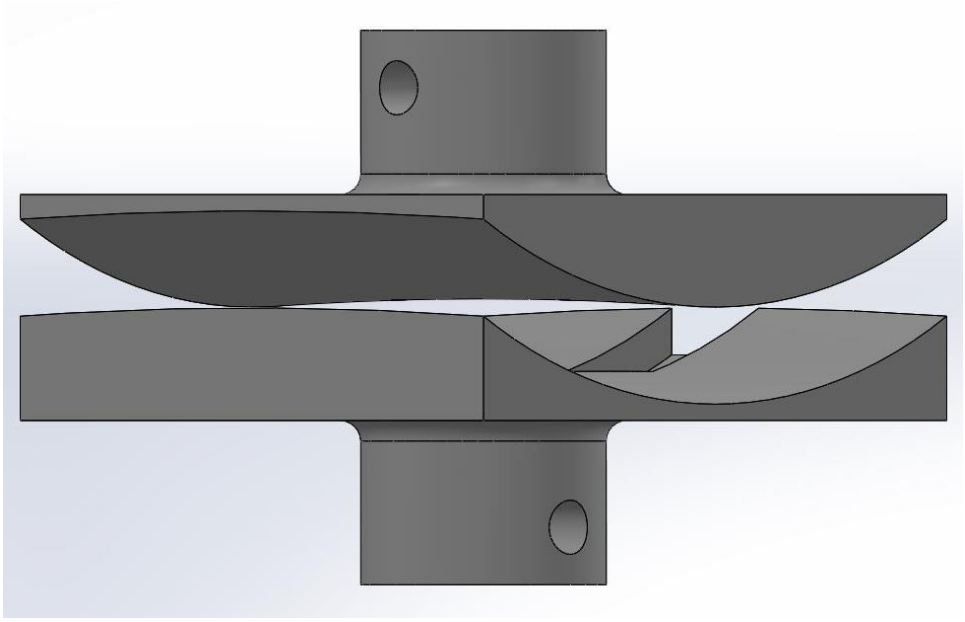

Figure 50 - 3D CAD model of the designed saddle-like shape biaxial bending fixtures.

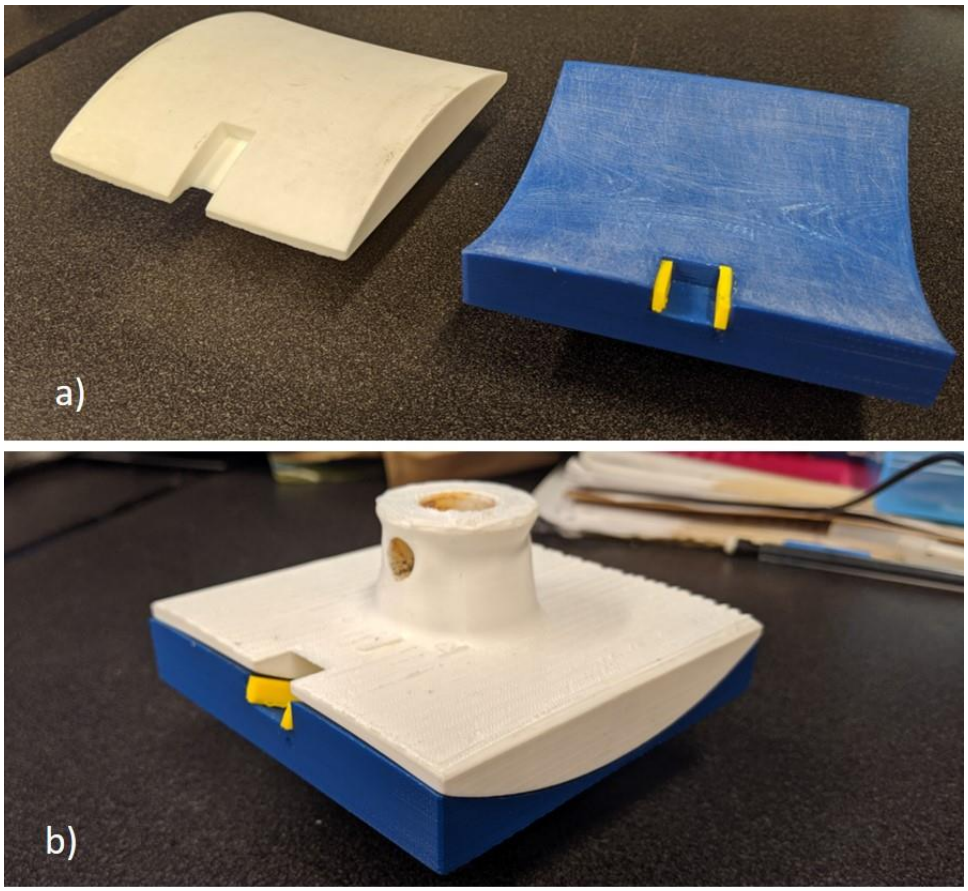

Figure 51 - The two parts of saddle-like shape bending fixture are 3D printed separately as seen in a), and they can be clamped together during the test as seen in b).

Sample P3 is tested in the saddle-like biaxial bending test. At the start of the biaxial bending experiment, S_{11} of the antenna is measured in the flat configuration. The sample is placed between the two blocks with flat mating surfaces as shown in Figure 52. The two blocks are 3D-printed using PLA with a thickness of 15 mm, and this thickness roughly corresponds to the average thickness of each of the saddle fixtures to account for the potential effect on the electrical characteristics of the antenna being sandwiched by another material. After the measurements in flat fixtures, the antenna sample is placed in between the saddle-like fixtures with the silver ink layer facing downward. The two fixtures are clamped together as demonstrated in Figure 53. In such scenario, the antenna experiences

tensile bending along the feedline line direction with a bending radius of 4 in. and a compressive bending in the direction perpendicular to the feedline with a bending radius of 40 in. After measuring S_{11} while the antenna being sandwiched by the fixtures, S_{11} is measured again in the flat configuration.

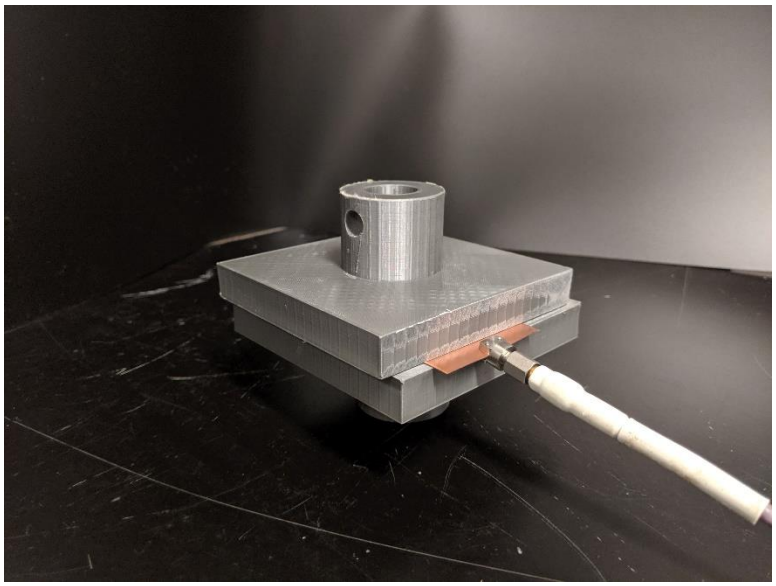

Figure 52 - The antenna is seated between two PLA printed blocks for the flat measurement.

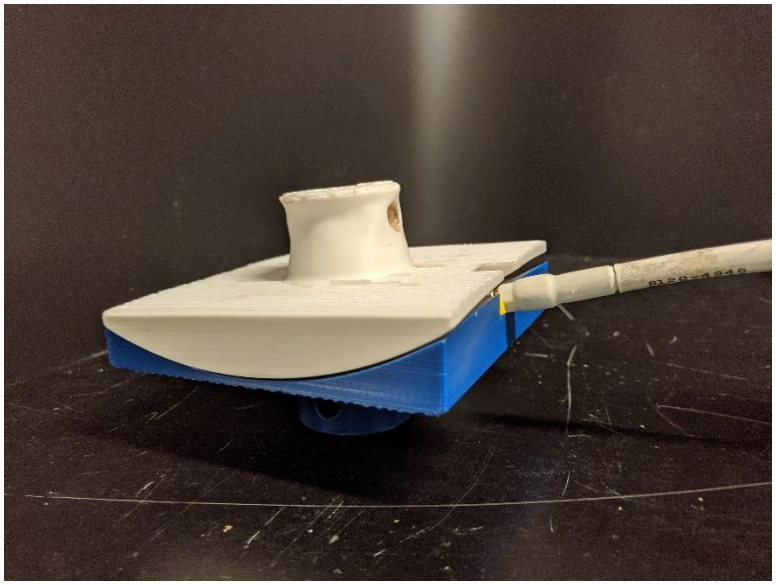

Figure 53 - The antenna is seated in between the PLA printed fixture with the ink layer facing down when taking the bent measurement.

Limited change appears in the three measurements of the S_{11} response, which is discussed more in detailed in the next section. Then the sample P3 is subjected to the cyclic biaxial bending test. The fixtures are attached to the universal testing machine; the bottom fixture remains stationary, while the top fixture moves vertically. The antenna sample P3 is placed in between the fixtures with the ink structure facing towards the bottom fixture. Figure 54 shows the setup of the cyclic experiment. A cycle starts at the position that the two fixtures are 10 mm apart. Then the top fixture travels down until the two fixtures clamp the antenna sample to fully conform to the mating surfaces. The fixtures stay at the sandwich position for two seconds before to the top fixture travel back to the initial position. In total 2000 cycles are run. The antenna sample is taken out to take S_{11} measurement at flat every 100 times below the 500^{th} cycle, and every 500 times between the 500^{th} – 2000^{th} cycles.

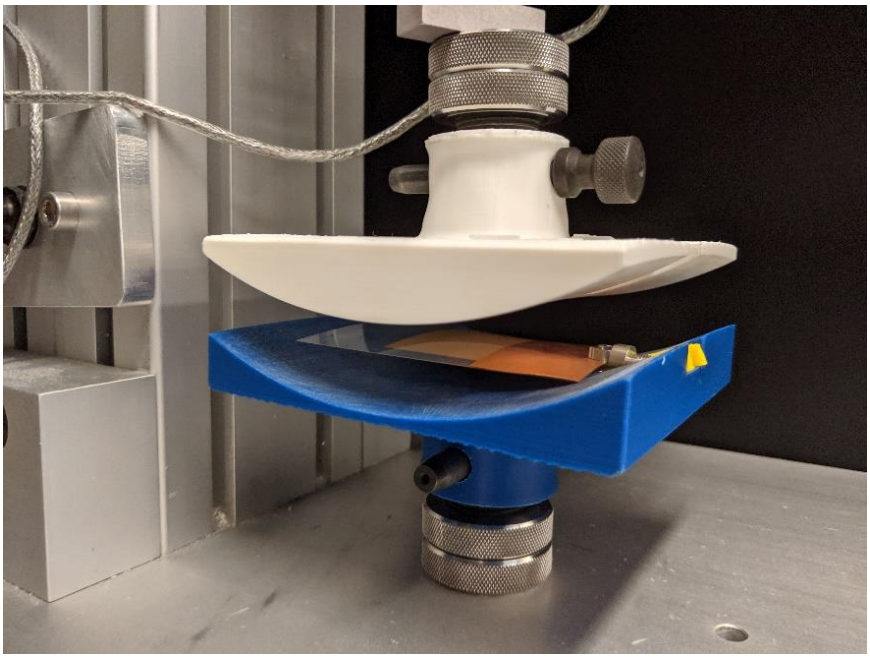

Figure 54 - The saddle-like bending fixtures are attached to universal testing machine for the cyclic bending test.

7.2 Experimental High-Frequency Measurement Results

Figure 55 shows the first cycle's measurement S_{11} results: "f0" is the initial flat measurement, "b" is the measurement taken at bent, and "ff" is the flat measurement taken after being bent. As seen, the shapes of the S_{11} responses remain the same. When the antenna is conformed to the biaxial curved mating surface, the resonant frequency is shifted by +20 MHz. In addition, the two flat measurements almost overlap with each other. This indicates that as the bending radii relatively are large, and the antenna is only subjected to one cycle of the bending there is no damage in the ink structure due to the bending.

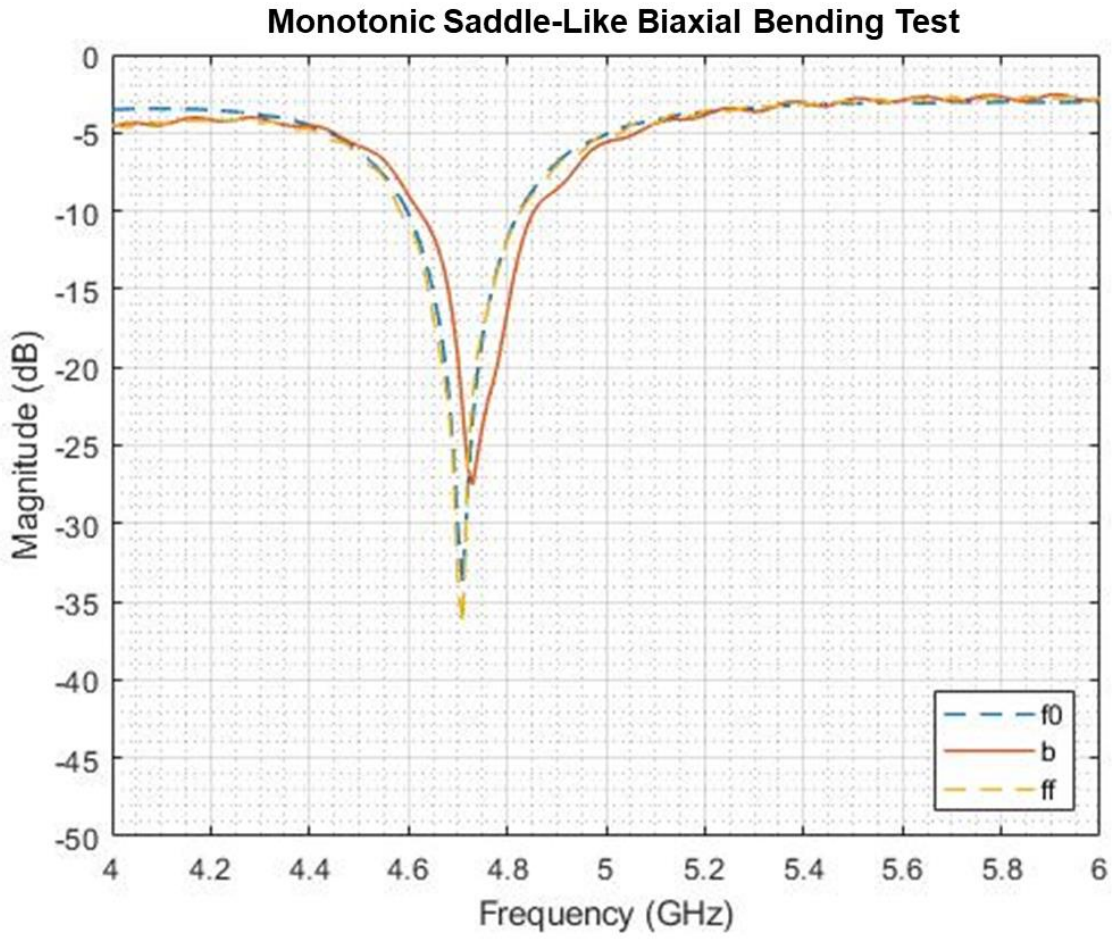

Figure 55 - The first cycle S_{11} response measurements of antenna sample P3 in the biaxial saddle-like bending test.

Figure 56 shows the flat measurement results that are taken during the cyclic biaxial bending test. “F”s indicate that they are measurement taken at flat, and the following numbers indicate the number of cycle. As seen, the resonant frequencies of all the plots fall into the range of 4.68 - 4.75 GHz, with the initial resonant frequency of 4.71 GHz. The flat measurement taken at the 2000th cycle not only has the most shift of -30 MHz, but also has a change in magnitude of its resonant frequency from around -35 dB to -19 dB.

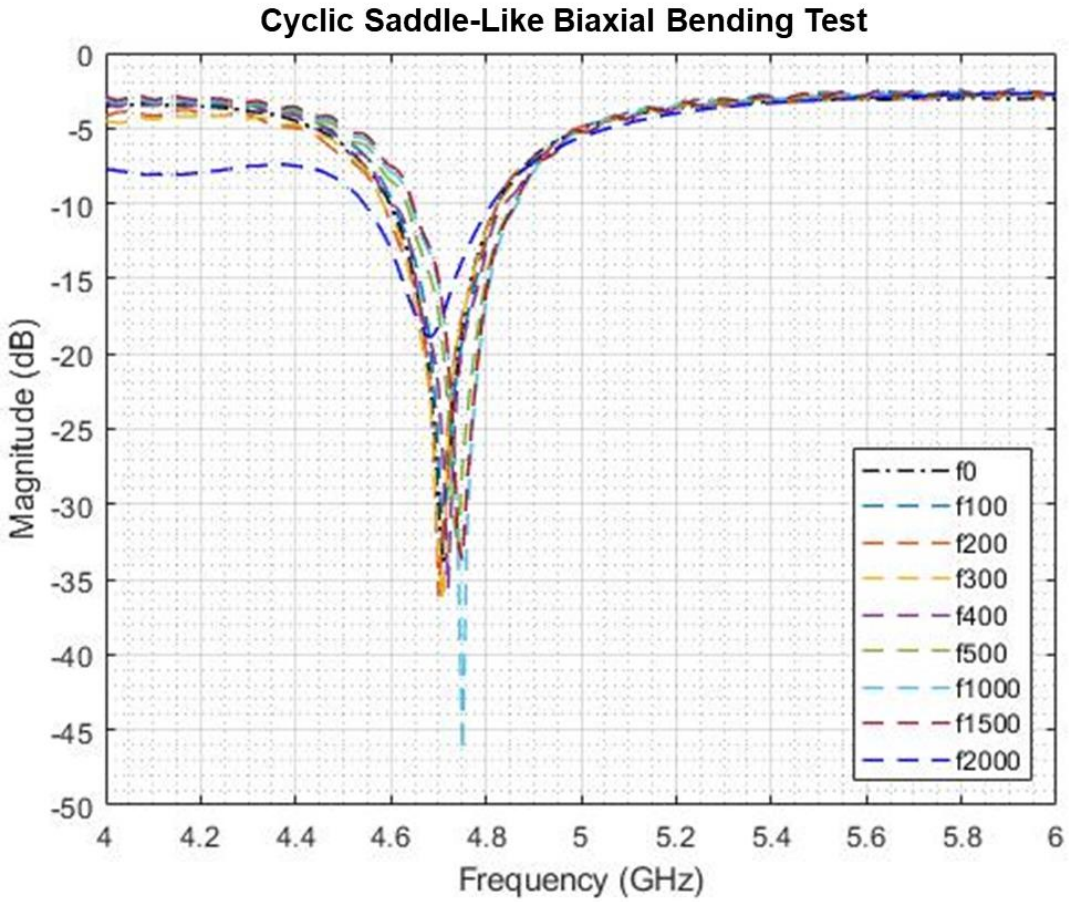

Figure 56 - S_{11} response flat measurements of antenna sample P3 in the cyclic biaxial saddle-like bending test.

7.3 SEM Images Results

SEM images are taken to examine the damages in the printed ink structure. There are no obvious cracks observed throughout the ink layer both in the feedline and the patch area. Instead, some surface scratches appear near the edge of the ground plane as seen in Figure 57 and Figure 58. Although there is no disconnection of the ink layer due to the scratches, the changes of connection mode of the silver particles can be seen in the images taken at 45k magnification. The scratches are possibly the surface damages done by the fixtures, since the antenna sample might not hold still during the clamping process. Therefore, as a biaxial bending test method, a non-invasive method such as the Bladder Inflation Stretch (BIS) test is more recommended for the sample without a protective layer.

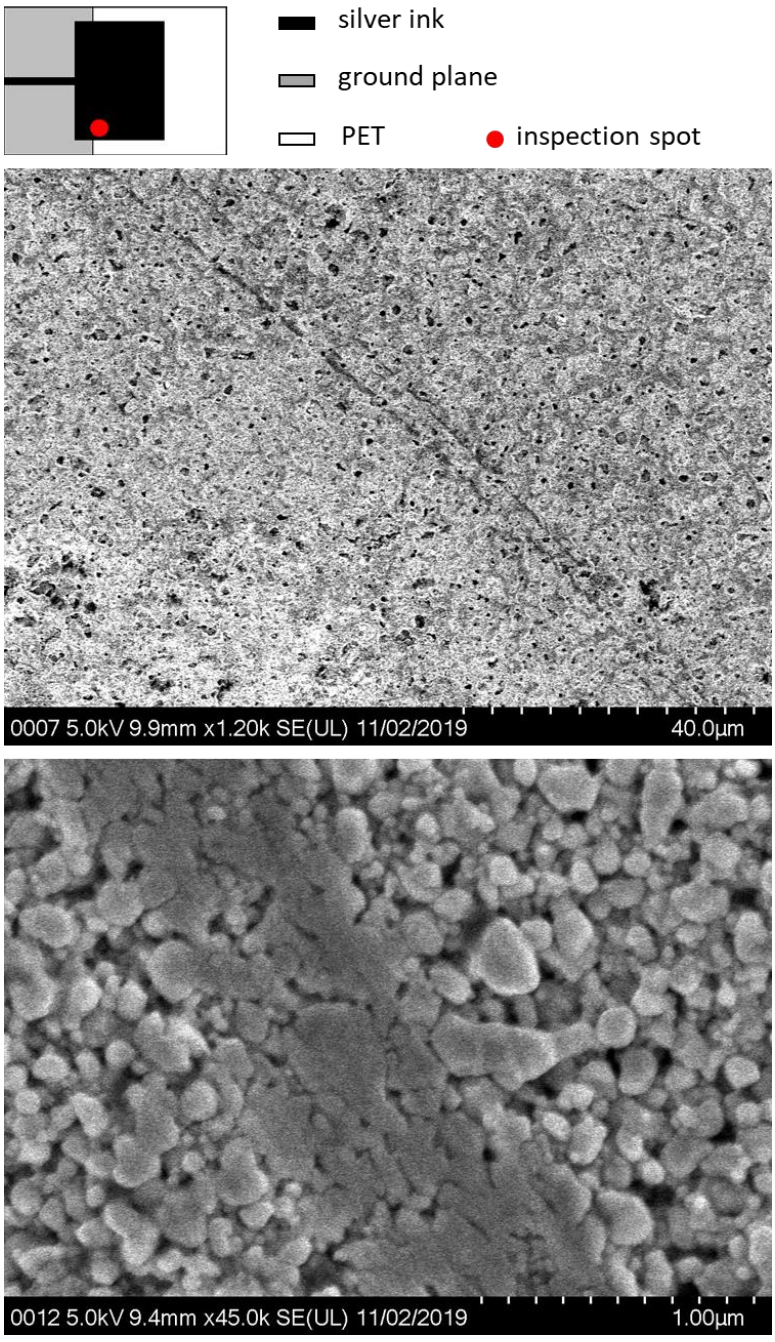

Figure 57 - SEM image of the antenna sample P3 after subjected to 2000 cycles of biaxial saddle-like shape bending test. The inspection location is near the right edge of the ground plane.

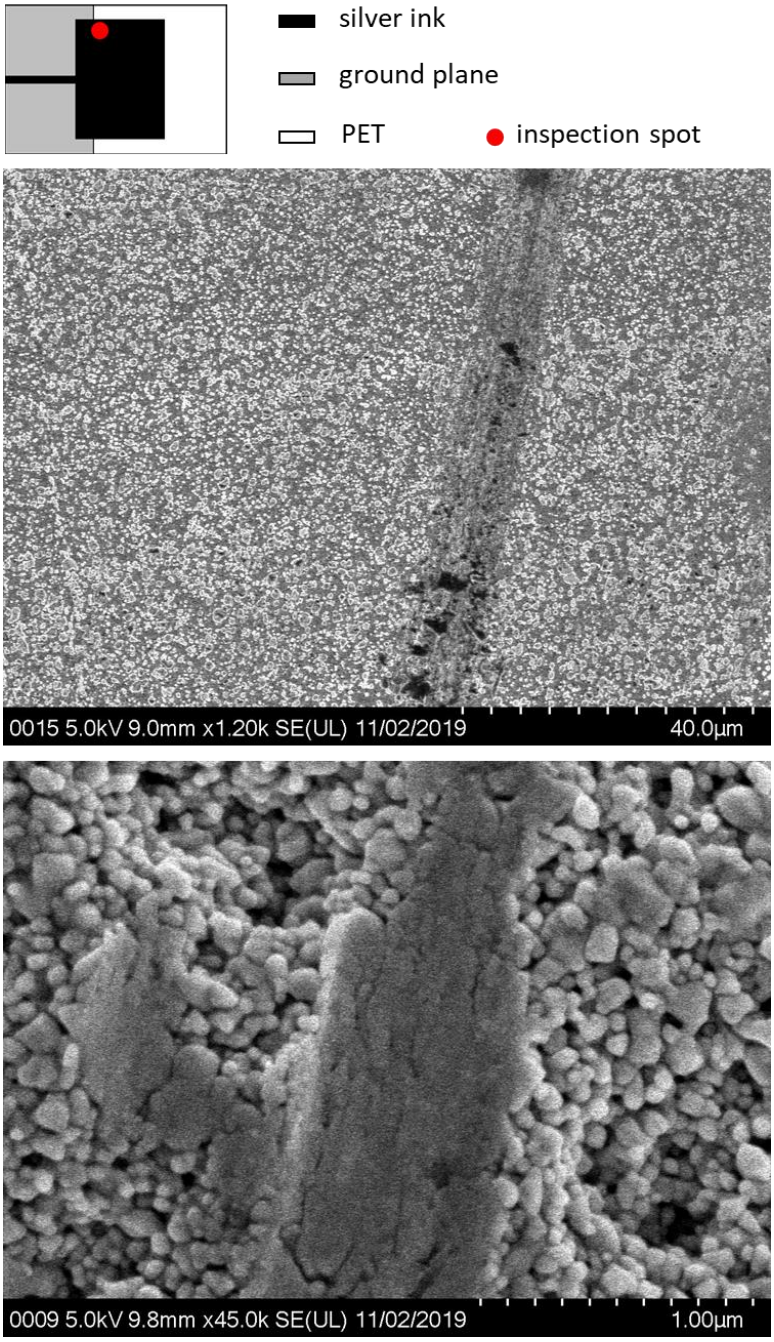

Figure 58 - SEM image of the antenna sample P3 after subjected to 2000 cycles of biaxial saddle-like shape bending test. The inspection location is near the left edge of the ground plane.

CHAPTER 8. MECHANICAL FINITE-ELEMENT ANALYSIS OF THE BIAXIAL BENDING TEST

A mechanical 3D finite-element model is built in ANSYS™ Workbench to determine the strain distribution of the antenna when in deformation in the biaxial saddle bending test. The model of the FEA simulation is shown in Figure 59. The simulation model includes the multi-layered antenna and the fixtures. The antenna model is the same in geometry, material properties as the model for the mandrel bending test which is discussed in Chapter 6. The fixtures' geometry details are discussed earlier in Chapter 7. As seen in Figure 59, the geometry models are divided for better alignment at the initial position. Similar to the mandrel bending model, the fixtures are assigned a very large elastic modulus to indicate their rigid nature in the simulation. This chapter discusses the boundary conditions and the loading details, and presents the FEA strain distribution results.

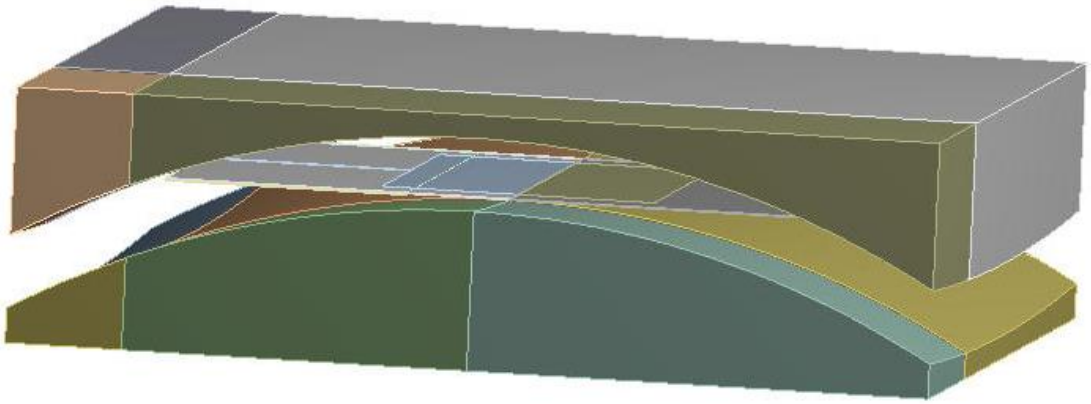

Figure 59 - Isometric view of the antenna-fixture system for biaxial bending model.

8.1 Loading and Boundary Conditions

Figure 60 shows the front view of the initial position of the model, where the antenna sample is seated between the simplified saddle fixtures, and the top and bottom fixtures are apart from each other. Upward displacement of 0.05 mm per step is applied to the bottom fixture, while the top fixture is held rigid. In addition to that, to prevent rigid body movement of the antenna, the node where the antenna sample is in contact with the top fixture is fixed, and the front surface of the antenna is constrained to have in-plane motion. The contact surfaces between the antenna and the fixtures are assigned to be frictionless. A total of 7.6 mm displacement is applied to the bottom fixture for the sample to fully conform into the curved surface as shown in Figure 61. Figure 62 shows the shape of the antenna at the final position.

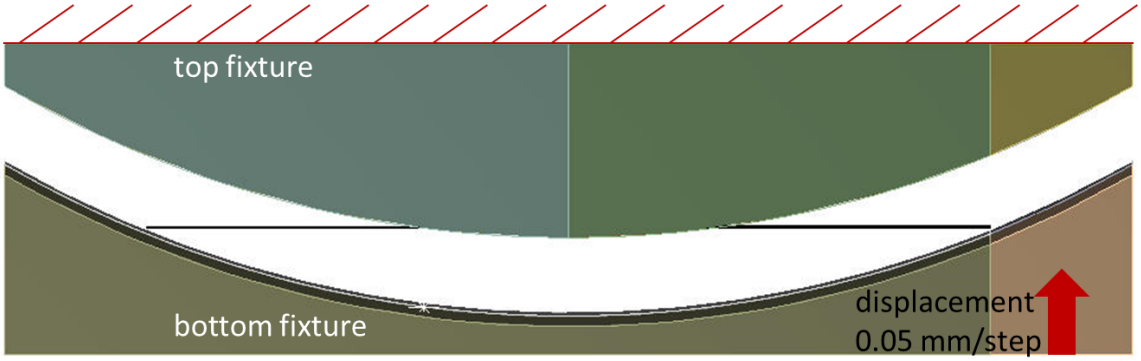

Figure 60 - Front view of the initial position of the biaxial bending model, with the indication of boundary and loading conditions.

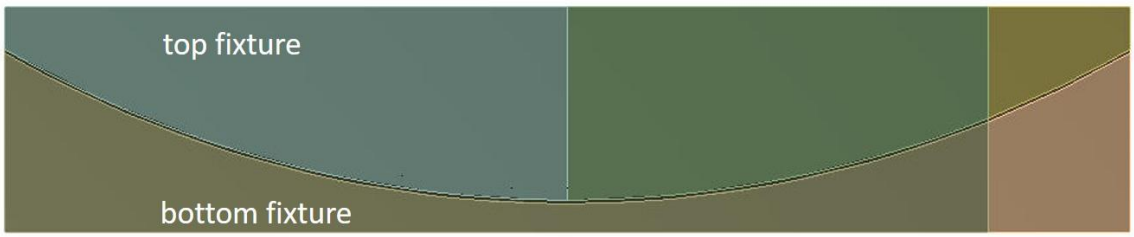

Figure 61 - Front view of the final position of the biaxial bending model.

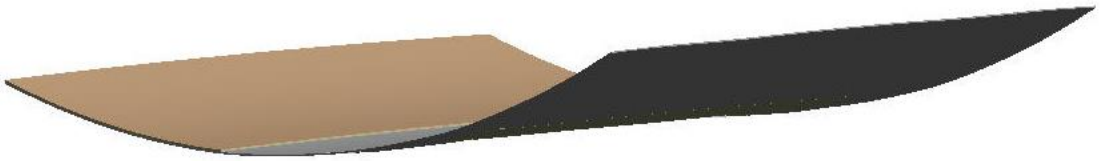

Figure 62 - Isometric view of the antenna sample at the final position.

8.2 Mesh Convergence and Simulation Results

Theoretically, the strain induced by the biaxial deformation can be calculated by Equations 6 and 7. The *x* direction represents the lengthwise direction and *y* represents the width direction.

$$\varepsilon_{xx} = \frac{d}{\rho_x} - \nu\frac{d}{\rho_y} \tag{6}$$

$$\varepsilon_{yy} = \frac{d}{\rho_y} - \nu\frac{d}{\rho_x} \tag{7}$$

where ε_{xx} and ε_{yy} are the strain values in *x* direction and *y* direction , *d* is the distance from the neutral axis of the multilayer structure, ρ_x is the bending radius along *x* direction of 4 inches, ρ_y is the bending radius along *y* direction of 40 inches, and *v* is the Poisson's ratio of the silver ink structure. The strain values of the printed ink structure differ in different zones. In the zone with the underneath copper ground plane, ε_{xx} is calculated to be 0.00237, and ε_{yy} is calculated to be -0.00067. In the zone without the underneath copper ground

plane, ε_{xx} is calculated to be 0.00064, and ε_{yy} is calculated to be -0.000179. A summary of the theoretical values is presented in Table 5.

Table 5 - Theoretical strain values of the printed ink sturcture under the biaxial bending condition.

Ink Structure of Different Zone	ε_{xx}	ε_{yy}
Zone with Underneath Ground Plane	0.00237	-0.00067
Zone without Underneath Ground Plane	0.00064	-0.00018

Figure 63 and Figure 64 show the initial mesh (case 1) details of the fixtures and the multi-layered antenna. Similar to the model of the mandrel bending test, the fixtures are assumed as rigid bodies in the simulation and are meshed with 8-node SURF 154 elements. The element size is assigned to be 5 mm.

The multi-layered antenna is meshed with the 20-node SOLID 186 elements. The element size of 1 mm is assigned to the top surface of the silver ink layer. A sweep method is used for the ink layer with two layers through thickness initially. A multizone method is used in the PET layer, adhesive layer and copper layer to help saving elements in the unfocused area as seen. A sweep method is also used in these three layers. The PET is meshed with 2 layers, adhesive with 1 layer, and the ground plane with 2 layers through thickness.

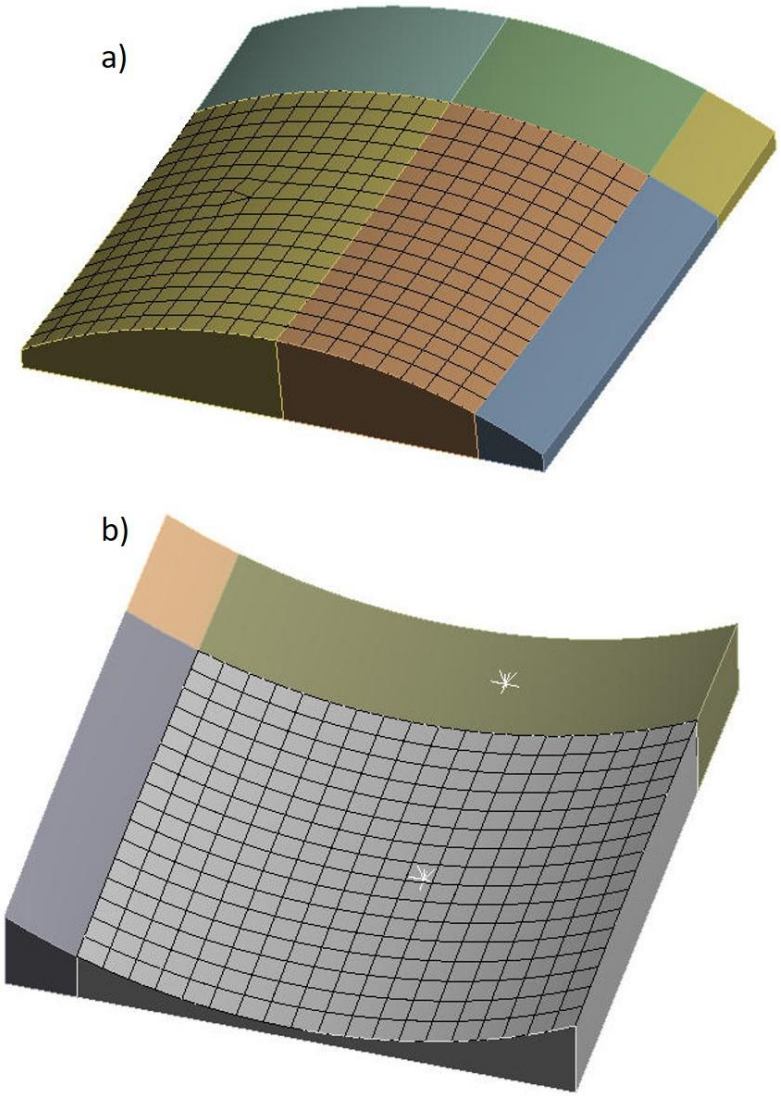

Figure 63 - Isometric view of the a) top fixture, and b) bottom fixture with indication of initial mesh details.

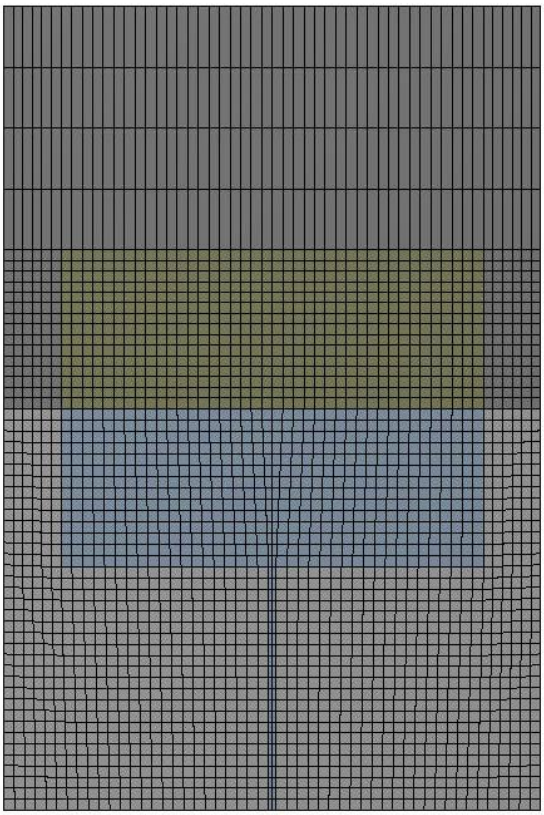

Figure 64 - Top view of the multi-layered patch antenna with the initial mesh details.

Figure 65 shows the direction of the principal strains from the simulation. As seen, the first principal and the second principal strains are the two in-plane strains of the printed ink structure. Therefore, these two contours are plotted to compare with the theoretical values.

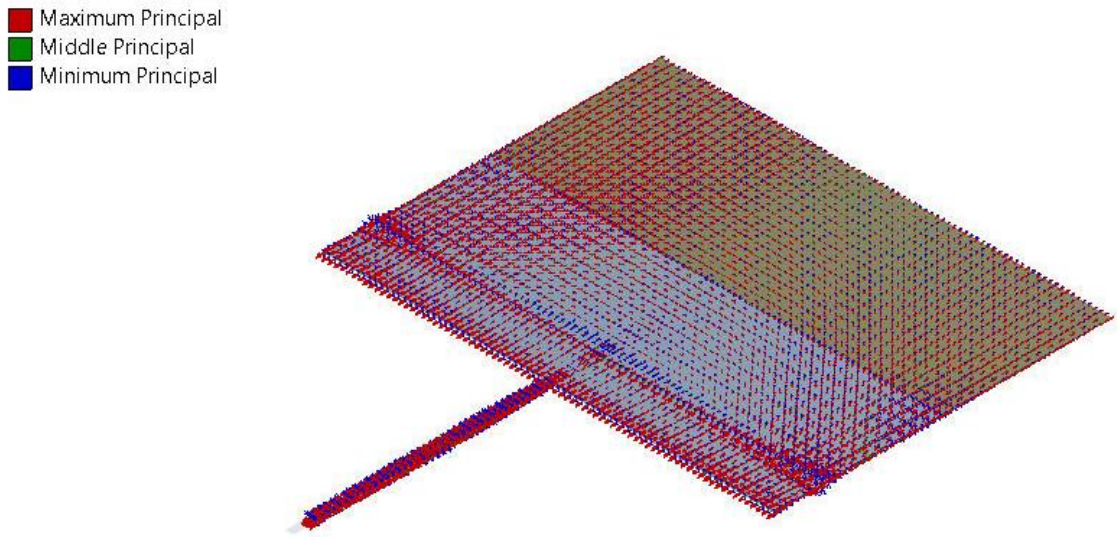

Figure 65 - Simulation result of the principal strain vector contour with the initial mesh.

Figure 66 is the first principal strain contours. As seen, in the zone with underneath ground plane, the first principal strain is in the range of 0.00249 – 0.00326. This value is close to the theoretical ε_{xx} value of 0.00237. The first principal strain of the printed ink structure without underneath ground plane is in the range of 0.00056 – 0.00095, which is closed to the theoretical ε_{yy} value of 0.00064. The edge effect appears due to the copper ground plane, and the strain concentration occurs at the edge with a strain value of 0.00364.

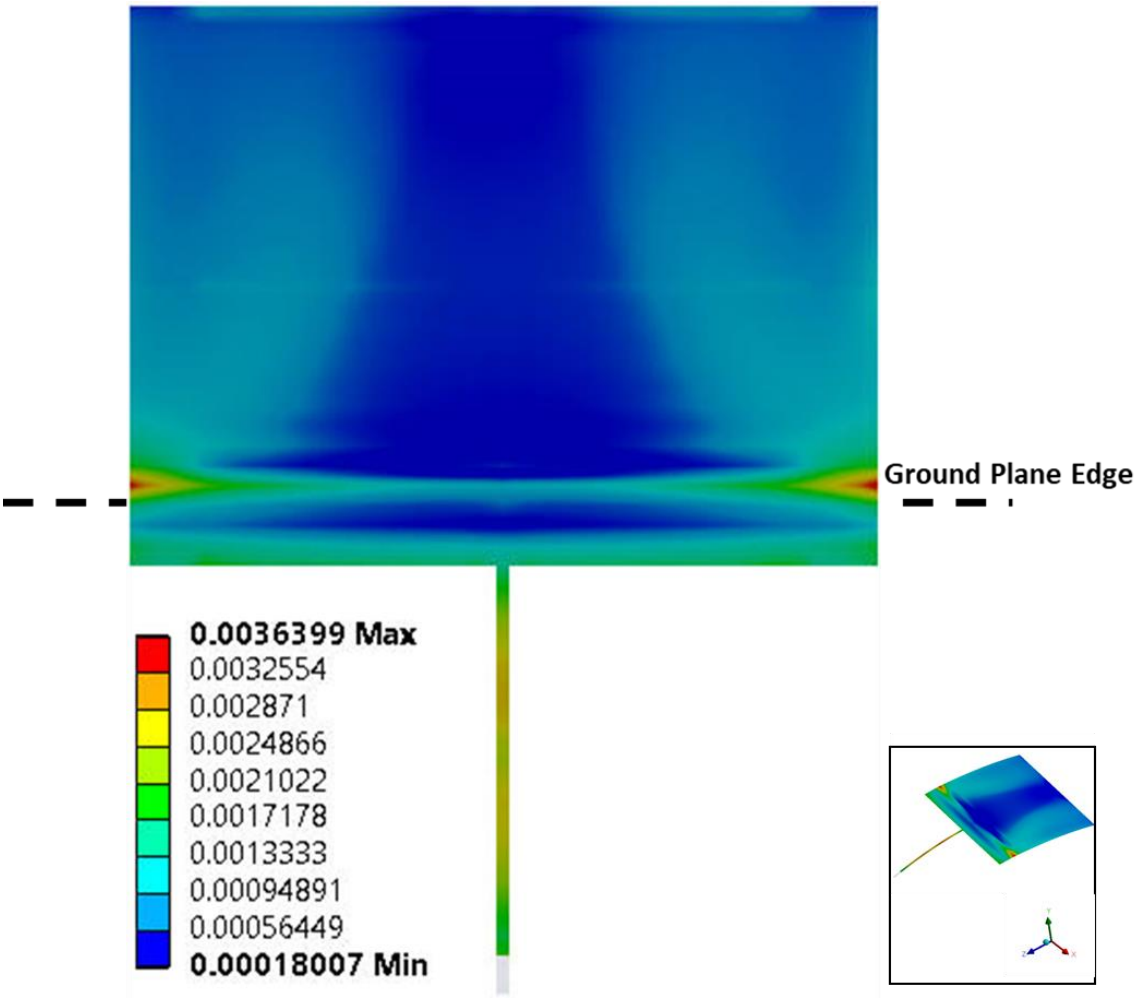

Figure 66 - Simulation result of the first principal strain distribution of the ink layer in the saddle-like shape bending model with the initial mesh (case 1).

Figure 67 is the second principal strain contours. As seen, in the zone with underneath ground plane, the second principal strain is in the range of -0.00079 – -0.00038. This value range is close to the theoretical ε_{xx} value of -0.00067. The second principal strain of the printed ink structure without underneath ground plane is in the range of -0.00025 – 0.00030, which is close to the theoretical ε_{yy} value of -0.00018. It is noted that a strain concentration appears where the patch is divided. Therefore, another run of the simulation is conducted with a finer mesh.

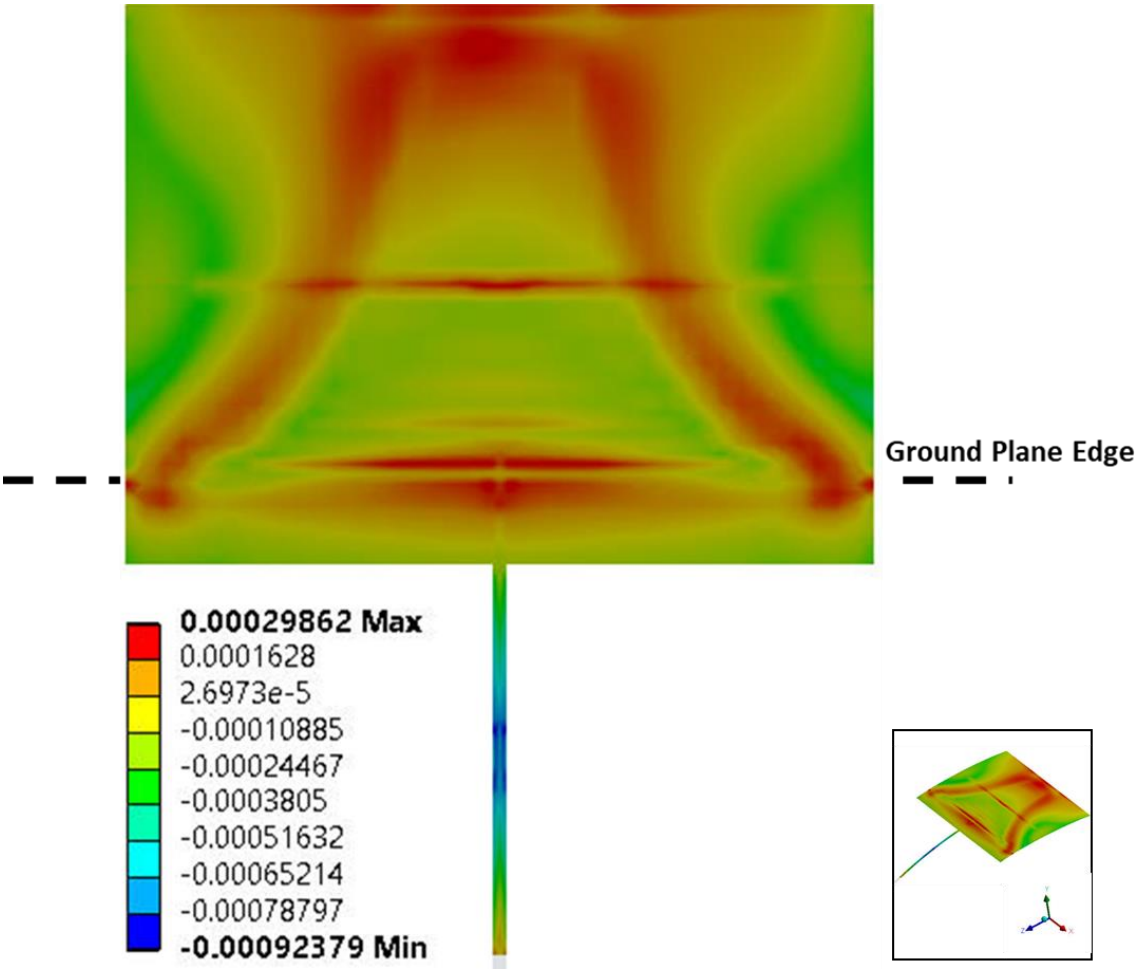

Figure 67 - Simulation result of the second principal strain distribution of the ink layer in the saddle-like shape bending model with the initial mesh (case 1).

In the mesh case 2, 0.5 mm is assigned to patch edge, and 3 mm to the fixtures' surfaces as the element sizes. Figure 68 and Figure 69 show the first and second principal strain contours of the case 2 results. As seen, the strain results of the mesh case 2 have similar contours to the ones of mesh case 1. In addition, the strain contours of mesh case 2 are smoother and do not have strain concentration. A summary of the strain results in both cases is presented in Table 6. As seen, in the mesh case 2 with finer mesh, all the strain values are smaller and closer to the theoretical values. In general, the FEA strain results of the printed ink structure are fairly small in the biaxial bending condition due to the large bending radii.

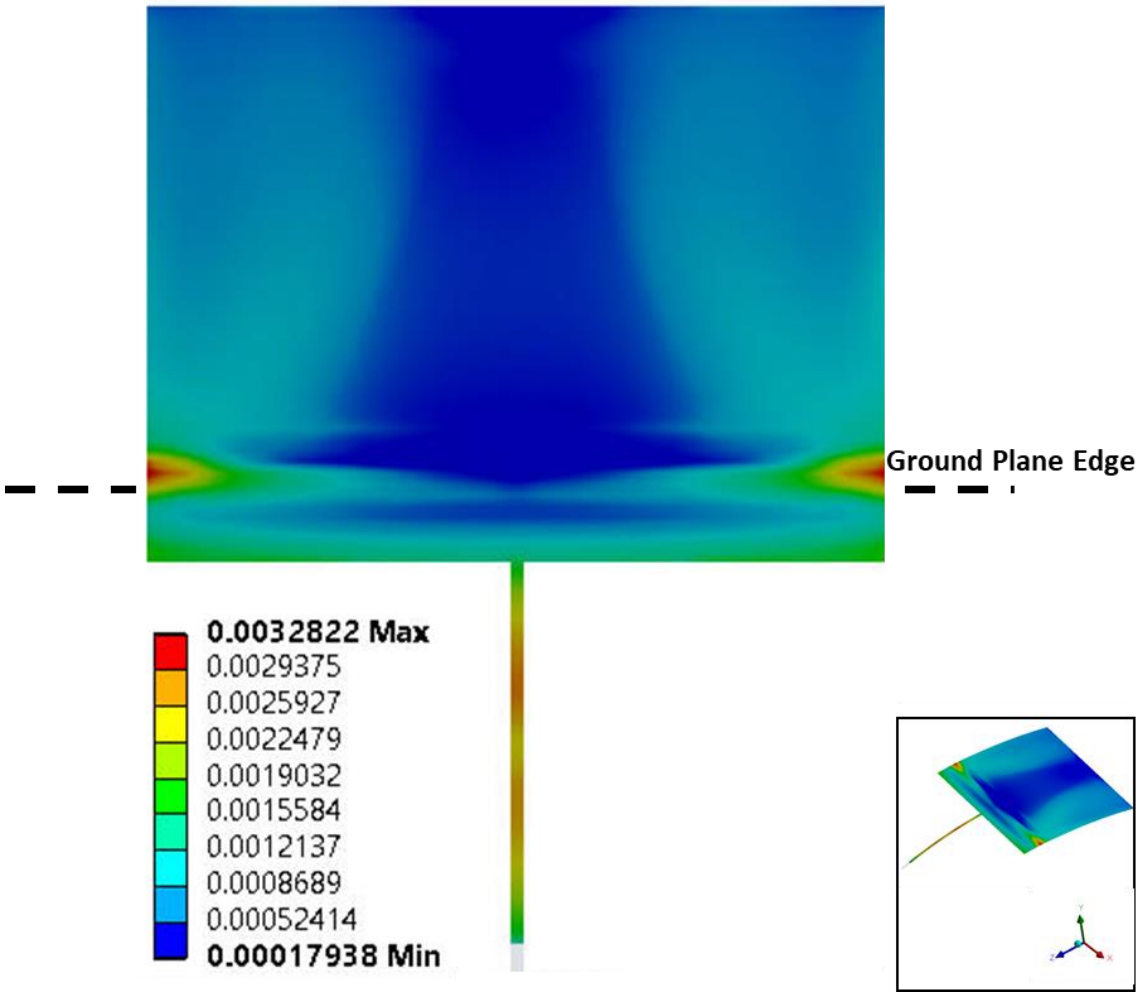

Figure 68 - Simulation result of the first principal strain distribution of the ink layer in the saddle-like shape bending model with the mesh case 2.

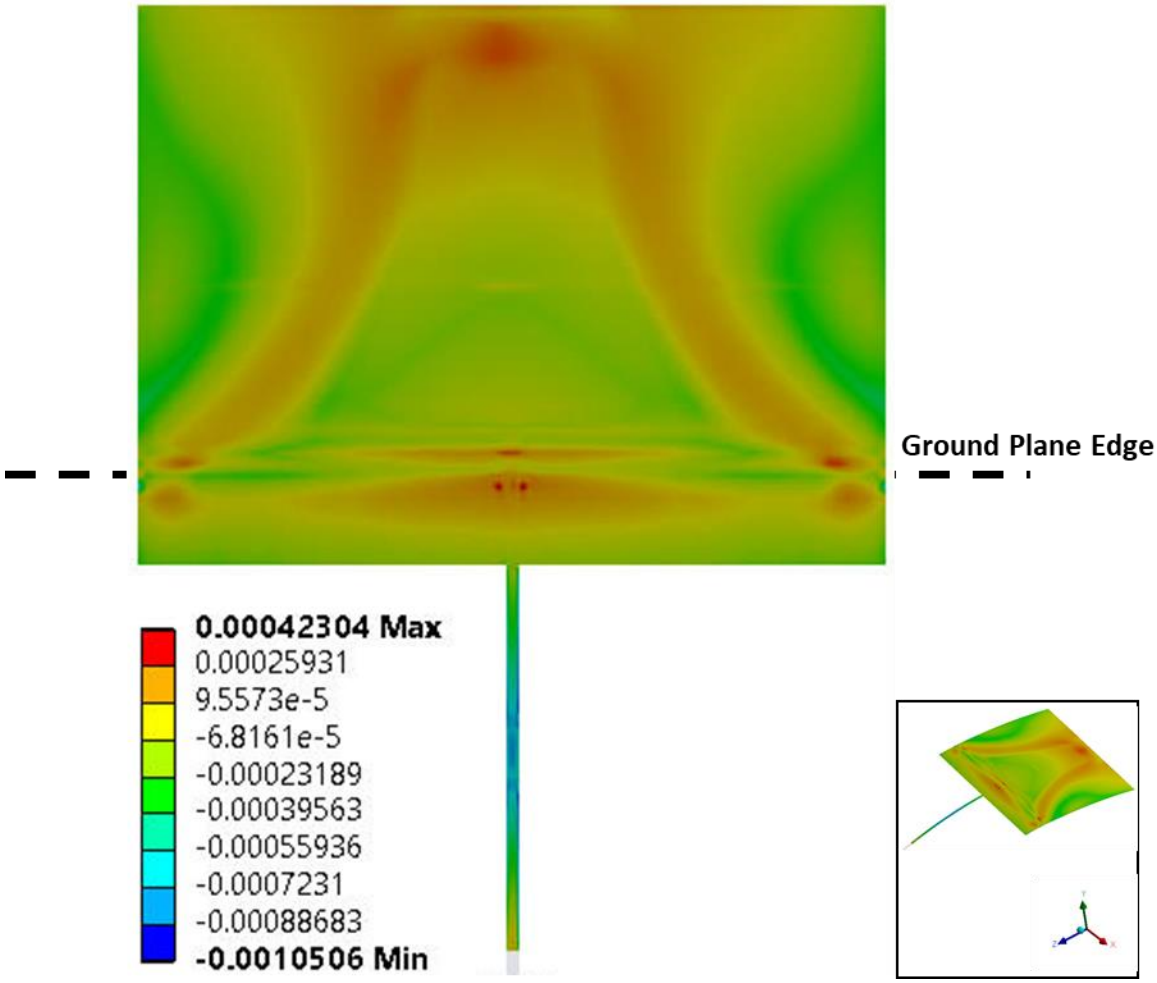

Figure 69 - Simulation result of the second principal strain distribution of the ink layer in the saddle-like shape bending model with the mesh case 2.

Table 6 - Mesh convergence results of the saddle-like shape bending model.

Case	1	2	Theoretical Value
Antenna Patch Edge Element Size	1 mm	0.5 mm	
Fixtures Mating Surface Element Size	5 mm	3 mm	
First Principal Strain Range with Ground Plane	0.00249 – 0.00326	0.00225 – 0.00294	0.00237
First Principal Strain Range without Ground Plane	0.00056 – 0.00095	0.00052 – 0.00087	0.00064
Max First Principal Strain	0.00364	0.00328	
Second Principal Strain Range with Ground Plane	-0.00079 – -0.00038	-0.00089 – -0.00040	-0.00067
Second Principal Strain Range without Ground Plane	-0.00025 – 0.00030	-0.00023 – 0.00026	-0.00018

CHAPTER 9. CONDUCTIVITY CHANGE IMPACT ON PATCH ANTENNA'S HIGH-FREQUENCY ELECTRICAL BEHAVIOR

Although the damages are observed in the ink structures after 2000 cycles of bending in both the biaxial and uniaxial bending tests, the shifts in resonant frequency response of the antenna are less than 50 MHz in the flat configuration. The relationship between the conductivity and the S_{11} response are studied with the electrical model in HFSS.

9.1 Updated HFSS Model

An updated model is built in HFSS to better match the fabricated sample and the measurement results. The updated model is built based on the dimensions of the antenna sample P1, and a polycarbonate sheet is placed underneath the antenna model as seen in Figure 70. The updated patch size is 30.69 mm × 40.69 mm, and the polycarbonate sheet is 0.125 in. thickness. The polycarbonate sheet has the dielectric constant of 2.8, and the loss tangent of 0.01 [67]. Figure 71 provides the comparison between the initial flat measurement taken of P1 at the flat configuration and the simulation result of the updated model. The simulation result has the resonant frequency of 4.79 GHz, and the actual measurement has the resonant frequency of 4.81 GHz.

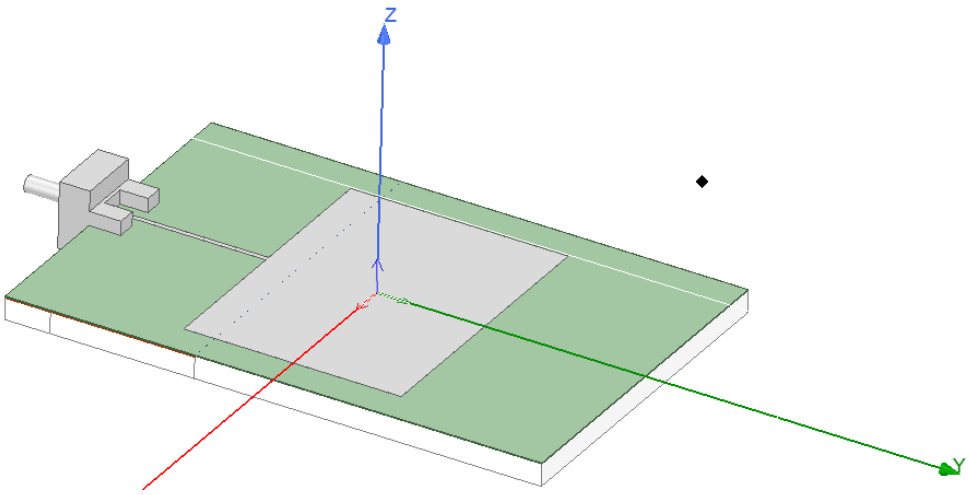

Figure 70 - Updated HFSS model built based on the geometry of sample P1 with polycarbonate sheet underneath.

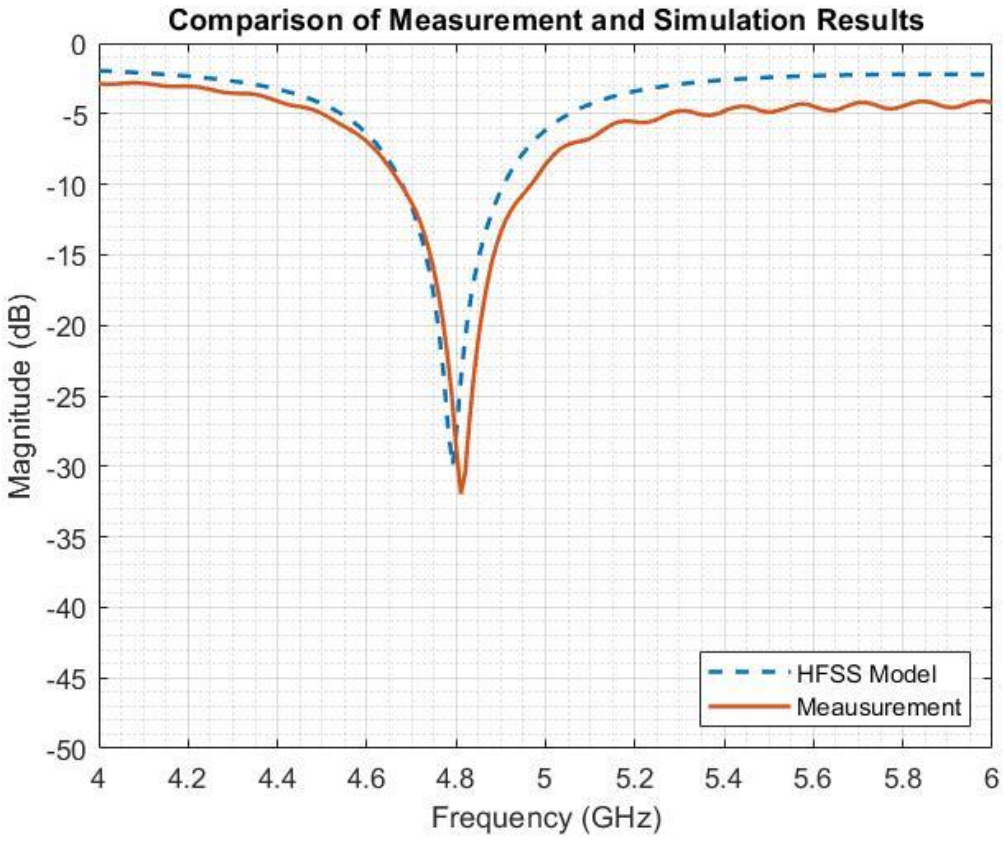

Figure 71 - Comparison of the HFSS simulation and measurement results of P1 at flat configuration.

9.2 Conductivity Impact on the S_{11} Response

Multiple sweeps are run with different values of the conductivity to examine how sensitive is the S_{11} responses to the conductivity change. The original model has a conductivity of 2.52×10^6 S/m. The tested conductivity range is 0.50×10^6 S/m – 3.00×10^6 S/m. The results of the sweeps plus the initial model is presented in Figure 72(a).

It is seen that the value of resonant frequency has limited change due to the variation in conductivity. Larger changes are however observed in the magnitude. When the conductivity is reduced to 1.00×10^6 S/m, the magnitude of the resonant frequency changes from -30 dB to -20 dB, and when the conductivity is further reduced to 0.5×10^6 S/m, the S_{11} loses the sharpness at resonance. This matches with experimental results. The minimum conductivity measured on sample P1 after it is bent is 1.13×10^6 S/m, 45% of the initial value. As seen in Figure 72(b), the final measurement taken after 2000 cycles of bending has similar resonant frequency as the initial flat measurement; but the magnitude in the final measurement is about -25 dB and the initial one is about -30 dB.

The decrease in conductivity of the printed structure is due to the cracks accumulated through cycles of deformation. For the antenna structure with a lower conductivity at around 1.00×10^6 S/m, at the resonant frequency, impedance matching is getting affected due to increased loss in the antenna. This is manifesting itself as an increase in the magnitude of return loss at resonance. It is expected that as a result, the radiated antenna gain will decrease when the antenna is bent over 2000 cycles.

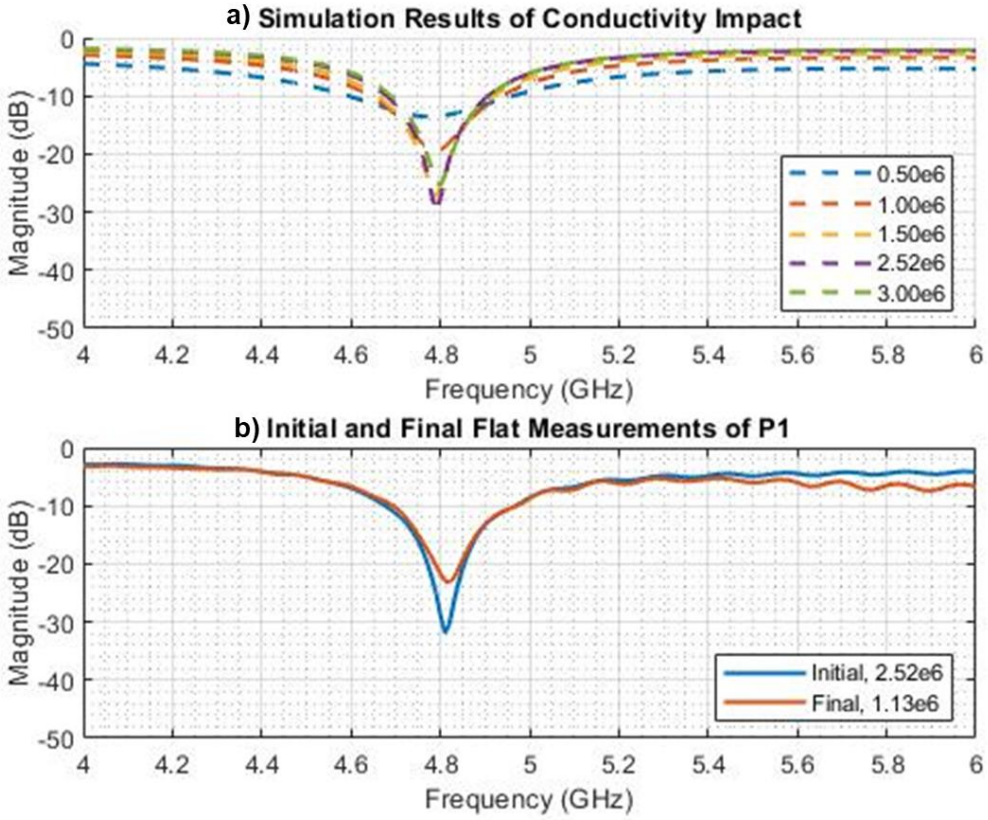

Figure 72 - Conductivity value has impact on the S_{11} response. a) HFSS simulation results of models with different conductivity values. b) The initial and final flat measurements of P1 in mandrel bending test.

Among all the experimental results, the most shift of resonant frequency at bent is -80 MHz (-1.66% of shift relative to 4.81 GHz) when the antenna is wrapped around the smallest mandrel of 0.625 in. radius. A greater shift of the resonant frequency at bent configuration, can be due to the elongation of the electrical length [68]. For a patch antenna on Kapton™, 0.5% of maximum relative shift to lower values is observed when a uniform 0.5% bending strain is experienced by the antenna. In this work, when the antenna is bent over the mandrel of 0.625 in. radius, the strain value over the antenna patch is between 0.95% and 1.79%.

CHAPTER 10. CONCLUSION, CONTRIBUTIONS, AND FUTURE WORK

10.1 Conclusion

This work has designed and fabricated flexible patch antennas by inkjet printing method. High-frequency electrical performance of the antennas is characterized and measured in and after different bending conditions. The damages in the printed ink structure due to cycles of deformation have been inspected by SEM. Mechanical finite-element models have been developed to mimic the bending experiments and to compare with the damage observed in SEM. Electrical models have been built to relate damage that appears in the ink to the electrical performance of the patch antenna, and to compare against the experimental results.

The patch antenna is designed to have a patch size of 30 mm × 40 mm with a target resonant frequency of 5 GHz. Three antenna samples are printed by the Epson™ C88+ inkjet printer with Novacentrix™ JS-B25P silver nanoparticle ink on PET substrates. The three samples have resonant frequencies of 4.82 GHz, 5.06 GHz, and 4.93 GHz in free space. The conductivity of the printed ink is 2.52×10^6 S/m.

In uniaxial cyclic bending test over various sizes of mandrel, when the antenna sample is wrapped around cylindrical mandrels, a decrease in resonant frequency is observed at the smaller mandrel size, and the resonant frequency continues to decrease with repeated cycling, especially at smaller radii. The resonant frequency measurements at the flat configuration after each bent have limited changes compared to the initial results. The

antenna samples are also tested in cyclic mandrel bending test over the cylinder mandrel of 0.625 in. in radius up to 2000 cycles. A maximum 50 MHz shift to a lower value in resonant frequency is observed at flat configuration. SEM images are taken to the samples after 2000 cycles, and the cracks are observed throughout the printed ink structure. But the crack density varies in different zones, depending on whether there is a copper ground plane underneath. The crack that appears in the printed ink structure leads to a decrease in the conductivity.

There is less than 2% relative change on the electrical performance of the antenna when being conformed to the designated biaxial curved surface. A maximum 70 MHz shift to a lower value in resonant frequency is observed after 2000 cycles of bending in biaxial bending test at flat configuration. From the inspection results of the SEM images, no cracks are observed, but some surface scratches due to the clamping motion of the surface are seen, which change the particle connection modes.

Mechanical finite-element models are built to mimic the both mandrel and saddle-like shape bending tests. The ink's elastic modulus is obtained in-house by nanoindentation, while other materials' properties are obtained from literatures. A maximum strain of 0.01740 is seen in uniaxial bending model, and a maximum strain of 0.00364 is seen in biaxial bending model. The location of the maximum strain values matches with the damage spots found in SEM images.

The damages in the ink structure leads to the decrease of the conductivity of the printed ink. The minimum conductivity measured from the printed ink structure after bending is 1.13×10^6 S/m, which is 45% of the initial value. From the electrical simulations done in HFSS, for this specific design, if the final conductivity is greater than 40% of the

original conductivity value, the S_{11} response does not show a great change in the shape and resonant frequency. This matches with the observation from the bending experiments.

10.2 Contributions

This thesis has successfully fabricated patch antennas by inkjet printing that match with the design expectation. The antenna samples are tested in uniaxial and biaxial bending test. The contributions of this work are:

- The design and fabrication methodologies of inkjet-printed flexible patch antenna that works in high-frequency have been successfully demonstrated.
- Antenna performance has been measured under both bending configuration and flat configuration. The bending tests have been carried out both uniaxially and biaxially. This provides an insight of how the antenna would behave in a realistic application and gives an insight into the reliability of the antenna.
- The failure locations of the printed ink structures can be predicted from the mechanical numerical simulations of the antenna under deformation.
- The impact of the decrease in conductivity due to ink damages from deformation on the electrical performance have been studied for the patch antenna by electrical numerical simulation.

10.3 Future Work

There are various areas of this research that could be further explored, including:

- In this work, only S_{11} is characterized and studied for the antenna design. Other parameters such as radiation patterns should also be studied when in deformation.

- For the biaxial bending test, the damages are done to the printed ink structure from the performance of the fixture. The flexible antenna needs to be tested in other non-invasive method such as Bladder Inflation Test to avoid the unwanted damages.
- This work only studies one design of the rectangular patch antenna. More designs of the patch antenna and other types of antenna, such as spiral and dipole antenna designs, need to be examined.
- The mechanical finite-element models need to be extended to account for non-linear constitutive behavior of the substrate and the printed materials.

REFERENCES

[1] M. Segev-Bar and H. Haick, "Flexible Sensors Based on Nanoparticles", *ACS Nano*, vol. 7, no. 10, pp. 8366-8378, 2013. Available: 10.1021/nn402728g.

[2] M. Stoppa and A. Chiolerio, "Wearable electronics and smart textiles: A critical review, " *Sensors*, vol. 14, no. 7, pp. 11957–11992, 2014.

[3] J. van den Brand et al., "Flexible and stretchable electronics for wearable health devices", *Solid-State Electroni*cs, vol. 113, pp. 116-120, 2015.

[4] G. Yang et al., "A Health-IoT Platform Based on the Integration of Intelligent Packaging, Unobtrusive Bio-Sensor, and Intelligent Medicine Box, " in *IEEE Transactions on Industrial Informatics*, vol. 10, no. 4, pp. 2180-2191, Nov. 2014.

[5] A. Eid et al., "Nanotechnology-Empowered Flexible Printed Wireless Electronics: A Review of Various Applications of Printed Materials, " in *IEEE Nanotechnology Magazine*, vol. 13, no. 1, pp. 18-29, Feb. 2019.

[6] S. Khan, L. Lorenzelli and R. S. Dahiya, "Technologies for Printing Sensors and Electronics Over Large Flexible Substrates: A Review, " in *IEEE Sensors Journal*, vol. 15, no. 6, pp. 3164-3185, June 2015.

[7] V. Misra et al., "Flexible Technologies for Self-Powered Wearable Health and Environmental Sensing, " in *Proceedings of the IEEE*, vol. 103, no. 4, pp. 665-681, April 2015.J. Clerk Maxwell, A Treatise on Electricity and Magnetism, 3rd ed., vol. 2. Oxford: Clarendon, 1892, pp.68–73.

[8] S. Cruz, L. Rocha, and J. Viana, "Printing Technologies on Flexible Substrates for Printed Electronics. " DOI: 10.5772/intechopen.76161, July 2018.

[9] W. Wong and A. Salleo, *Flexible electronics*. pp. 7,77-78.

[10] W. MacDonald et al., "Latest advances in substrates for flexible electronics", *Journal of the Society for Information Display*, vol. 15, no. 12, p. 1075, 2007. Available: 10.1889/1.2825093.

[11] W. MacDonald et al., "Polyester Film Substrates for the Flexible Electronics Industry - An Overview and Where Next."

[12] V. Zardetto, T. Brown, A. Reale and A. Di Carlo, "Substrates for flexible electronics: A practical investigation on the electrical, film flexibility, optical, temperature, and solvent resistance properties", *Journal of Polymer Science Part B: Polymer Physics*, vol. 49, no. 9, pp. 638-648, 2011. Available: 10.1002/polb.22227.

[13] L. Tong et al., "Electrically Conductive TPU Nanofibrous Composite with High Stretchability for Flexible Strain Sensor", *Nanoscale Research Letters*, vol. 13, no. 1, 2018. Available: 10.1186/s11671-018-2499-0.

[14] J. Suikkola et al., "Screen-Printing Fabrication and Characterization of Stretchable Electronics", *Scientific Reports*, vol. 6, no. 1, 2016. Available: 10.1038/srep25784.

[15] X. Fan et al., "Synthesis of nano-copper particles for conductive ink in gravure printing," *The 8th Annual IEEE International Conference on Nano/Micro Engineered and Molecular Systems*, Suzhou, 2013, pp. 775-778.

[16] J. Reboun, J. Hlina, R. Soukup and J. Johan, "Printed thick copper films for power applications," *2018 7th Electronic System-Integration Technology Conference (ESTC)*, Dresden, 2018, pp. 1-5.

[17] J. Niittynen, E. Sowade, H. Kang, R. Baumann and M. Mäntysalo, "Comparison of laser and intense pulsed light sintering (IPL) for inkjet-printed copper nanoparticle layers", *Scientific Reports*, vol. 5, no. 1, 2015. Available: 10.1038/srep08832.

[18] S. Jang et al., "Sintering of inkjet printed copper nanoparticles for flexible electronics", *Scripta Materialia*, vol. 62, no. 5, pp. 258-261, 2010. Available: 10.1016/j.scriptamat.2009.11.011.

[19] Z. Liu, Y. Su and K. Varahramyan, "Inkjet-printed silver conductors using silver nitrate ink and their electrical contacts with conducting polymers", *Thin Solid Films*, vol. 478, no. 1-2, pp. 275-279, 2005. Available: 10.1016/j.tsf.2004.11.077.

[20] S. Kim and H. Sung, "Effect of printing parameters on gravure patterning with conductive silver ink", *Journal of Micromechanics and Microengineering*, vol. 25, no. 4, p. 045004, 2015. Available: 10.1088/0960-1317/25/4/045004.

[21] K. Kim, K. Jung and S. Jung, "Design and fabrication of screen-printed silver circuits for stretchable electronics", *Microelectronic Engineering*, vol. 120, pp. 216-220, 2014. Available: 10.1016/j.mee.2013.07.003.

[22] T. Seifert, E. Sowade, F. Roscher, M. Wiemer, T. Gessner and R. Baumann, "Additive Manufacturing Technologies Compared: Morphology of Deposits of Silver Ink Using Inkjet and Aerosol Jet Printing", *Industrial & Engineering Chemistry Research*, vol. 54, no. 2, pp. 769-779, 2015. Available: 10.1021/ie503636c.

[23] J. Chung, S. Ko, N. Bieri, C. Grigoropoulos and D. Poulikakos, "Conductor microstructures by laser curing of printed gold nanoparticle ink", *Applied Physics Letters*, vol. 84, no. 5, pp. 801-803, 2004. Available: 10.1063/1.1644907.

[24] H. Kang, G. Lee and Y. Nam, "Inkjet-printed gold nanorods using biocompatible polyelectrolyte layer-by-layer coating for patterned photothermal applications," *2017 39th Annual International Conference of the IEEE Engineering in Medicine and Biology Society (EMBC)*, Seogwipo, 2017, pp. 3545-3548.

[25] S. A. Tukur, N. A. Yusof and R. Hajian, "Gold Nanoparticles-Modified Screen-Printed Electrode for Determination of Pb(II) Ion Using Linear Sweep Anodic Stripping Voltammetry," in *IEEE Sensors Journal*, vol. 15, no. 5, pp. 2780-2784, May 2015.

[26] A. Määttänen, P. Ihalainen, P. Pulkkinen, S. Wang, H. Tenhu and J. Peltonen, "Inkjet-Printed Gold Electrodes on Paper: Characterization and Functionalization", *ACS Applied Materials & Interfaces*, vol. 4, no. 2, pp. 955-964, 2012. Available: 10.1021/am201609w.

[27] B. Andò and S. Baglio, "All-Inkjet Printed Strain Sensors, " in *IEEE Sensors Journal*, vol. 13, no. 12, pp. 4874-4879, Dec. 2013.

[28] A. B. Menicanin, N. P. Ivanisevic, L. D. Zivanov, M. S. Damnjanovic, A. M. Maric and D. V. Randjelovic, “Improved Performance of Multilayer CPW Inductors on Flexible Substrate,” in *IEEE Transactions on Magnetics*, vol. 50, no. 11, pp. 1-4, Nov. 2014, Art no. 8401204.

[29] B. S. Cook, J. R. Cooper and M. M. Tentzeris, "Multi-Layer RF Capacitors on Flexible Substrates Utilizing Inkjet Printed Dielectric Polymers, " in *IEEE Microwave and Wireless Components Letters*, vol. 23, no. 7, pp. 353-355, July 2013.

[30] S. Ahmed, F. A. Tahir, A. Shamim and H. M. Cheema, "A Compact Kapton-Based Inkjet-Printed Multiband Antenna for Flexible Wireless Devices, " in *IEEE Antennas and Wireless Propagation Letters*, vol. 14, pp. 1802-1805, 2015.

[31] A. Constantine, *Antenna theory*, 3rd ed. Hoboken, N.J.: Wiley-Interscience, 2005.

[32] L. Joseffsson and P. Persson, *Conformal array antenna theory and design*. New Jersey: Wiley, 2006.

[33] X. Guo, Y. Hang, Z. Xie, C. Wu, L. Gao and C. Liu, "Erratum for: Flexible and wearable 2.45 GHz CPW-fed antenna using inkjet printing of silver nanoparticles on pet substrate", *Microwave and Optical Technology Letters*, vol. 59, no. 4, pp. 992-992, 2017. Available: 10.1002/mop.30446.

[34] H. Zhang, S. Chai, K. Xiao and L. Ye, "Numerical and Experimental Analysis of Wideband E-Shape Patch Textile Antenna", *Progress In Electromagnetics Research C*, vol. 45, pp. 163-178, 2013. Available: 10.2528/pierc13091308.

[35] F. Tahir and A. Javed, "A compact dual-band frequency-reconfigurable textile antenna for wearable applications", *Microwave and Optical Technology Letters*, vol. 57, no. 10, pp. 2251-2257, 2015. Available: 10.1002/mop.29311.

[36] X. Huang et al., "Highly Flexible and Conductive Printed Graphene for Wireless Wearable Communications Applications", *Scientific Reports*, vol. 5, no. 1, 2015. Available: 10.1038/srep18298.

[37] M. Tang, B. Zhou and R. Ziolkowski, "Flexible Uniplanar Electrically Small Directive Antenna Empowered by a Modified CPW-Feed", *IEEE Antennas and Wireless Propagation Letters*, vol. 15, pp. 914-917, 2016. Available: 10.1109/lawp.2015.2480706.

[38] Q. Abbasi, M. Rehman, X. Yang, A. Alomainy, K. Qaraqe and E. Serpedin, "Ultrawideband Band-Notched Flexible Antenna for Wearable Applications", *IEEE Antennas and Wireless Propagation Letters*, vol. 12, pp. 1606-1609, 2013. Available: 10.1109/lawp.2013.2294214.

[39] D. Anagnostou, A. Gheethan, A. Amert and K. Whites, "A Direct-Write Printed Antenna on Paper-Based Organic Substrate for Flexible Displays and WLAN Applications", *Journal of Display Technology*, vol. 6, no. 11, pp. 558-564, 2010. Available: 10.1109/jdt.2010.2045474.

[40] IEEE Standard Definitions of Terms for Antennas," in *IEEE Std 145-1993* , vol., no., pp.1-32, 18 July 1993

[41] M. Scarpello et al., "Design of an Implantable Slot Dipole Conformal Flexible Antenna for Biomedical Applications", *IEEE Transactions on Antennas and Propagation*, vol. 59, no. 10, pp. 3556-3564, 2011. Available: 10.1109/tap.2011.2163761.

[42] P. Izdebski, H. Rajagopalan and Y. Rahmat-Samii, "Conformal Ingestible Capsule Antenna: A Novel Chandelier Meandered Design", *IEEE Transactions on Antennas and Propagation*, vol. 57, no. 4, pp. 900-909, 2009. Available: 10.1109/tap.2009.2014598.

[43] H. Subbaraman et al., "Inkjet-Printed Two-Dimensional Phased-Array Antenna on a Flexible Substrate", *IEEE Antennas and Wireless Propagation Letters*, vol. 12, pp. 170-173, 2013. Available: 10.1109/lawp.2013.2245292.

[44] K. Kabacik, M. E. Bjalkowski, and D. Bonefacic, "Cylindrical array antennas and their applications in wireless communications systems, " in *Proc. 16th Int. Conf. Appl. Electromagn. Commun.*, Dubrovnik, Croatia, Oct. 1–3, 2001, pp. 169–172.

[45] Keskilammi and M. Kivikoski, "Cylindrical patch antenna array for RFID applications, " in *Proc. INICA*, Berlin, Germany, Sep. 17–19, 2003, pp. 1–4.

[46] N. Athanasopoulos, K. Mourtzoukos, G. Stratakos, R. Makri, and N. Uzunoglu, "Development and testing of a 10 GHz phased-array cylindrical-antenna transmitting system incorporating a least-squares radiation-pattern synthesis technique, " *IEEE Antennas Propag. Mag.*, vol. 50, no. 6, pp. 80–88, Dec. 2008.

[47] D. Lane, "Conductive Inkjet Printed Ultra-Wideband (UWB) Planar Monopole Antenna On Low Cost Flexible Polyethelyne Terephthalate (PET) Substrate Material", Master of Science, San Diego State University, 2015. (SDSU Thesis)

[48] L. Song, A. Myers, J. Adams and Y. Zhu, "Stretchable and Reversibly Deformable Radio Frequency Antennas Based on Silver Nanowires", *ACS Applied Materials & Interfaces*, vol. 6, no. 6, pp. 4248-4253, 2014. Available: 10.1021/am405972e.

[49] X. Huang et al., "Highly Flexible and Conductive Printed Graphene for Wireless Wearable Communications Applications", *Scientific Reports*, vol. 5, no. 1, 2015. Available: 10.1038/srep18298.

[50] Yuxiao He, C. Oakley, P. Chahal, J. Albrecht and J. Papapolymerou, "Aerosol Jet printed 24 GHz end-fire quasi-Yagi-Uda antenna on a 3-D printed cavity substrate," *2017 International Workshop on Antenna Technology: Small Antennas, Innovative Structures, and Applications (iWAT)*, Athens, 2017, pp. 179-182

[51] A. Tekin and A. Emira, *High Frequency Communication and Sensing*. CRC Press, 2015, pp. 1-5.

[52] J. J. H. Wang, V. K. Tripp, J. K. Tillery, and C. B. Chambers, "Conformal multifunction antenna for automobile application," *1994 URSI Radio Science Meeting*, Seattle, Washington, p. 224, June 19-24, 1994.

[53] S. Eguchi et al., "46-2: Invited Paper: A Flexible OLED Display with Robustness and Bendability", *SID Symposium Digest of Technical Papers*, vol. 50, no. 1, pp. 632-635, 2019. Available: 10.1002/sdtp.13000.

[54] J. H. Chow, S. K. Sitaraman, C. May and J. May, "Study of Wearables with Embedded Electronics Through Experiments and Simulations," *2018 IEEE 68th Electronic Components and Technology Conference (ECTC)*, San Diego, CA, 2018, pp. 814-821.

[55] Justin Chow, K.K., Gabriel Cahn, Rui Chen, Jeffrey S Meth, Olivier Pierron, Samuel Graham, and Suresh Sitaraman. Stretch Testing of Flexible Electronics. in *2018 FLEX*. 2018. Monterey, CA, USA: SEMI.

[56] Rui Chen, Justin H. Chow, Christine Taylor, Jeffrey Meth, and Suresh K. Sitaraman. "Mechanical and Electrical Behavior of Printed Silver Conductor in Adaptive Curvature Flexure Test.", *IEEE Transactions on Components, Packaging and Manufacturing Technology*, under review, 2019.

[57] J. H. Chow, J. Meth and S. K. Sitaraman, "Twist Testing for Flexible Electronics," *2019 IEEE 69th Electronic Components and Technology Conference (ECTC)*, Las Vegas, NV, USA, 2019, pp. 785-791.s

[58] I, Bower, "Mechanical and Electrical Characterization of Printed Flexible Electronics Deformed Over Complex Surfaces", Master of Science, Georgia Institute of Technology, 2018.

[59] O. Glushko, P. Kraker and M. Cordill, "Explicit relationship between electrical and topological degradation of polymer-supported metal films subjected to mechanical

loading", *Applied Physics Letters*, vol. 110, no. 19, p. 191904, 2017. Available: 10.1063/1.4982802.

[60] M. Haghzadeh, C. Armiento and A. Akyurtlu, "Microwave dielectric characterization of flexible plastic films using printed electronics," *2016 87th ARFTG Microwave Measurement Conference (ARFTG)*, San Francisco, CA, 2016, pp. 1-4.

[61] 3M™ Technical Data", *3m.citrination.com*, 2019. [Online]. Available: https://3m.citrination.com/pif/000314?locale=en-US. [Accessed: 26- Feb- 2019].

[62] "Understanding VNA Calibration", 2012. [Online]. Available: http://anlage.umd.edu/Anritsu_understanding-vna-calibration.pdf [Accessed 18 Jan. 2019].

[63] E. Lam, "Fabrication and Material Characterization of Silver Cantilevers via Direct Surface Micromachining", Undergraduate, Massachusetts Institute of Technology, 2005.

[64] "Polyethylene terephthalate - online catalogue source - supplier of research materials in small quantities – Goodfellow", *Goodfellow.com*, 2019. [Online]. Available: http://www.goodfellow.com/E/Polyethylene-terephthalate.html. [Accessed: 27- Feb- 2019].

[65] D. Yu and F. Spaepen, "The yield strength of thin copper films on Kapton", *Journal of Applied Physics*, vol. 95, no. 6, pp. 2991-2997, 2004.

[66] J. Zhu, J. Feng and Z. Guo, "Mechanical properties of commercial copper current-collector foils", *RSC Adv.*, vol. 4, no. 101, pp. 57671-57678, 2014.

[67] "Dielectric Constant, Strength, & Loss Tangent - RF Cafe", *Rfcafe.com*, 2019. [Online]. Available: http://www.rfcafe.com/references/electrical/dielectric-constants-strengths.htm. [Accessed: 07- Nov- 2019].

[68] U. Tata, H. Huang, R. Carter and J. Chiao, "Exploiting a patch antenna for strain measurements", *Measurement Science and Technology*, vol. 20, no. 1, p. 015201, 2008. Available: 10.1088/0957-0233/20/1/015201.